

2009

The functionalization of carbon nanosheets

Ronald A. Quinlan

College of William & Mary - Arts & Sciences

Follow this and additional works at: <https://scholarworks.wm.edu/etd>



Part of the [Condensed Matter Physics Commons](#), and the [Materials Science and Engineering Commons](#)

Recommended Citation

Quinlan, Ronald A., "The functionalization of carbon nanosheets" (2009). *Dissertations, Theses, and Masters Projects*. Paper 1539623539.

<https://dx.doi.org/doi:10.21220/s2-9djv-fn57>

This Dissertation is brought to you for free and open access by the Theses, Dissertations, & Master Projects at W&M ScholarWorks. It has been accepted for inclusion in Dissertations, Theses, and Masters Projects by an authorized administrator of W&M ScholarWorks. For more information, please contact scholarworks@wm.edu.

The Functionalization of Carbon Nanosheets

Ronald A. Quinlan

Figsboro, Virginia

Master of Science, The College of William and Mary, 2005
Bachelor of Science, The College of William and Mary, 2003

A Dissertation presented to the Graduate Faculty
of the College of William and Mary in Candidacy for the Degree of
Doctor of Philosophy

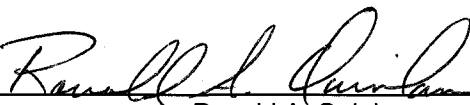
Department of Applied Science

The College of William and Mary
January 2009

APPROVAL PAGE

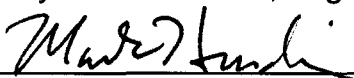
This dissertation is submitted in partial fulfillment of
the requirements for the degree of

Doctor of Philosophy

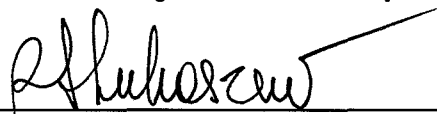


Ronald A. Quinlan


Approved by the Committee, August, 2008



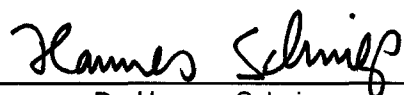
Committee Chair
Dr. Mark K. Hinders
The College of William & Mary




Dr. R. Alejandra Lukaszew
The College of William & Mary



Dr. Ronald A. Outlaw
The College of William & Mary



Dr. Hannes Schniepp
The College of William & Mary



Dr. Brian C. Holloway
Luna Innovations, Incorporated

ABSTRACT PAGE

Carbon nanosheets are a novel two-dimensional nanostructure made up of 2-20 graphene atomic planes oriented with their in-plane axis perpendicular to the growth substrate. Previous efforts in developing nanosheet technology have focused on the characterization of the system and their development as an electron source due to the high atomic enhancement factor (beta) and low turn on field. Further investigation of nanosheets as high surface area electrodes revealed poor wetting by polymeric material and extreme hydrophobic behavior.

Because nanosheet technology has promise as a high surface area electrode material, this thesis research has focused on three areas of interest: the enhancement of nanosheets through chemical modification, the incorporation of the nanosheets into a polymeric composite and the delivery of a proof of concept measurement. We have successfully introduced defects into the graphene lattice of the nanosheet system via an acid treatment. Inspection of these defects by x-ray absorption near-edge spectroscopy (XANES) shows the introduction of two features in the spectra assigned to C=O pi* and C-O sigma* transitions. Thermal desorption spectroscopy (TDS) was used to identify the oxygen containing groups created during the functionalization as carboxylic and hydroxyl functional groups. These groups were identified through the combination of carboxylic, hydroxyl, anhydride and lactone peaks in the CO₂, CO and H₂O TDS spectra. Deconvolution of the TDS spectra using 1st and 2nd order Polanyi-Wigner equations enables the calculation of desorption energy values for individual features and for the estimation of the number of atoms desorbing from the surface during a particular event. Identification of the exact nature of the functional groups was attempted through high resolution x-ray photoelectron spectroscopy (XPS) of the C(1s) and O(1s) peaks. Though the pairing of sub-peaks with specific functionalities of the system was not possible due to the complexities of the spectra, the trends observed in the data support the data gathered via the XANES and TDS experiments.

Also, a procedure for the classification of defect density and exact functionality was outlined. Deconvolution of the TDS spectra using 1st and 2nd order Polanyi-Wigner equations enabled the calculation of desorption energy values for individual features and for the estimation of the number of atoms desorbing from the surface during a particular event. This information along with the changing sub-peak areas from dedicated and calibrated XPS system would allow for not only a more accurate estimation of defect density, but also for the identification of sub-peaks in the C(1s) and O(1s) spectra.

Finally, photoluminescence measurements of poly[2-methoxy-5-(2'-ethyl-hexyloxy)-1,4-phenylene vinylene] (MEH-PPV) and MEH-PPV/nanosheet systems showed a quenching of three orders of magnitude for the MEH-PPV/nanosheet system suggesting that nanosheets are a viable option for excitation separation in organic photovoltaics.

Contents

Dedication	iv
Acknowledgments	v
List of Tables	vii
List of Figures	viii
1 Introduction	1
1.1 Carbon nanostructures	1
1.2 Organization	7
2 Materials analysis tools used for the inspection of carbon nanosheets	9
2.1 Introduction to materials analysis	9
2.2 Growth of carbon nanosheets via radio frequency (RF) plasma enhanced chemical vapor deposition (PE CVD)	10
2.2.1 Experimental setup for the growth of carbon nanosheets	12
2.3 Functionalization of carbon nanosheets via acid treatment	15
2.3.1 Experimental setup for the functionalization of carbon nanosheets	18
2.4 Scanning electron microscopy (SEM) and energy dispersive x-ray spectroscopy (EDS)	21
2.5 Introduction to Raman spectroscopy	27
2.5.1 Experimental use of Raman spectroscopy	31
2.6 Fourier transform infrared spectroscopy (FT-IR)	33
2.6.1 Experimental setup of the FT-IR for the inspection of functionalized nanosheets	35
2.7 Four-point probe	38
2.8 X-ray absorption near-edge spectroscopy (XANES)	41
2.8.1 Experimental setup for the investigation of functionalized nanosheets using XANES	47
2.9 Thermal desorption spectroscopy (TDS)	49
2.9.1 Experimental use of TDS for the inspection of functionalized carbon nanosheets	52
2.10 X-ray photoelectron spectroscopy (XPS)	61

2.10.1	Experimental setup for XPS inspection of functionalized carbon nanosheets	65
2.11	Summary	66
3	Experimental results and discussion of XANES, TDS and XPS experiments	67
3.1	Introduction	67
3.2	X-ray absorption near-edge spectroscopy	68
3.2.1	Results and interpretation of data from x-ray absorption near-edge spectroscopy (XANES)	68
3.2.2	Summary of XANES experiments	82
3.3	Thermal desorption spectroscopy	83
3.3.1	Identification of the TDS features	83
3.3.2	Deconvolution of the TDS spectra	92
3.3.3	Summary of TDS experiments	99
3.4	High resolution X-ray photoelectron spectroscopy	100
3.4.1	Interpretation of XPS data	100
3.4.2	Summary of XPS results	120
3.5	Summary and discussion of functional group characterization	122
4	Atomic layer deposition of titanium dioxide nanostructures	126
4.1	Introduction to atomic layer deposition (ALD) of titanium dioxide	126
4.2	Motivation for deposition of TiO ₂ on carbon nanosheets	127
4.3	Experimental setup	130
4.4	Results and discussion	131
4.5	Summary of carbon nanosheets as nanostructured template	139
5	Conformal coating and transfer of carbon nanosheet films to a zero thermal budget substrate	140
5.1	Introduction	140
5.2	Motivation for the conformal coating of carbon nanosheets	141
5.3	Experimental	144
5.4	Results and discussion	145
5.5	Photoluminescence measurements as a proof of concept for carbon nanosheet as high surface area electrodes	156
5.6	Summary	161
6	Summary and future work	162
6.1	Summary	162
6.2	Avenues for future work	166
6.3	Defect concentration and quality in carbon nanosheets	166
6.4	Further functionalization of carbon nanosheets	168

6.5	Carbon nanosheets as high surface area electrodes	169
6.6	Epitaxial growth of graphene	170
6.7	Carbon nanosheets as chemical sensors	171
	Afterword	174
	Bibliography	175
	Vita	180

To Lara -

Without your love and support this would not have been possible

Acknowledgments

I would like to thank Dr. Brian C. Holloway for his advice, support and help throughout my graduate career at the College of William & Mary. Though I may not have liked it at the time, I think in five years I will appreciate it.

I would also like to thank Prof. Mark K. Hinders for stepping in over the past two years as my advisor. His guidance and support were invaluable throughout this process.

I will always be indebted to Dr. Ronald A. Outlaw for his support, enthusiasm and advice. Whether the questions were about vacuum science or college football, he was there.

I am extremely grateful for the support of my friends – Blair Williams, Hilary DeRemigio, Jefferey Groff, Drew LaMar, Michael Bagge-Hansen and Jill Bingham. Whether MATLAB, a place to sleep or VA beer night, I could always count on them.

A special thank you goes to the Chemistry Department for helpful discussions, department keys for weekend experiments and extra glassware. Specifically, Prof. Robert D. Pike for getting me started on this path.

I need to thank everyone in my lab, past and present. Dr. Zhao Xin, Dr. Kun Hou, Dr. Zhu Mingyao, and Dr. Wang Jiajun. Thank you not only for helping me with experiments, but also for teaching and sharing your wisdom with me.

I would like to thank all the great people at Luna nanoWorks. Getting to work as a member of an industrial team was an invaluable experience. Especially, Charlie Gauss, Veronica Welsh, Dr. Martin Drees, Russel Ross, Claudia Cordona and Dr. Brian Holloway.

I would like to thank my friends and colleagues from Uppsala University – Erika Widenkvist, Dr. Mårten Rooth, Dr. Victoria Coleman, Dr. Helena Grennberg and Dr. Ulf Jansson – for their collaboration and hospitality over the past two years.

Special thanks to my mother for always being my biggest fan, my sister for her constant support and my father for introducing me to the lab and for being my best friend.

Thanks to Mary, Steve and Anna for their help and support in more ways than I can list.

Finally, I would like to thank my wife Lara. She continued to believe in me even when I did not.

List of Tables

3.1	Results for the calculation of $\Delta E_{d,i}$, N_i , and ν_i for the acid-treated carbon nanosheet CO ₂ spectrum fit with a second order Polanyi-Wigner equation.	96
3.2	Results for the calculation of $\Delta E_{d,i}$, N_i , and ν_i for the acid-treated carbon nanosheet CO spectrum fit with a second order Polanyi-Wigner equation.	97
3.3	Results for the calculation of $\Delta E_{d,i}$, N_i , and ν_i for the acid-treated carbon nanosheet H ₂ O spectrum fit using a second order Polanyi-Wigner equation.	98
3.4	Results of TDS peak identification	123
5.1	As-deposited sheets and transferred sheets have a resistivity close to that of graphite. Values reported are best values based on experiments with varying force of probes. Average is based on varying the outer probe current from 0.1mA to 1.5mA.	155

List of Figures

1.1	Schematic representing the different allotropes of carbon	3
1.2	Schematic representation of nanotube unit cell and definition of chiral angle	4
1.3	Schematic illustration of nanotube chirality	5
1.4	Schematic of a typical carbon nanosheet	6
2.1	Schematic of a fullerene and nanotube illustrating the dimensions . .	11
2.2	Schematic of nanosheet growth chamber	14
2.3	SEM of typical carbon nanosheets with schematic representation . .	14
2.4	SEM of attempt to deposit Pt catalyst on nanosheets	17
2.5	Schematic of functionalization setup	19
2.6	SEM of pre and post acid-treatment nanosheets	20
2.7	Raman spectrum of functionalized nanosheets	20
2.8	Different signals from electron beam interactions	24
2.9	Schematic of a typical SEM	25
2.10	Digital image of SEM	26
2.11	Inelastic scattering of light during Raman spectroscopy	29
2.12	Schematic of a typical Raman system	30
2.13	Raman of a typical nanosheet sample	32
2.14	Raman spectrum of typical CNT sample	32
2.15	Schematic of a typical FT-IR	36
2.16	Typical FT-IR results for functionalized nanosheets	37
2.17	Schematic of a four-point probe	39
2.18	Digital image of the four-point probe	40
2.19	Schematic of x-ray absorption energy ranges defining the difference between XANES and EXAFS	42
2.20	Schematic of x-ray absorption	42
2.21	Molecular orbital diagram of a theoretical C-C system	44
2.22	Schematic of absorption in the XANES spectrum	44
2.23	XANES spectrum of HOPG	45
2.24	Digital image and schematic of beamline D1011 at MAX-Lab	46
2.25	Digital image of the copper sample holder	48
2.26	Schematic of the TDS experimental setup	50
2.27	Schematic of the Feulner and Menzel cup	50
2.28	Digital image of the sample holder and sample used during the TDS experiments	51

2.29	Schematic of dehydration event between two acids	56
2.30	Schematic of dehydration event between an acid and a hydroxyl	56
2.31	Schematic of CO and CO ₂ desorption from an anhydride group	57
2.32	Schematic of CO desorption from a lactone type functional group	58
2.33	Schematic of the processes during an XPS experiment	62
2.34	Schematic of a typical XPS system	64
3.1	XANES spectra of HOPG and as-deposited nanosheets	69
3.2	XANES spectra of HOPG and as-deposited nanosheets with acid and water treated offset	70
3.3	XANES spectra of HOPG and as-deposited nanosheets	70
3.4	Close up of XANES spectra for B1 and B2 features	72
3.5	Angular dependence of acid-treated samples in XANES spectra	74
3.6	Angular dependence of water-treated samples in XANES spectra	75
3.7	XANES spectra of 3hr acid-treated sample heated stepwise	78
3.8	XANES spectra of 23hr acid-treated sample heated stepwise	79
3.9	Comparison of heated acid-treated sample to HOPG	80
3.10	Density functional theory calculations of the local density of states for di-vacancy nanosheets	81
3.11	Measurement of nanosheet conductivity after acid-treatment	81
3.12	Raman spectrum of pre- and post-functionalized nanosheets	84
3.13	TDS spectrum for Ta substrate	85
3.14	TDS spectra for CO	87
3.15	TDS spectra for CO ₂	89
3.16	TDS spectra for H ₂ O	90
3.17	Schematic of dehydration event	91
3.18	Schematic of functional groups discussed in TDS results	91
3.19	First order deconvolution of acid-treated CO ₂ spectrum	94
3.20	Second order deconvolution of acid-treated CO ₂ spectrum	95
3.21	Second order deconvolution of acid-treated CO spectrum	97
3.22	Second order deconvolution of acid-treated H ₂ O spectrum	98
3.23	Schematic representation of functional groups discussed during XPS analysis	102
3.24	XPS room temperature survey scans	102
3.25	High resolution C(1s) spectrum for as-deposited nanosheets at room temperature	103
3.26	High resolution C(1s) spectrum for acid-treated nanosheets at room temperature	104
3.27	High resolution C(1s) spectrum for water-treated nanosheets at room temperature	105
3.28	Acid-treated C(1s) spectrum after heating to 150°C	106
3.29	Water-treated C(1s) spectrum after heating to 150°C	107
3.30	As-deposited C(1s) spectrum after heating to 150°C	108
3.31	Acid-treated C(1s) spectrum after heating to ≈ 450°C	109
3.32	As-deposited room temperature O(1s) spectrum	112

3.33	Acid-treated room temperature O(1s) spectrum	113
3.34	Water-treated room temperature O(1s) spectrum	114
3.35	As-deposited O(1s) spectrum after heating to $\approx 150^{\circ}\text{C}$	115
3.36	Acid-treated O(1s) spectrum after heating to $\approx 150^{\circ}\text{C}$	116
3.37	Water-treated O(1s) spectrum after heating to $\approx 150^{\circ}\text{C}$	117
3.38	As-deposited O(1s) spectrum after heating to $\approx 350^{\circ}\text{C}$	118
3.39	Acid-treated O(1s) spectrum after heating to $\approx 450^{\circ}\text{C}$	118
3.40	Water-treated O(1s) spectrum after heating to $\approx 200^{\circ}\text{C}$	119
3.41	Water-treated O(1s) spectrum after heating to $\approx 450^{\circ}\text{C}$	119
4.1	SEM and schematic of as-deposited nanosheets	129
4.2	SEM and TEM of TiO_2 deposited on as-deposited nanosheets at 100 cycles	133
4.3	TEM of TiO_2 deposited at 50 and 75 cycles	133
4.4	TEM of TiO_2 on acid-treated nanosheets at 50 cycles	134
4.5	XRD diffractogram of TiO_2 coated nanosheets	134
4.6	Raman spectra of TiO_2 coated nanosheets	136
4.7	TEM of broken nanosheet with amorphous TiO_2	138
5.1	SEM images of nanosheet spin casting that resulted in poor incorporation	143
5.2	Schematic of spin casting setup and process	146
5.3	Successful spin casting of carbon nanosheets	149
5.4	Buckling of polystyrene film	149
5.5	Digital image of damaged nanosheet/polystyrene film	150
5.6	Digital image of the nanosheet film washing procedure	150
5.7	Schematic of transfer process utilizing backing substrate to stiff substrate	152
5.8	Schematic of transfer process without a backing substrate to a polymeric substrate	152
5.9	Digital images of doctor blading and solution casting a polymeric substrate	153
5.10	Raman spectra of nanosheet film during and after the washing process	154
5.11	SEM of transferred nanosheets and digital image of large transfer area	155
5.12	Schematic representation of the photoluminescence process in an organic polymer	158
5.13	Schematic representation of the structure of MEH-PPV	158
5.14	Schematic representations of donor-acceptor devices	159
5.15	Photoluminescence measurement of MEH-PPV/nanosheet film	160

Chapter 1

Introduction

1.1 Carbon nanostructures

The fabrication and use of nanostructures has received a lot of attention recently because the limits of traditional microstructures are being pushed by current technology. A nanostructure is defined as a structure that has at least one of the three dimensions between 1 and 100nm as illustrated by Figure 1.1. If all three of the dimensions fall in this range, the structure is considered a zero-dimensional (0D) structure. Conversely, if all three dimensions are outside of this range, the structure is considered bulk, or three-dimensional (3D). A one-dimensional (1D) nanostructure will have two dimensions that are nanometer in scale and a two-dimensional (2D) structure will only have one dimension that is in the range. A carbon nanostructure is simply a structure that fits the preceding criteria and is composed of carbon. Carbon is unique in that there is at least one allotrope in all four categories as shown in Figure 1.1. Well known carbon nanostructures include the 0D fullerenes and 1D carbon nanotubes and nanofibers. The 3D forms of carbon—diamond and graphite—are also commonly known. The discoveries of 2D carbon nanostructures, including nanosheets, nanowalls and graphene are more recent and complete the nanostructure group.

Fullerenes are a class of material made up of hollow spheres or ellipsoids. The Buckminsterfullerene (C_{60})—named for the futurist Richard Buckminster Fuller best known for his geodesic dome design—is a 0D carbon nanostructure discovered by Kroto

et al. in 1985 [1] that is made up of pentagons and hexagons of carbon. C_{60} (Fig. 1.1 (a)) is the smallest structure to obey the isolated pentagon rule, meaning that no two pentagons are adjacent and each pentagon is surrounded by five hexagons. If carbon atoms are added to the central axis, an ellipsoid is formed. As the number of atoms added to the axis (j) increases, the size of the ellipsoid (C_{60+j}) increases as well until a nanotube (Fig. 1.1 (b)) is formed.

Carbon nanotubes can be single-walled as seen in Figure 1.1 (b) or they can be multi-walled with concentric tubes layered inside one another. Though they have been used for centuries [2] Iijima is given credit for their discovery in 1991 after successfully characterizing such structures via transmission electron microscopy [3]. The formation of a single-walled nanotube can be imagined by taking a graphene plane and wrapping it around an axis that is parallel to this plane so that the edges are seamlessly mated (Fig. 1.2 - point O overlaps point A and point B overlaps point B'). The chiral angle (θ) is measured relative to the direction defined by a_1 . The chiral vector (OA) is then defined by the relationship of the lattice vectors (a_1 and a_2) and the integers n and m represented in Equation 1.1:

$$OA = na_1 + ma_2 \quad (1.1)$$

When n or m is equal to zero, the chiral angle of the nanotube is 0° and the nanotube is called a zigzag tube. When $n = m$, however, the nanotubes are called armchair and have a chiral angle of 30° . For all other combinations of n and m , the tubes are considered chiral. This is illustrated in Figure 1.3. Due to their diameter and geometric structures, nanotubes can also be metallic or semiconducting as predicted early on by theory [4]. If $(2n + m) = 3q$, where q is an integer, then the nanotube is considered metallic, otherwise the tube is semiconducting. All armchair nanotubes are metallic.

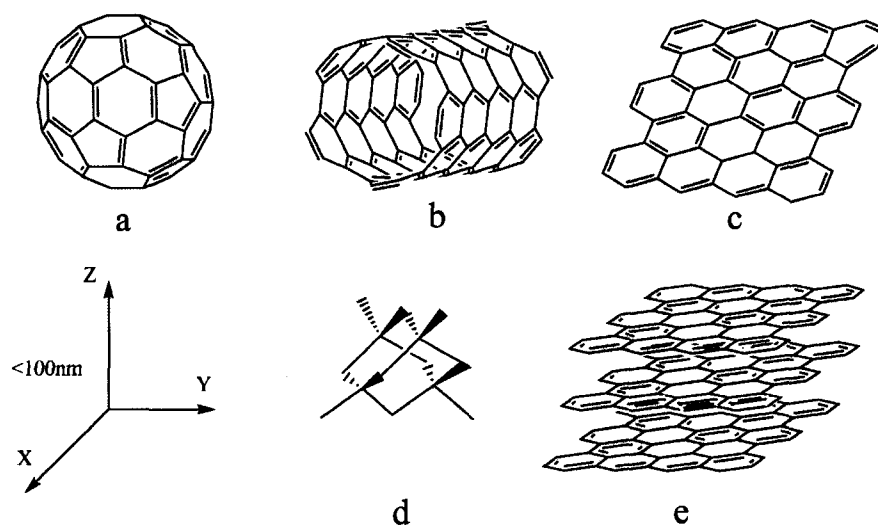


Figure 1.1: The different allotropes of carbon representing the different dimensional structures. The 0D allotrope is represented by a C₆₀ fullerene (a), the 1D by a single-walled nanotube (b), 2D by single graphene plane (c) and the 3D structures of diamond (d) and graphite (e) are shown. The dimensions are represented on the lower left of the image. For a 0D structure, all dimensions (x, y and z) must be below 100nm.

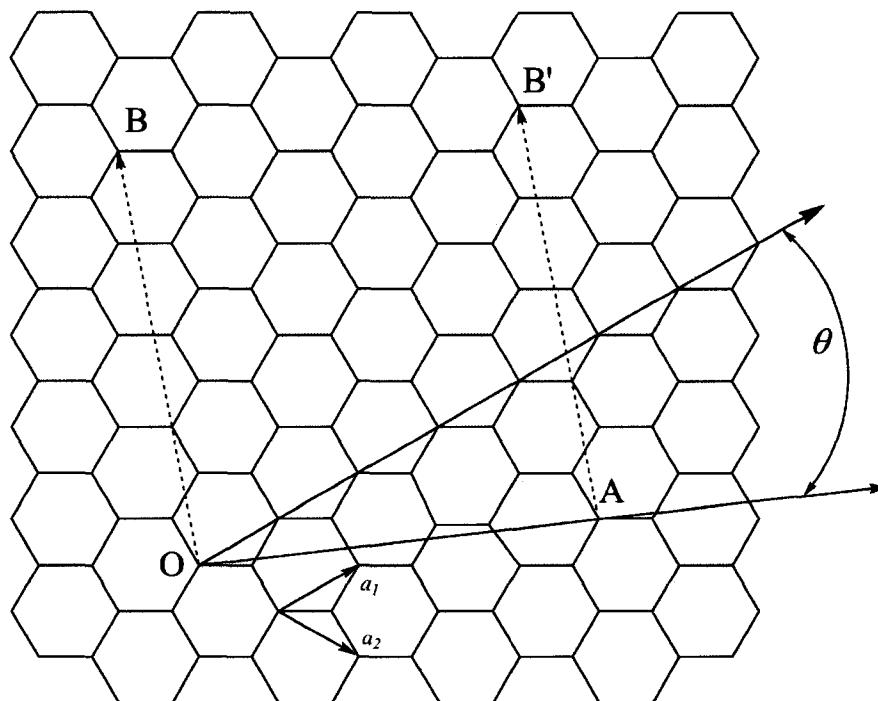


Figure 1.2: To form the nanotube, the graphene sheet is rolled up so that O meets A and B meets B' . The chiral angle (θ) is defined by the angle between the zigzag direction and the chiral vector (OA). The unit vectors are represented by a_1 and a_2 .

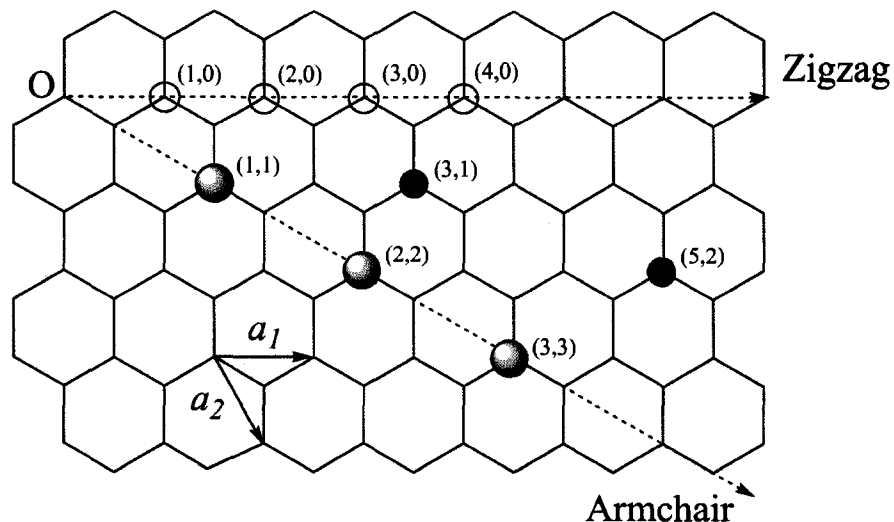


Figure 1.3: To form the nanotube, the graphene sheet is rolled up so that O meets A and B meets B' . The chiral angle (θ) is defined by the angle between the zigzag direction and the chiral vector (OA). The unit vectors are represented by a_1 and a_2 .

The two-dimensional nanostructures were not observed until 1997 when Ando *et al.* reported the observation as a bi-product of nanotube synthesis [5]. Our group was one of the first to report the intentional growth of a two-dimensional structure which we termed carbon nanosheets [6, 7]. Conceptually, these nanosheets are graphene layers that grow vertically oriented from the substrate as illustrated in Figure 1.4. Ultrathin epitaxial graphene films have been grown by vacuum graphitization of single-crystal silicon carbide, but typically produces several layers [8, 9]. Single graphene layers (Fig. 1.1 (c)), although hypothesized for years, were once thought to be thermodynamically unstable. However, Novoselov *et al* were able to isolate them in 2005 [10] via mechanical exfoliation.

Chemical vapor deposition (CVD) is a process commonly used for the deposition of thin film materials. During a typical process, gas phase reactants decompose and react on a substrate surface to create the desired film. There are various types of CVD available that are distinguished by the processing parameters and by means in which the chemical reactions are activated (e.g., low-pressure CVD vs. ultrahigh vac-

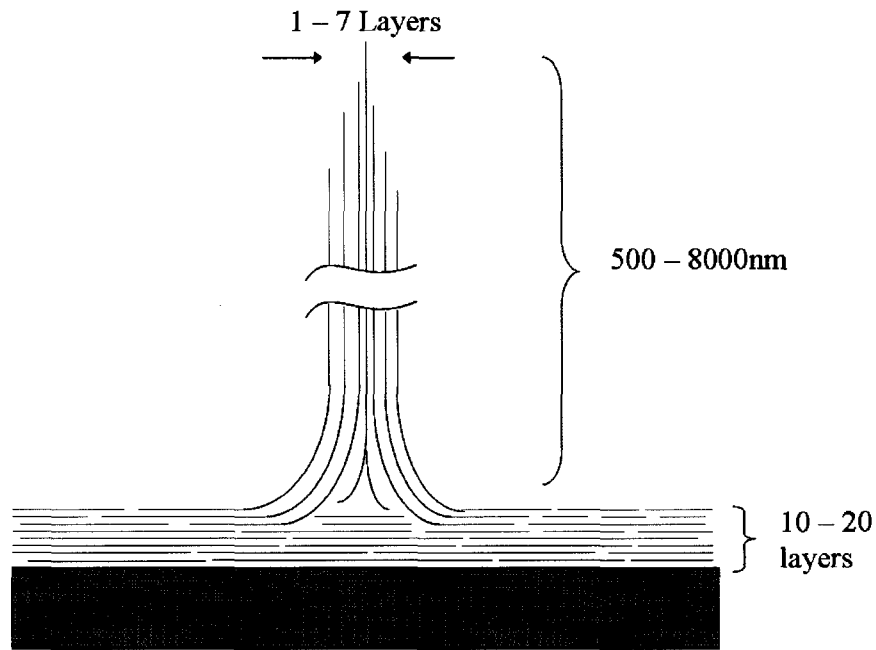


Figure 1.4: Schematic of carbon nanosheets illustrating the vertical nature of the graphene layers.

uum CVD and microwave plasma assisted CVD vs. radio frequency plasma enhanced CVD). Though carbon nanosheets have been obtained by other methods [5,11–13], we use a radio frequency plasma enhanced chemical vapor deposition (RF PECVD) process [6]. This process utilizes an inductively coupled plasma to enhance the reaction rates of the precursor materials which allows for lower temperature processing. Our carbon nanosheets are the thinnest reported for structures not classified as graphene with two-layer edges commonly observed in transmission electron microscopy (TEM). Our nanosheets also do not require a catalyst for growth, thus eliminating the need for removal of non-carbon species after the growth.

The chirality (armchair, zigzag or chiral) and the curvature of nanotubes define the electronic properties of the material. These properties, along with remarkable thermal and mechanical properties make nanotubes interesting for a variety of applications. To date, the properties of graphene are a result of the edges of the sheets where

interesting electronic properties emerge [14]. Due to the structure of the material these sites are inherently limited, however. The same can be said of carbon nanosheets. Recently, because of their high atomic enhancement factor (β) and low turn on field, most research has focused on their development as an electron source. Therefore, this work focuses on the functionalization of carbon nanosheets and the characterization of resulting structures for the purpose of developing nanosheet technology as high surface area electrodes. By controllably creating defects and functional groups in the lattice of the material new opportunities open up. This thesis also includes a process for transferring the carbon nanosheets to zero thermal-budget substrate—a substrate that has experienced no thermal treatment—without damaging the original morphology. Additionally, as a proof-of-concept, measurements illustrating the effectiveness of carbon nanosheets as an exciton separation interface were also performed. Finally, carbon nanosheets were also used as templates for the growth of nanostructured TiO_2 during an atomic layer deposition (ALD) process.

1.2 Organization

For the purposes of this research, carbon nanosheets were synthesized via RF PECVD. The as-deposited nanosheets were functionalized for the development of nanosheet technology and their use in advanced graphene devices. Chapter 2 focuses on the fundamentals of the techniques that were employed throughout the course of this work. The experimental setups used for our purposes are also outlined when appropriate.

Chapter 3 focuses on the experimental results of three major characterization techniques, include x-ray absorption near-edge spectroscopy (XANES), thermal desorption spectroscopy (TDS) and high resolution x-ray photoelectron spectroscopy (XPS). With the use of these techniques, we were able to identify that defects were

successfully created in the graphene lattice of the carbon nanosheets and we were also able to define the nature of the functional groups created.

Chapter 4 is representative of the functionality of functionalized carbon nanosheets. The work is also representative of the collaboration developed with Uppsala University in Sweden during the lifetime of this research.

Chapter 5 introduces a novel process for the transfer of carbon nanosheets to zero thermal-budget substrate while retaining the original morphology of the material. Experimental support for the use of carbon nanosheets as high surface area electrodes in organic photovoltaics is also presented.

Finally, Chapter 6 provides a summary of all the work and possible directions for future work. The functionalization of carbon nanosheets—including the identification of the functional groups—provides ample opportunity for the progression of nanosheet technology.

Chapter 2

Materials analysis tools used for the inspection of carbon nanosheets

2.1 Introduction to materials analysis

Throughout the course of this research, several techniques were used to investigate the morphology, composition, quality and properties of the carbon nanosheets. Two of these techniques, Raman spectroscopy and scanning electron microscopy (SEM) were utilized throughout the course of study for all of the various experiments. Others, however, were utilized as a more direct part of the experiments, such as Fourier-transform infrared (FT-IR), four point probe, x-ray absorption near-edge spectroscopy (XANES), x-ray photoelectron spectroscopy (XPS), and thermal desorption spectroscopy (TDS). In this chapter, we provide an introduction to the growth of carbon nanosheets and the basic characterization of these novel structures. A brief background concerning the underlying fundamental principles for each technique utilized in subsequent experiments is also presented.

2.2 Growth of carbon nanosheets via radio frequency (RF) plasma enhanced chemical vapor deposition (PE CVD)

Carbon nanostructures are labeled as zero dimensional (0D) and as one dimensional (1D) nanostructures, respectively, because of the number of dimensions that are less than 100nm. Figure 2.1 provides a schematic representation of a fullerene (a) and a nanotube (b), illustrating their size ranges and corresponding to their labeled dimensions. Graphite and diamond are well-known, 3D carbon structures, but a 2D structure was not. Sheet-like carbon structures were noticed as co-deposits in carbon nanotube (CNT) synthesis [15,16], but it was not until Ando *et al.* [5] reported the petal-like sheets as a by-product of CNT synthesis that the synthesis of these structures were investigated.

The synthesis of 2D carbon nanostructures has been reported by several methods. Shang *et al.* [13] reported the synthesis of carbon nanoflake films via hot filament CVD and Wu *et al.* [17] and Chuang [12] reported using microwave assisted PECVD for the synthesis of carbon nanowalls. Novoselov *et al.* [18] manufactured atomically thin graphene via mechanical exfoliation of graphite. Our group has previously reported the synthesis of a novel, 2D carbon nanostructure via an inductively coupled, radio frequency plasma enhanced chemical vapor deposition (RF PECVD) process [6,7,19–21] and has also reported a proposed mechanism for their growth [20,22]. Unlike the other 2D carbon nanostructures mentioned above however, our carbon nanosheets are atomically thin, vertically free-standing from the substrate, and do not require a non-carbon catalyst for growth. Throughout the course of this research, the nanosheets used were synthesized in the manner briefly introduced below for the purpose of familiarizing the reader with the growth parameters available. The ex-situ characterization of typical carbon nanosheets via Raman spectroscopy and scanning electron microscopy (SEM) will also be provided as a reference for later experiments.

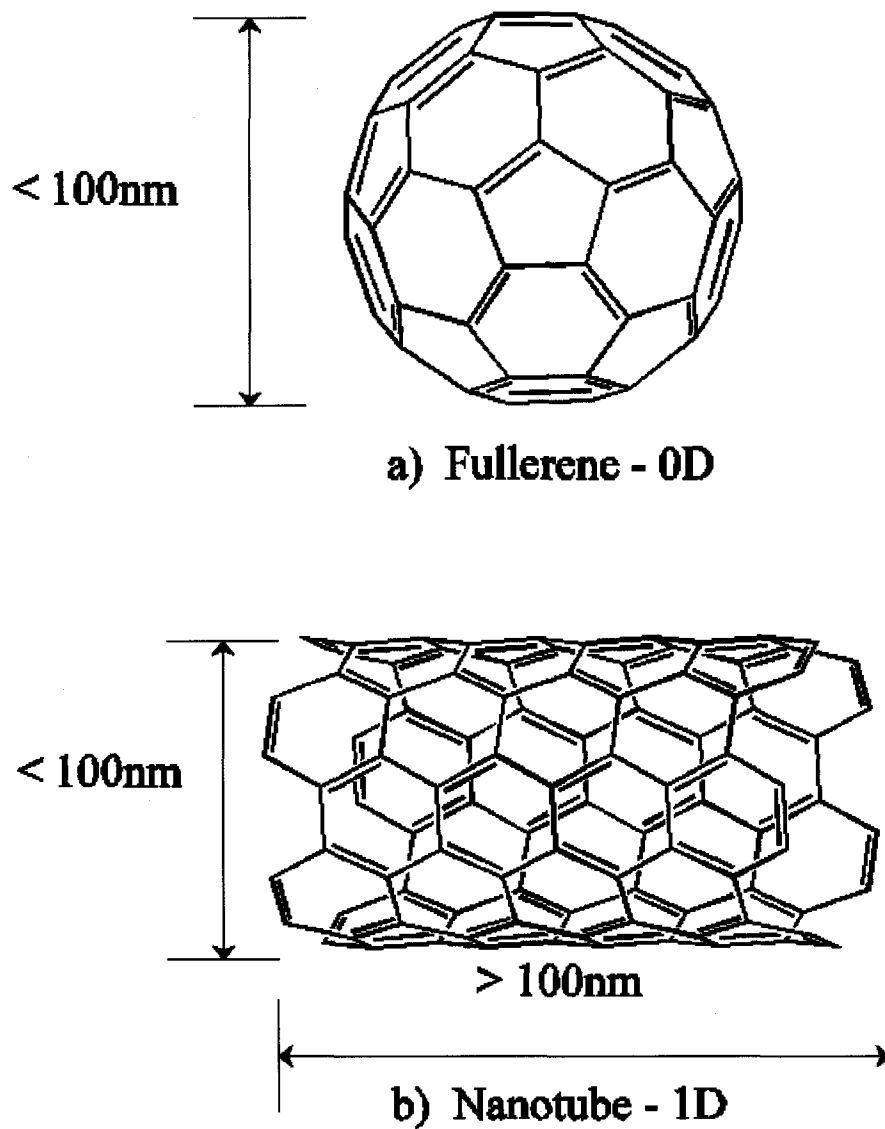


Figure 2.1: A schematic representation of a fullerene (a) and a nanotube (b) representing the sizes of the material and the labeling of the respective structures as 0D and 1D.

2.2.1 Experimental setup for the growth of carbon nanosheets

As previously reported [6, 7, 19–21], nanosheets were grown via RF PECVD. We are capable of depositing nanosheets on various substrates, ranging from metals to insulators [7]. For the functionalization experiments, metal substrates were needed to enhance the nanosheet/substrate interaction so that the system would withstand the treatment. Tungsten was used for the high resolution XPS and XANES experiments while tantalum was used for the TDS experiments. Quartz was utilized for the photoluminescence experiments and for all other experiments silicon wafers were utilized. Using water cooled copper tubing as a coiled antenna, RF power was inductively coupled into the deposition chamber. Substrates were used as received with no special treatment or catalyst prior to growth. Using a resistive heater, substrates were heated in a hydrogen atmosphere ($\approx 60\text{mTorr}$) to a temperature around 700°C . Upon reaching the desired temperature, methane gas, used as the carbon feedstock, was introduced into the system. The gas flow rate of hydrogen was kept constant at 6 sccm during the heating and during the deposition. The flow rate of methane was 4 sccm. Standard growth conditions consisted of an RF power of 900W, a pressure of $\approx 100\text{mTorr}$ and substrate temperatures from 650°C - 800°C for times ranging from ten to twenty minutes. The methane flow was cut to zero with the plasma still ignited, for a brief time, to allow hydrogen to remove any amorphous carbon. After growth, the substrates were allowed to cool in a hydrogen atmosphere before removing to atmosphere. The samples were subject to no post-deposition treatments before being analyzed via SEM and Raman. A schematic of the deposition chamber is provided in Figure 2.2.

An SEM of typical carbon nanosheets can be seen in Figure 2.3, both plan view (a) and a cross-section (b) view. A schematic of typical carbon nanosheets is provided in Figure 2.3 (c). These micrographs reveal the smooth sides and atomically sharp edges of the nanosheets. The overall translucent to transparent character of the sheets

shown in the image suggests the thin nature of the material.

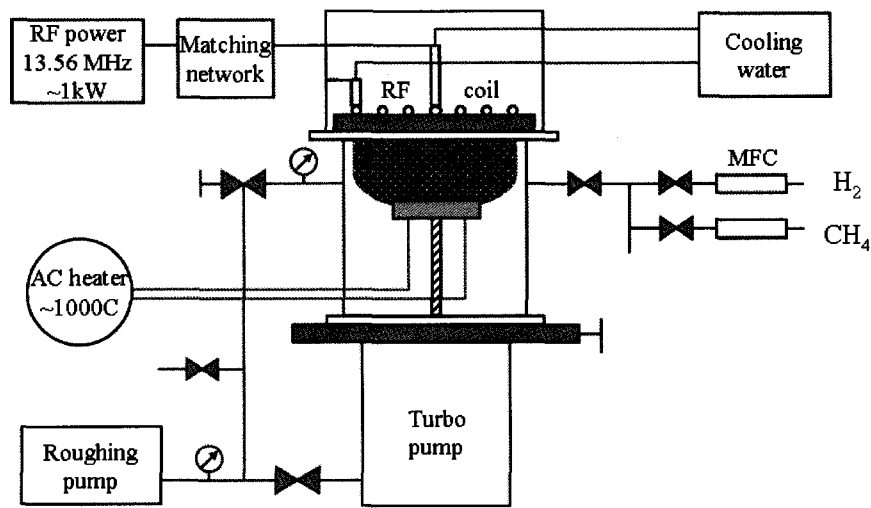


Figure 2.2: Schematic of the growth chamber used for the deposition of carbon nanosheets [7]

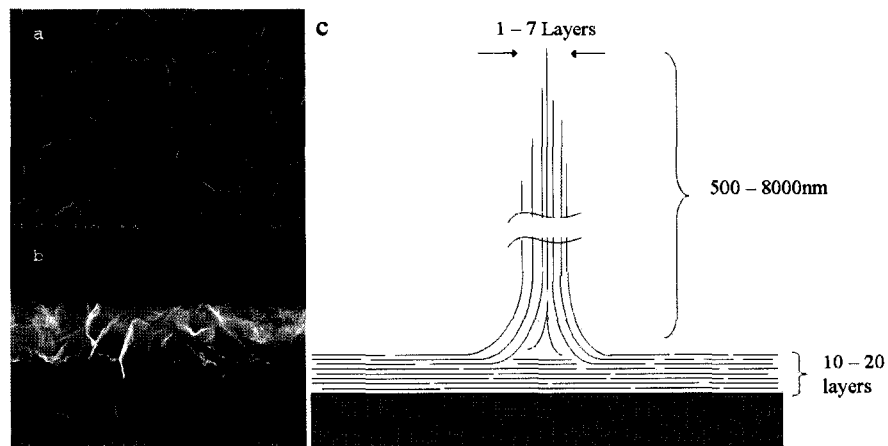


Figure 2.3: SEM image of a typical nanosheet sample. The top panel (a) is a canopy view and the bottom panel (b) provides a cross-sectional view. The SEM is operating at 15keV and in SE mode. The schematic (c) represents a single, typical nanosheet in the system.

2.3 Functionalization of carbon nanosheets via acid treatment

The functionalization of carbon nanostructures to increase the utility of the structures in applications is an area of current interest. Products such as Methanofullerene Phenyl-C61-Butyric-Acid-Methyl-Ester (PCBM), a functionalized fullerene, has been shown to increase the efficiency of organic photovoltaics (OPV) and is now one of the most commonly used n-type semiconductors used in OPVs [23]. The use of oxygen containing compounds on the surface of carbon nanotubes (CNTs) to act as chemical [24–26] and biological [27] sensors has also been reported. Graphene is a new and emerging material that is being investigated for use in device applications. As of now, arguably the most usable feature of graphene has been the edges of the sheets and ribbons, where the differences between armchair and zigzag edges present unique opportunities and sites available for functionalization. The number of these sites is obviously limited however, due to the edge to volume ratio, limiting the use of the structures. By creating defects over the entire nanosheet surface area new possibilities are created and are available [14].

Acid treatment is known to result in oxygen created defects in carbon nanotubes and graphite [28] and this is expected to also work for nanosheets. The creation of defect sites and the addition of functional groups around the defect site would not only allow for further functionalization of the graphene sheets, but may also allow for the tailoring of the electronic properties of the nanosheets.

Initial investigations into the use of nanosheets as high surface electrodes have produced poor results. As shown in Figure 2.4(left), nanosheets were grown on carbon fiber paper for use in fuel cell applications. An attempt to deposit platinum catalyst, which is dispersed in a water solution, was then made resulting in extremely low loading of the catalyst material as illustrated by the lack of Pt present in the high resolution SEM image of Figure 2.4 (right). This was due to the extreme hydrophobic

behavior of the carbon nanosheets. The introduction of oxygen containing defects should offer control over the hydrophobicity of the material and permit the use of carbon nanosheets in a range of new applications. The experimental verification of acid-treatment created defects on carbon nanosheets is the focus of this research.

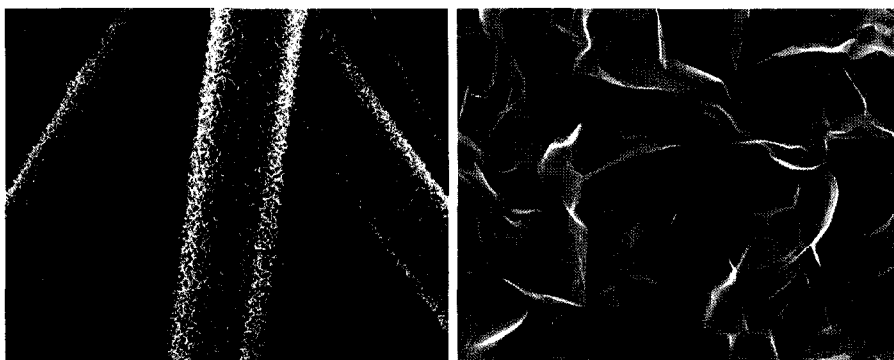


Figure 2.4: Carbon nanosheets were successfully grown on carbon fiber paper (left), but due to the extreme hydrophobic behavior of the nanosheet system, the Pt catalyst that is dispersed in a water solution was not successfully deposited on the nanosheets. This is illustrated by the lack of Pt in the SEM image (right).

2.3.1 Experimental setup for the functionalization of carbon nanosheets

The acid-treatment setup is shown schematically in Figure 2.5. The nanosheets are grown on tungsten and tantalum substrates and are then subjected to analysis via SEM and Raman. The substrate is then placed in a round bottom flask and approximately 3mL of concentrated hydrochloric acid (HCl) is added via pipette in such a manner as to keep the substrate from floating. The flask is then attached to a Gram-type condenser and lowered into the oil bath. The oil bath is kept around 100°C (+/- 5°C) and is stirred using a magnetic stir bar. The acid-treatment ranges from 3 hours to 24 hours and then the flask is removed from the oil bath and the acid removed via pipette with careful attention paid to not damaging the substrate. The flask is washed with 5mL of deionized water three separate times. Approximately 3mL of deionized water is then placed in the flask, again in such a manner as to keep the substrate from floating. After this simple acid treatment, the nanosheets are much more hydrophilic than before. The hydrophobicity is measured only by observation of the substrate's interaction with water. The flask is then returned to the condenser and the oil bath. The substrate is allowed to reflux in water overnight for a period of 15-20 hours. After refluxing, the substrate is removed from the flask and placed in an oven at 150°C for three minutes to dry. For the water-treated samples, the three hour reflux in acid was replaced with 3hrs in deionized water. The water was then removed and the flask rinsed. The substrates are also subject to the overnight reflux in deionized water. As can be seen in Figure 2.6 no apparent change in the morphology of the nanosheets can be seen in the SEM. As represented in Figure 2.7 however, an increase in the disorder of the graphene system can be seen via Raman spectroscopy as revealed with the increase in the D and $G'(2D)$ peaks and the reduction of the G peak.

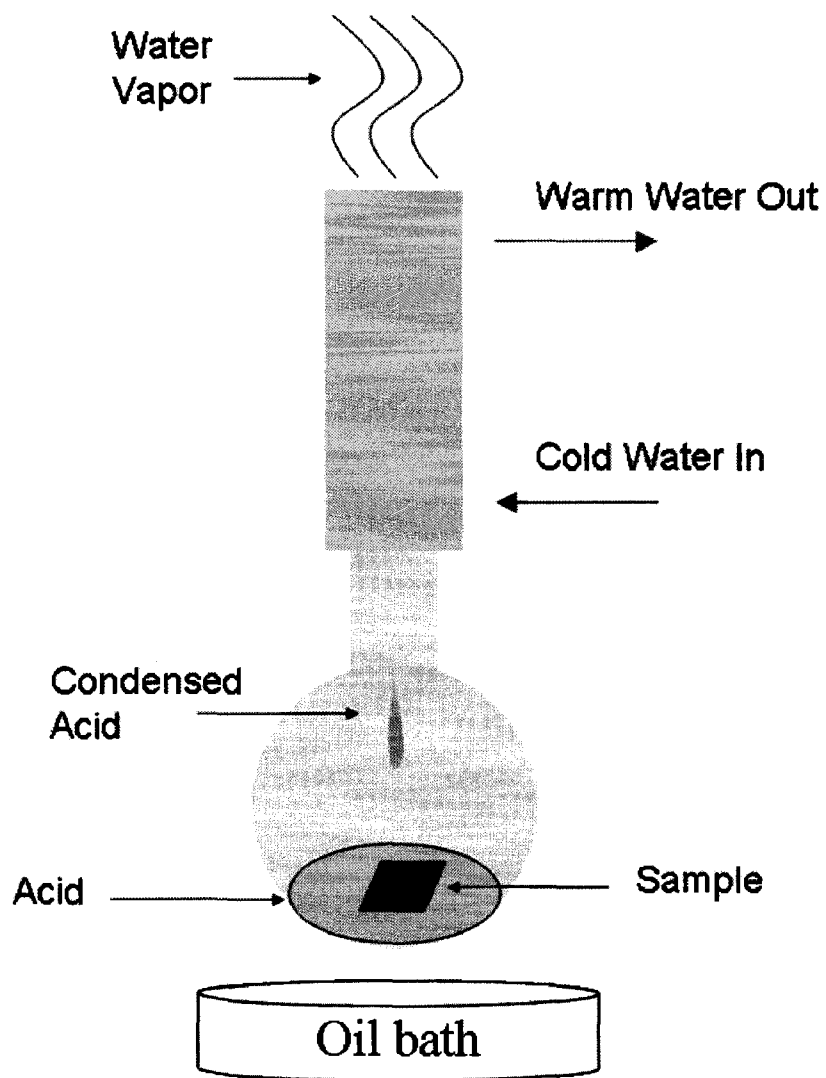


Figure 2.5: Schematic representation of the chemical hood setup used for the functionalization of carbon nanosheets.

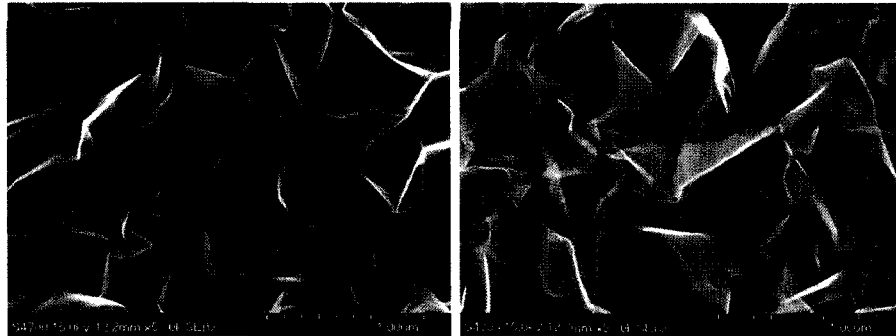


Figure 2.6: SEM micrograph of nanosheets before (left) and after (right) acid-treatment. The change in brightness is due only to the contrast settings on the SEM and not due to charging.

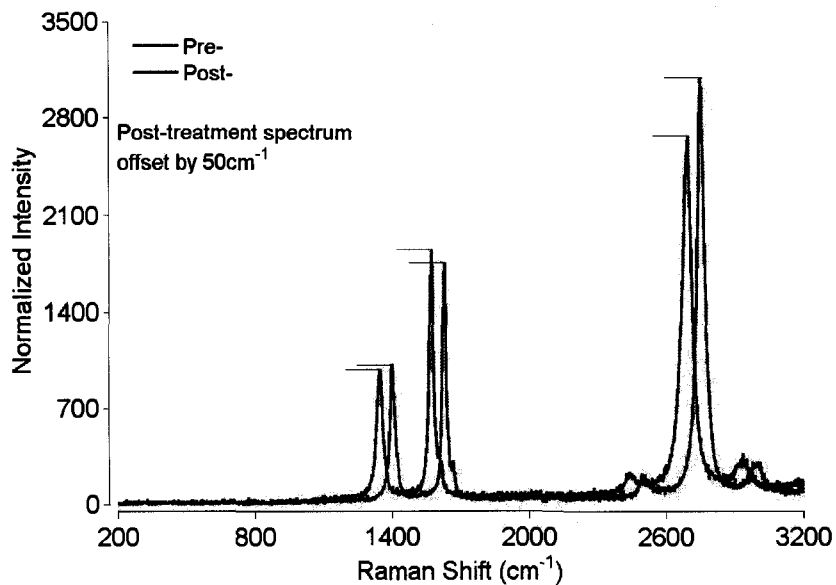


Figure 2.7: Raman spectrum of nanosheets on tantalum, pre- and post-acid treatment showing the detectable increase in disorder of the system after acid-treatment. This is expected with the creation of defects in the graphene lattice of the nanosheets. The spectra are offset for ease of viewing.

2.4 Scanning electron microscopy (SEM) and energy dispersive x-ray spectroscopy (EDS)

Zworykin *et al* are given credit for first developing the modern SEM in 1942. The first commercial instrument was developed in 1965 by Cambridge Scientific Instruments. SEM has now become one the most useful tools for the characterization of materials. Much like a traditional optical microscope the SEM creates a picture that allows the viewer to discern details from a three dimensional-like image that are too small to see with the naked eye. However, where as the resolution of an optical microscope is limited by the wavelengths of visible light (400nm - 800nm, enabling a resolution down to $\approx 200\text{nm}$) an SEM utilizes electrons to create the image, resulting in a much higher resolution ($< 1 - 5\text{nm}$). The resolution of the SEM is based on the de Broglie wavelength (λ) of the electron. The mathematical description is

$$\lambda = \frac{h}{m\nu} \quad (2.1)$$

where h is Plank's constant (6.625×10^{-34}), m is the mass of the particle and ν represents the velocity of the particle. From this equation, it is easily seen that a particle's wavelength is inversely proportional to its velocity and that as the velocity of the electrons is increased, the wavelength is decreased, which should allow for extremely high resolution. Other instrumentation limitations, such as the size of the focused electron beam, determine the resolution of the microscope.

During the operation of an SEM, the primary electron-beam strikes the sample, creating elastic scattering events which produce backscattered electrons and inelastic scattering events that are responsible for producing secondary electrons, auger electrons and characteristic x-rays (shown schematically in Fig. 2.8). Through the elastic interactions, the electrons from the beam are deflected by the atoms of the samples and can be deflected back out of the surface with a kinetic energy close to

that of the primary electron beam. These electrons are called backscattered electrons (BSEs) and can provide important information about the elemental makeup of the sample. At the same time, inelastic events are taking place as well. When this energy is transferred to the sample, some electrons near the surface can escape due to the large mean free path relative to their distance from the surface. These electrons, whose kinetic energy is not close to that of the primary beam, are called secondary electrons (SEs). Because the escape depth of SEs is small, as the beam energy is decreased, the interaction volume of the beam with the sample, the number of SEs increases. Though BSEs, Auger electrons, SEs and x-rays are present, usually the primary imaging mode utilizes the SEs, which can provide extremely high resolution images. These electrons are gathered by a collector and used to produce a 2D intensity distribution that can be viewed as a digital image. The image is created by the rastering of the primary electron beam and the variation in secondary emission coefficients (δ). If the beam is incident to the sample, a certain number of secondary electrons will escape the surface. As the beam moves over a feature and the angle of incidence increases, the escape depth will decrease on one side of the beam, producing more secondary electrons, which creates a brighter image. Therefore, sharp edges or surfaces will appear brighter in the image. This provides a very useful depth of field perception, allowing the viewer to discern important features of a sample's surface. A schematic representation of the components of an SEM is shown in Figure 2.9.

A Hitachi S-4700 field emission SEM (Fig. 2.10) was used for most of the sample imaging throughout the course of this study. A working distance of 12 mm provides a resolution as high as 2.1 nm at 1kV accelerating voltage and 1.5 nm at 15 kV. The S-4700 is capable of detecting secondary electrons, backscattered electrons, X-rays, and transmission electrons, making it a valuable instrument. However, the maximum voltage of the electron gun is only 30 kV so high resolution scanning transmission electron microscopy (STEM) is not possible in this instrument.

Also during the electron beam - sample interaction, some core electrons can be ejected from atoms due to the collisions, as also shown in Figure 2.8. When this occurs, a core level hole is created that is then filled with an electron from a higher energy level. This energy can then be released by ejecting another electron (Auger electrons) or by releasing x-rays. These x-rays have kinetic energies that are characteristic of the elements from which they originate, allowing for elemental identification by collecting these x-rays. These x-rays can be generated from a very deep region ($\approx 1\mu\text{m}$) compared to our thin carbon film. This process is called Energy Dispersive X-ray Spectroscopy (EDX). The EDX used in this work is an EDX PV 7746/61 with an energy resolution of ≈ 2.5 eV. It is shown in the top left of Figure 2.10.

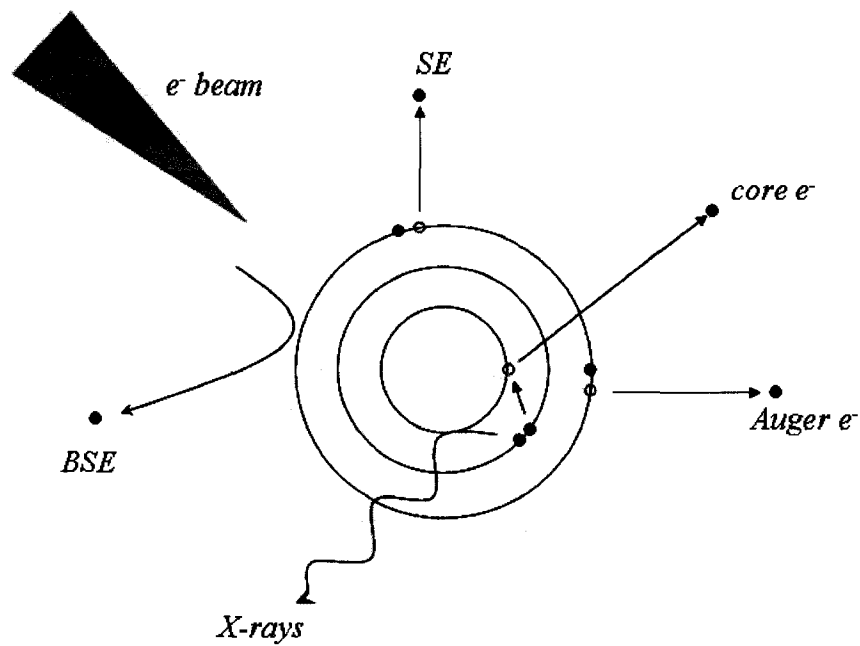


Figure 2.8: The different signals resulting from the electron beam interactions with the atoms of the sample are shown schematically. Backscattered electrons and secondary electrons are represented by BSE and SE respectively. The holes left by leaving electrons are represented by the red rings. The characteristic x-rays utilized during EDS are represented by the wavy blue line and are denoted X-rays in the schematic.

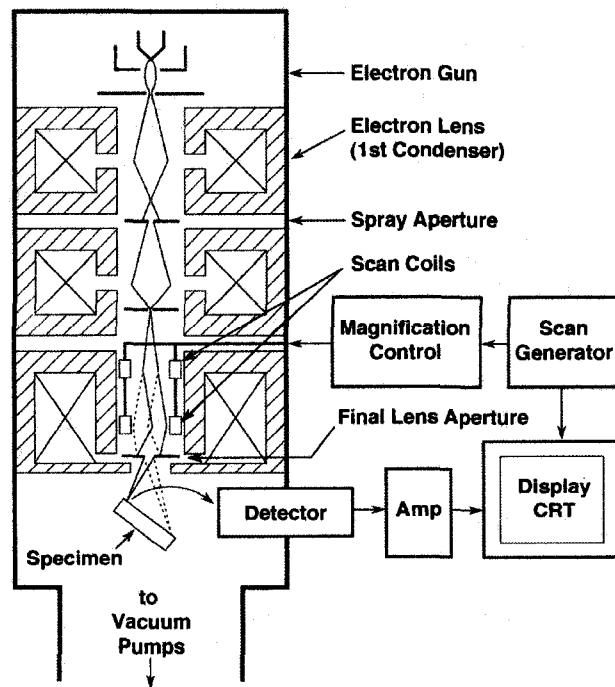


Figure 2.9: Schematic representation of the major components of a typical scanning electron microscope [29].

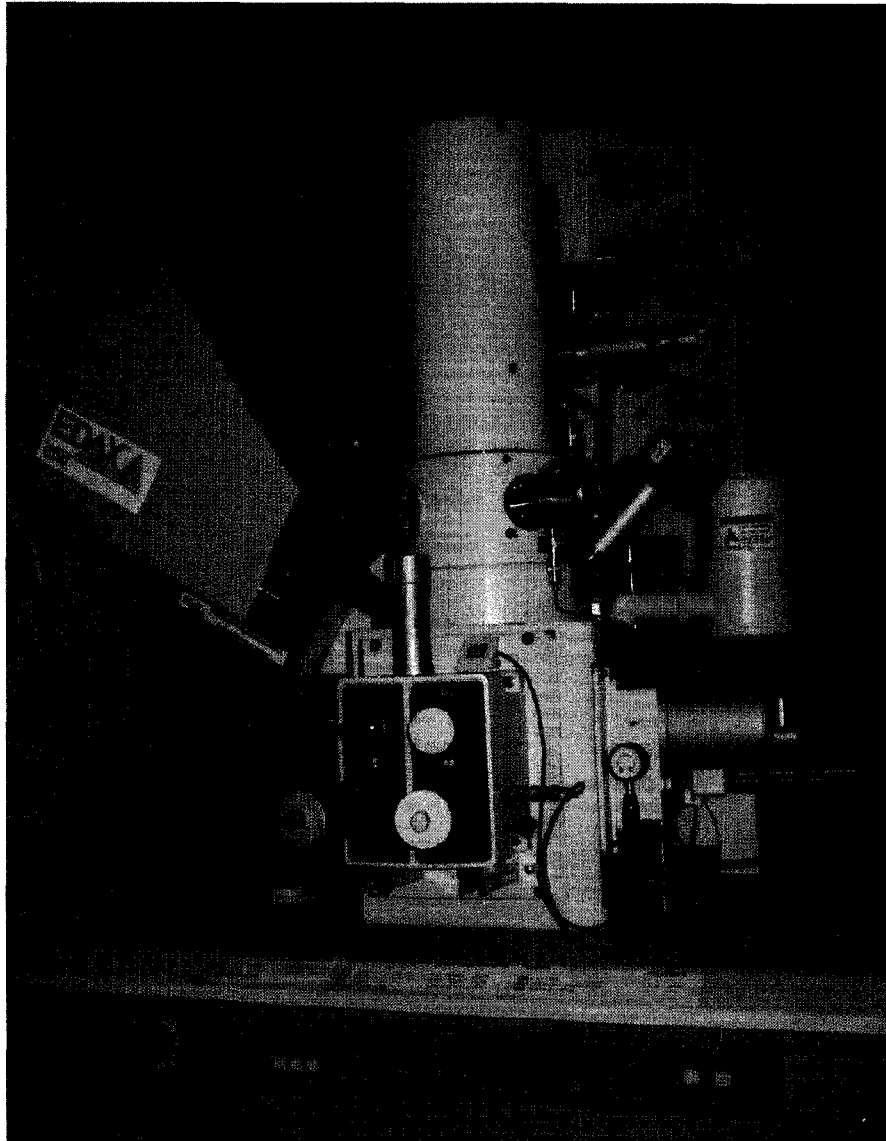


Figure 2.10: Digital picture of Hitachi S-4700 located in Small Hall at the College of William and Mary. The EDS is labeled EDAX in the top left of the image.

2.5 Introduction to Raman spectroscopy

Indian physicist, Chandrasekhara Venkata Raman, is given credit for first discovering the radiation effect known as the Raman Effect in 1928. The discovery of this effect led to the development of the now widely used Raman Spectroscopy. Raman spectroscopy is based on the inelastic scattering of monochromatic light: in most modern systems a laser. As the sample is irradiated, the laser interacts with the phonons of the material and excites them into a virtual state that is below the first excited electronic state. Relaxation of the material produces three types of scattering: Rayleigh, Stokes and anti-Stokes. If the scattering is of the same energy as the incident photon, i.e. it is excited from a ground electronic state and relaxes to the same ground electronic state, it is called Rayleigh scattering. If the material is excited from the ground electronic state and relaxes to an excited vibrational state, the scattering is called Stokes. If the lattice was already in an excited vibrational state and then relaxes to the ground state, the scattering is called anti-Stokes (see Fig. 2.11). Because the number of phonons in an excited vibrational state at room temperature is small, the signal for anti-Stokes scattering is very small and the measurements are rarely used. It is important to note that the shifts of the Stokes and anti-Stokes from the Rayleigh line are identical and equals ΔE in Figure 2.11. Both peaks are much less intense than the Rayleigh line and the anti-Stokes less intense than the Stokes.

In order for the material to be Raman active a molecular polarizability change with respect to the vibrational coordinate is required. The amount of the change will determine the intensity of the peaks while the Raman shift is determined by the vibrational level involved. The vibrational information of a molecule is very specific for particular molecules. Therefore, Raman is very effective as a fingerprint or quality control technique. It should be noted that while the intensities of the peaks observed during Raman depend on the absorption coefficient of the material for the particular wavelength of laser being used, the Raman shifts do not depend upon the excitation

wavelength of the laser.

Raman spectroscopy has also been shown to be a particularly useful tool in determining the disorder of carbon based systems. Graphite crystals exhibit two features in a Raman spectrum, the E_{2g2} mode at 1582 cm^{-1} , the $G - band$, and under special conditions the E_{2g1} at 42 cm^{-1} . However, even a modest amount of disordered carbon gives rise to another feature around 1350 cm^{-1} , known as the $D - band$ [30]. The ratio between the two bands can be used to characterize different types of *it sp*² carbon, such as carbon fibers, carbon nanotubes and ion implanted carbons. This ratio ($R = I_D/I_G$) can also be related to the in-plane crystallite size [31], which is normally determined by x-ray diffraction measurements [30].

The Raman setup used in throughout this study was an inVia dispersive Raman (Renishaw, Inc.) with three laser sources and four different wavelengths (488 nm and 514 nm from an Ar⁺ ion laser, 633 nm from a He-Ne laser and 785 nm from a diode laser). Our setup utilized a charge-coupled device (CCD) detector. A schematic of the major components of a typical Raman instrument is provided in Figure 2.12.

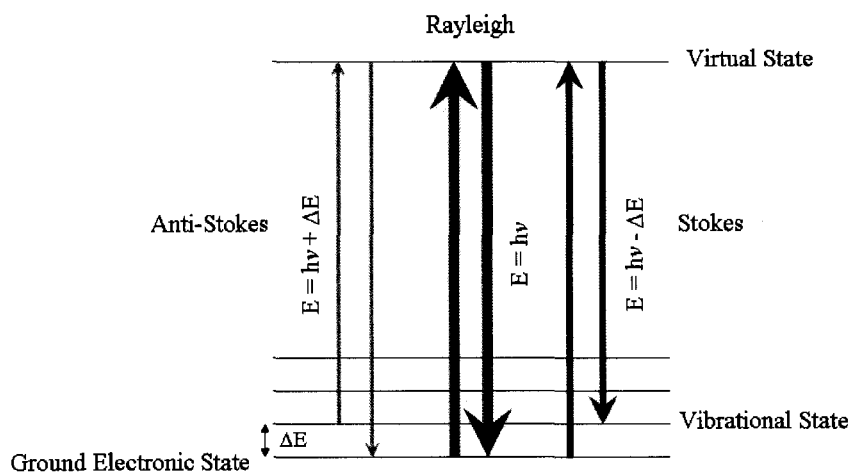


Figure 2.11: Raman Spectroscopy involves the inelastic scattering of monochromatic light. The green lines represent the Anti-Stokes scattering, the red represent the Rayleigh scattering and the blue lines represent the Stokes scattering events.

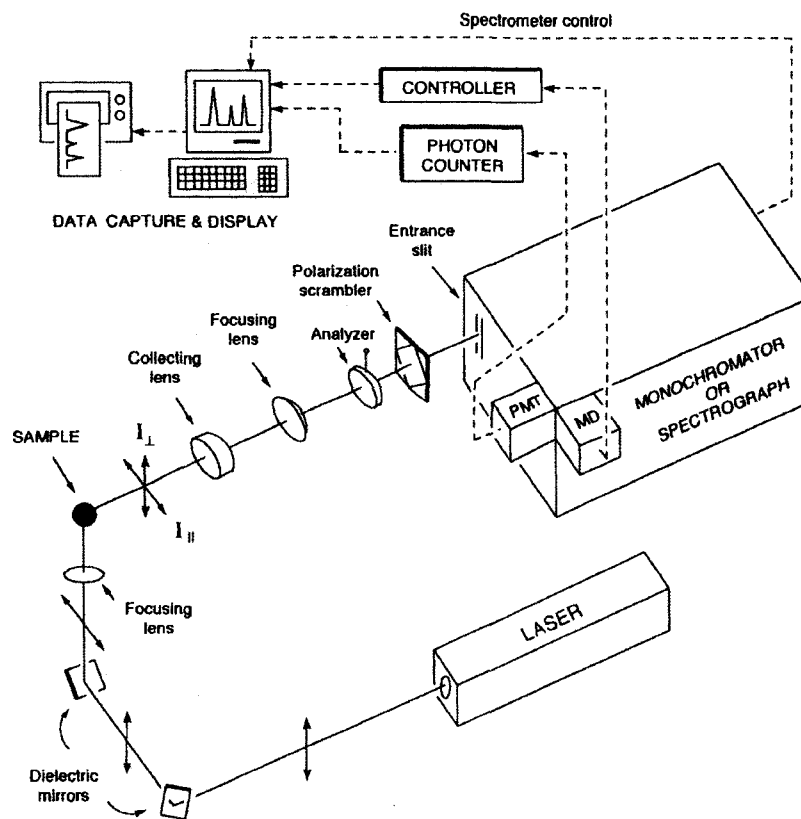


Figure 2.12: Schematic representation of the major components of a typical Raman spectrometer [32]. During this study a Renishaw Raman spectrometer was used, located at the College of William and Mary.

2.5.1 Experimental use of Raman spectroscopy

For the purpose of this study, Raman has been used mainly as a quality control instrument. Complete investigation via Raman has been reported by our group previously [6, 7]. As can be seen in Figure 2.13, nanosheets possess similar spectra to that of carbon nanotubes (Figure 2.14). The *D* band (1350 cm^{-1}), the *G* band (1580 cm^{-1}) and the *D'* band (the shoulder on the *G* band at $\approx 1620\text{ cm}^{-1}$) which have all been previously recognized in microcrystalline graphite [31, 33] identifying nanosheets as having a crystalline, but defective graphitic structure. It is also important to note that I_D/I_G (the intensity ratio of the *D* to *G* peak) can be used to determine the relative crystallinity of the nanosheet samples [6, 33], but only holds true for laser excitation wavelengths around 514 nm. Therefore, with little to no damage to the sample, it can be compared to previous samples for analysis. The effects of procedures such as the transfer process (Chapter 5), the functionalization (Chapter 2.3) or vacuum firing (Chapter 2.10) can be quickly and easily investigated without damaging the nanosheet film.

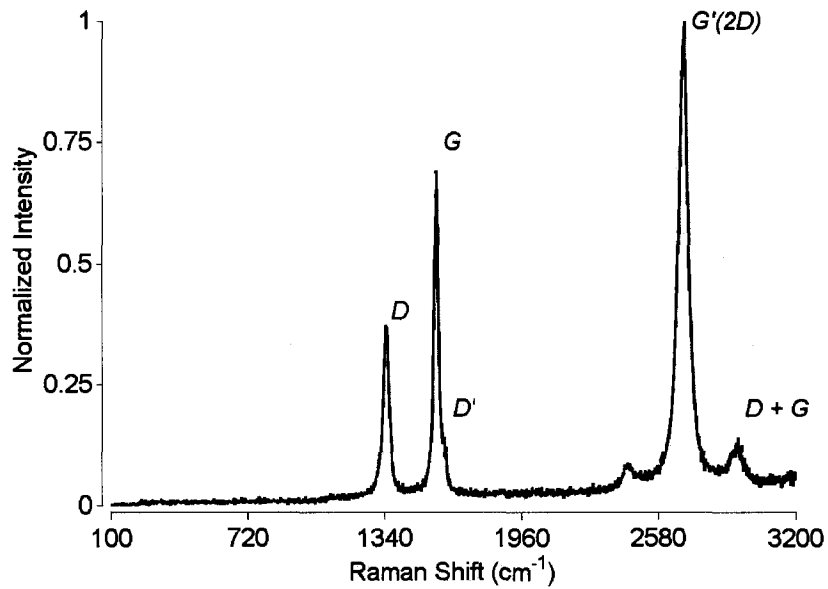


Figure 2.13: Raman spectrum of a typical nanosheet sample. The laser excitation wavelength utilized is 514nm. The ratio of the *D* and *G* peaks is commonly used for the determination of quality for a particular sample.

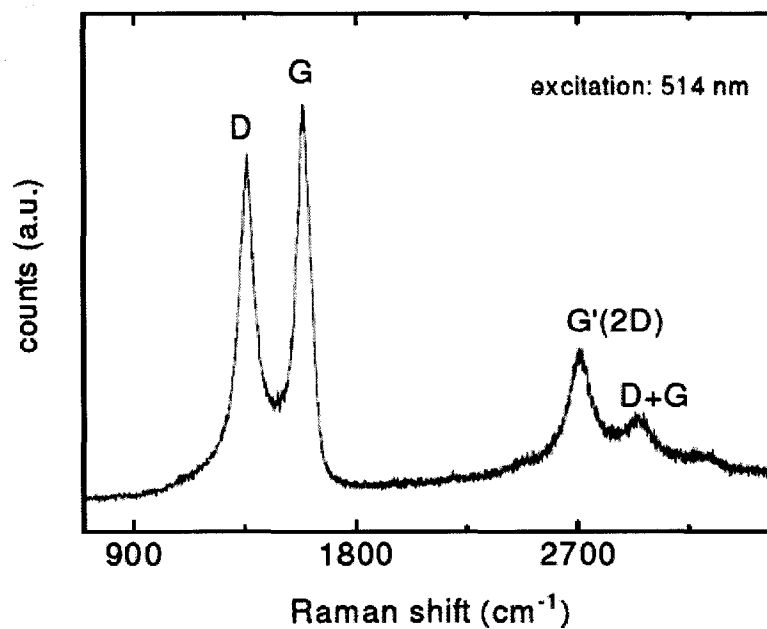


Figure 2.14: Raman spectrum of typical carbon nanotube sample for comparison to carbon nanosheets [20].

2.6 Fourier transform infrared spectroscopy (FT-IR)

Infrared spectroscopy is another method used to gather information about the chemical structure of materials by measuring vibrations in the sample. However, unlike Raman, in order for a vibration to be active in the infrared region, the vibration must involve an oscillation in the electric dipole moment. Multiplex instruments—techniques in which all the components of the response are collected simultaneously—rely on the *Fourier transform* (FT) for signal decoding. There are three main advantages of using a FT instrument. The first is the *throughput*. Because FT instruments have no slits to attenuate radiation, the power of the radiation that reaches the detector is much higher than that in dispersive instruments, resulting in a much higher signal to noise ratio. The second advantage is the high resolving power and wavelength reproducibility. The third advantage is the time involved. All elements of the source reach the detector simultaneously allowing for an extremely quick collection time.

From a mechanical perspective, systems can be thought of as masses (atoms) connected by springs (chemical bonds). These systems can absorb energy and thereby certain frequencies are excited. These frequencies can be described in the simple-harmonic-oscillator approximation of two atoms (Eq. 2.2) of mass m and M , where k is the force constant and μ is the reduced mass (defined by Eq. 2.3).

$$\nu_m = (2\pi)^{-1} \left(\frac{k}{\mu} \right)^{1/2} \quad (2.2)$$

and

$$\mu = \frac{m_1 m_2}{(m_1 + m_2)} \quad (2.3)$$

Therefore, the vibrational frequencies for a two mass system connected by a spring can be related by

$$\nu_m = (2\pi)^{-1} \left\{ k \frac{(m_1 + m_2)}{m_1 m_2} \right\}^{1/2} \quad (2.4)$$

While these calculations are fairly accurate, they do not completely describe the system, such as the quantized nature of the molecular vibrational energies. However, this can be developed by utilizing potential energy equations of the form

$$E = \left(\nu + \frac{1}{2} \right) \left(\frac{h}{2\pi} \right) \left(\frac{k}{\mu} \right)^{1/2} \quad (2.5)$$

where h is Planck's constant and ν is the vibrational quantum number, which can only be a positive integer including zero. This means that quantum mechanical vibrators can only take discrete values. Therefore, the difference between vibrational levels is identical and is given by the equations 2.6 and 2.7

$$\Delta E = \left(\frac{h}{2\pi} \right) \left(\frac{k}{\mu} \right)^{1/2} \quad (2.6)$$

$$\Delta E = h\nu_m \quad (2.7)$$

and because the energy of radiation is given by

$$E_{radiation} = h\nu \quad (2.8)$$

it follows that the frequency of the radiation (ν) that will excite the classical vibrational frequency of the bond (ν_m) can be expressed as a combination of these equations as

$$E_{radiation} = h\nu = \Delta E = h\nu_m = \left(\frac{1}{2\pi} \right) \left(\frac{k}{\mu} \right)^{1/2} \quad (2.9)$$

or

$$\nu = \nu_m = \left(\frac{1}{2\pi} \right) \left(\frac{k}{\mu} \right)^{1/2} \quad (2.10)$$

If we want to express the frequency as a wavenumber we simply divide the frequency (ν) by the speed of light (c) as illustrated in equation 2.11. The use of (2.9) along with experimental values for ν allow for the calculation of the force constant for systems (k) which is of course a measure of the stiffness of a bond [20, 34].

$$\nu = \frac{c}{\lambda} \quad (2.11)$$

2.6.1 Experimental setup of the FT-IR for the inspection of functionalized nanosheets

For the purpose of these experiments, nanosheet samples were pressed into KBr pellets and analyzed using a Nicolet Nexus 670. Analysis of typical nanosheet systems were previously completed and reported [20]. The nanosheets used in this experiment were grown on tungsten foil substrates as previously described (section 2.2.1) and then subjected to acid-treatment as described in section 2.3.1. The samples utilized for this experiment were treated for 3 hours. After acid-treatment, the nanosheets were removed from the growth substrate with a razor blade and pressed into the KBr pellets. Reference samples were as-deposited nanosheets prepared in the same manner. A schematic of a typical FT-IR is provided in Figure 2.15.

Results representative of the FT-IR of functionalized carbon nanosheets are shown in Figure 2.16. As is expected for the nanosheet system, C-H stretching is observed in the range of 1340 - 1470 cm^{-1} . Also illustrated is the stretching of a C-O bond found in alcohols, ethers, esters and carboxylic acids (1000 - 1260 cm^{-1}). Though these signals are not strong enough to make an identification of the functional groups alone, these results support the results that will be discussed in Chapter 3. A spectrum of

as-deposited nanosheets can be found in reference [20].

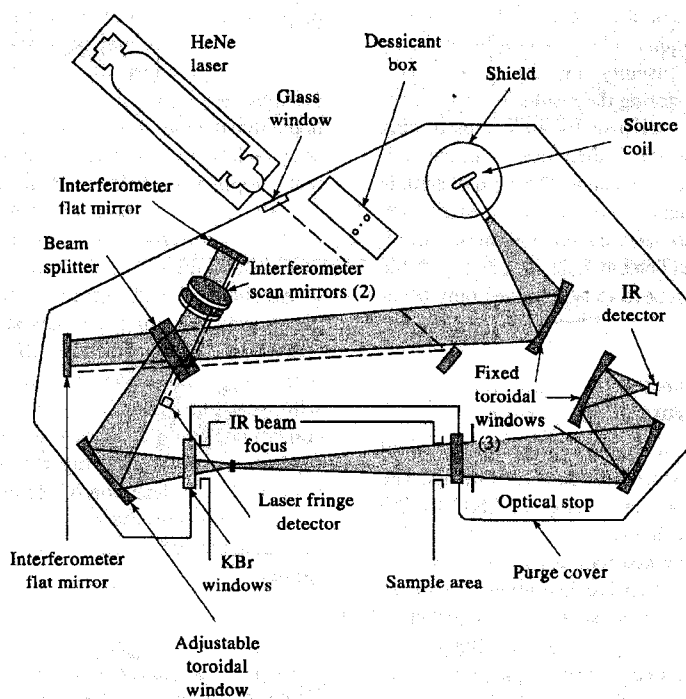


Figure 2.15: Schematic representation of a Fourier Transform Infrared Spectrometer [34].

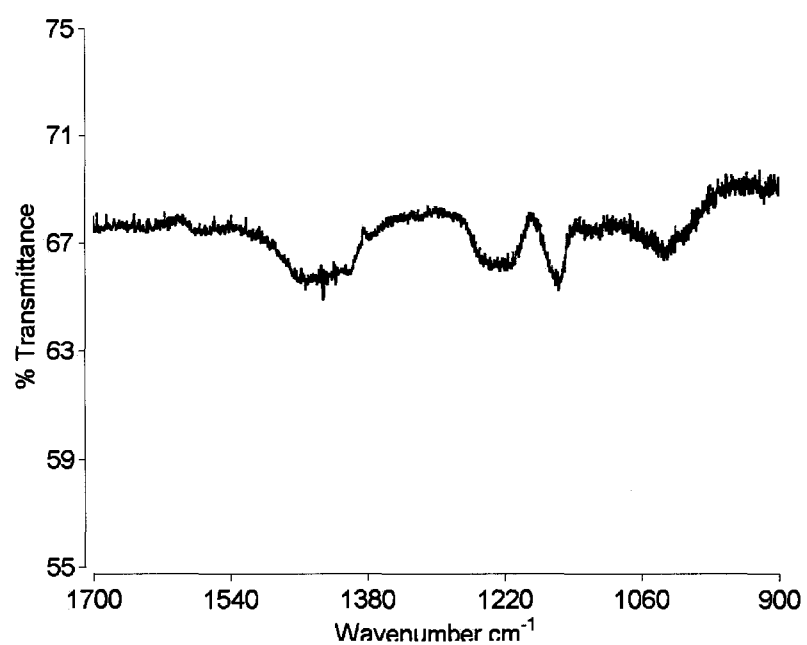


Figure 2.16: Typical FT-IR spectrum of functionalized carbon nanosheets. As can be seen, stretching for the C-H bonds in the nanosheet system is illustrated by the peak in 1340 - 1470 cm^{-1} . The stretching associated with C-O bonding of alcohols, esters, ethers and carboxylic acids (1000 - 1260 cm^{-1}).

2.7 Four-point probe

The four-point probe is a quick and easy way to determine the sheet resistance of a thin film material that can then be used to determine the resistance of the material. For our setup, four metal tips, which are part of auto-mechanical stage, are placed in contact with the sample. The force of the tips can be adjusted via springs that connect the tips to the stage. A schematic of the probe setup is shown in Figure 2.17 below. During the experiment, a current is passed through outer two probes while the inner two probes measure the voltage drop to determine the resistivity.

In this work, the sheet resistance of the basal layers was measured. This measurement was made before and after the transfer of nanosheet films to determine the success of the process (section 5.4).

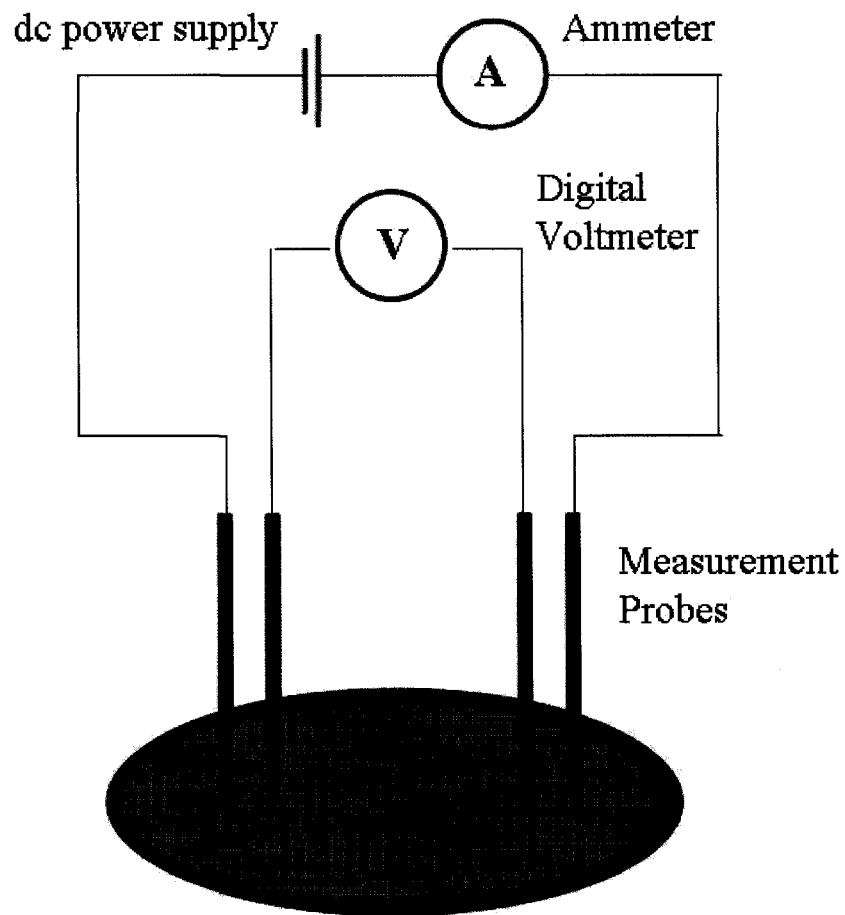


Figure 2.17: Schematic illustration of the four-point probe setup. The gray disc represents the transferred nanosheet film and the red disc represents the polymer substrate.



Figure 2.18: Photo of the four-point probe setup utilized at Luna Innovations Incorporated, Advanced Materials Division, Blacksburg, VA. Picture provided via courtesy of Dr. Jonas Gunter.

2.8 X-ray absorption near-edge spectroscopy (XANES)

X-ray absorption near-edge spectroscopy, or XANES, is a form of x-ray absorption spectroscopy (XAS) that is differentiated from extended x-ray absorption fine structure (EXAFS) – which considers the absorption spectrum out to much higher electron kinetic energies – by its energy range and is illustrated schematically in Figure 2.19. The near-edge region is normally considered the range between the absorption threshold and about 50eV above the threshold. This is about the range where the wavelength of the excited electron is equal to the distance between the absorbing atom and its nearest neighbors [35]. Therefore, the difference between the near-edge (XANES) and the extended fine-structure (EXAFS) is that the photoelectron generated by the absorption of x-rays undergoes multiple scattering events in the XANES experiment and only a single scattering event during the EXAFS experiment.

Most XANES experiments are completed at synchrotron sources where the x-ray beam energy can be easily tuned. During the experiment, the beam energy is scanned across a region of interest and either the electrons or fluorescence of the sample measured. This process is shown schematically in Figure 2.20. As depicted in the figure, when the x-ray is absorbed, a core level electron is ejected (the photoelectron) creating a core level hole and an electron from a higher energy level relaxes to fill the hole. This energy can either be released as fluorescence or by emitting another electron from a higher level, known as the Auger electron.

For XANES experiments, we can measure either the fluorescence yield or electron yield. During fluorescence yield measurements, the photons emitted during the relaxation of the absorbing atom are measured. However, the diode sensitivity is not as good and other events, such as scattering, can affect the measurements. Therefore fluorescence is not normally measured. The electrons can be measured in two ways, total electron yield (TEY) or partial electron yield (PEY). During the PEY mode the low energy electrons are filtered out. This is useful if trying to obtain depth

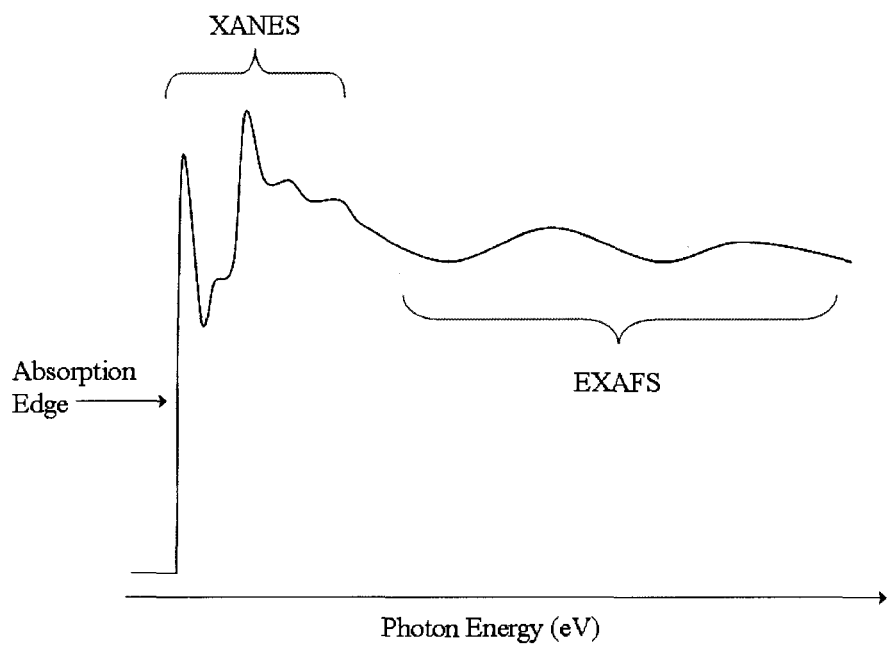


Figure 2.19: Schematic representation of the energy ranges for near-edge (XANES) versus extended (EXAFS) absorption. The schematic is not drawn to scale or for any particular system.

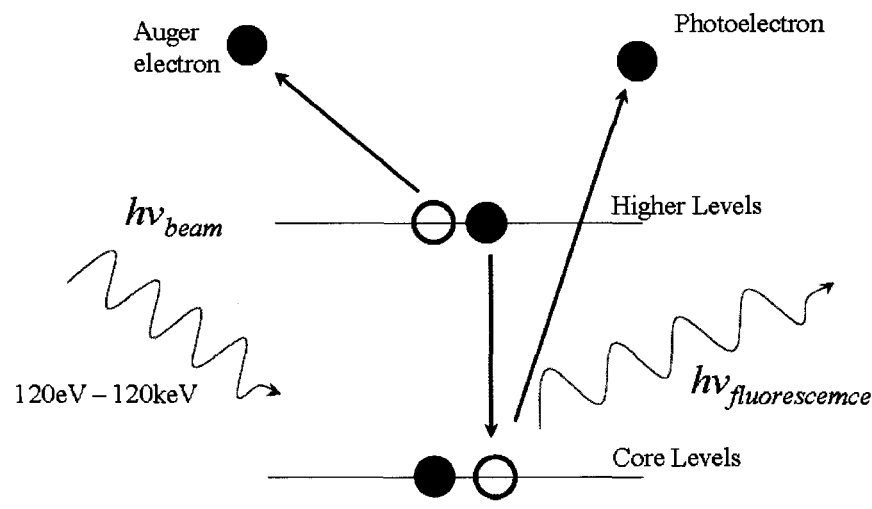


Figure 2.20: Schematic representation of x-ray absorption. As the x-ray photon is absorbed by the atom, a core-level electron is ejected (photoelectron, red dot), leaving behind a core-hole (red circle). This hole is filled by an electron from a higher energy level, resulting in the emission of a fluorescent photon (bright green arrow) or of an Auger electron (blue dot).

sensitivity. For the purposes of these experiments, TEY mode was utilized because there was no concern about depth profiling. This measurement is basically measuring all the electrons ejected from the sample.

As the energy of the beam is scanned, the transitions of core electrons to unoccupied states can be seen by the absorption of the x-rays. A schematic of these transitions for a theoretical C-C system are shown schematically in Figure 2.21 and Figure 2.22. These transitions can be measured against known materials, such as highly oriented pyrolytic graphite Figure 2.23, for comparison. When the atoms have different chemical environments, the energy levels will shift, resulting in corresponding shifts of the measured transitions.

Our XAS experiments were conducted at beamline D1011 at MAX II, MAX-Lab, Sweden with a modified SX-700 plane grating monochromator as shown in Figure 2.24.

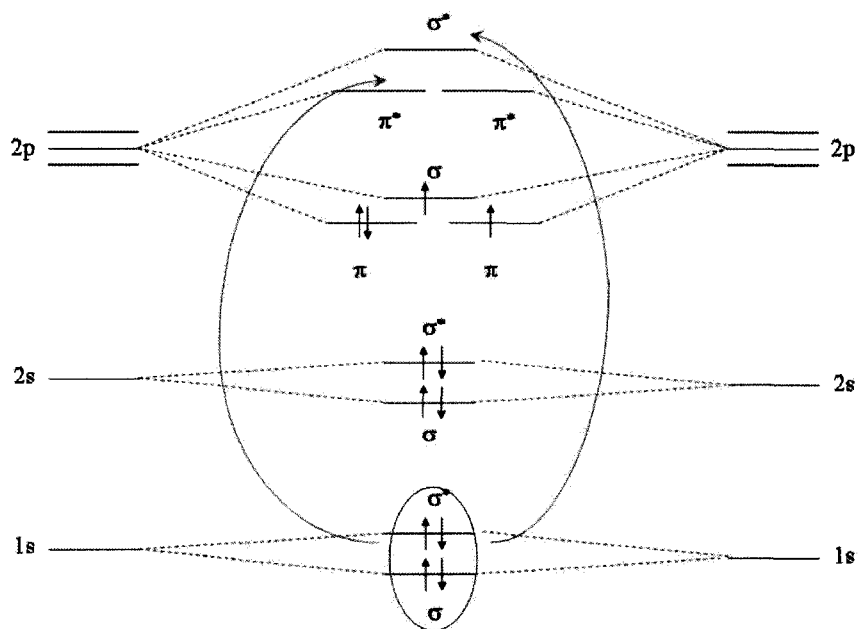


Figure 2.21: Molecular orbital diagram of C-C system. The transitions from core levels to π^* and to σ^* levels are marked by the green arrows. These transitions are seen in a typical XANES spectrum of a graphite system (Fig. 2.23) at 285 eV and 291 eV respectively. The schematic is not drawn to scale and is representative of the transitions on a molecular scale.

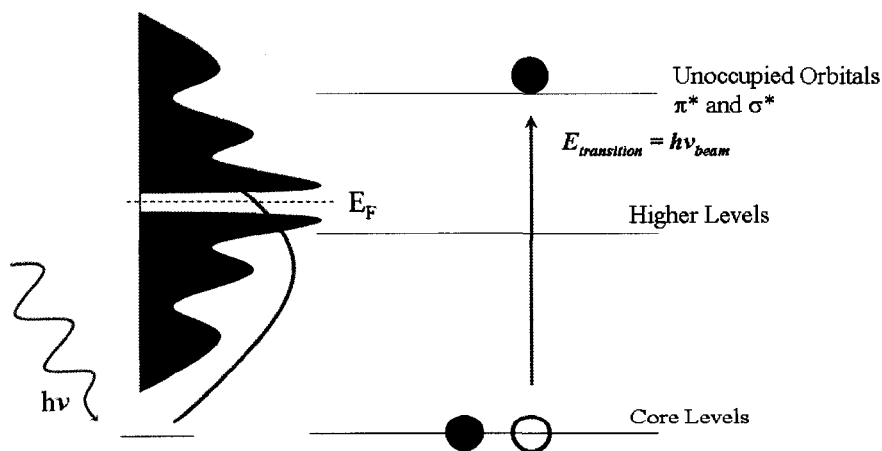


Figure 2.22: Absorption of the x-ray in XANES spectrum. The core electron is excited to an unoccupied orbital, either the π^* or σ^* transition. As the chemical structure of the sample changes, so will $E_{transition}$.

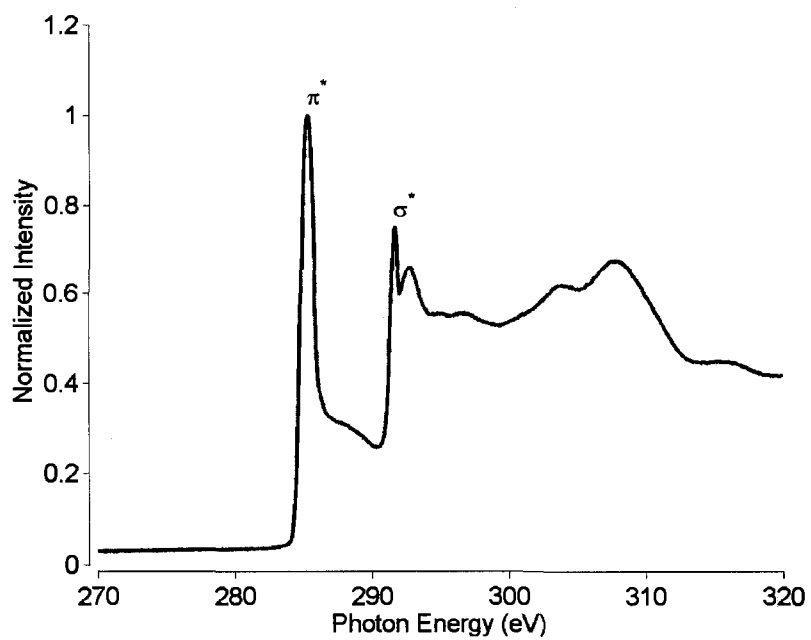


Figure 2.23: XANES spectrum of highly oriented pyrolytic graphite. The two predominate peaks at 285 eV and 291 eV are the result of π^* and σ^* transitions respectively.

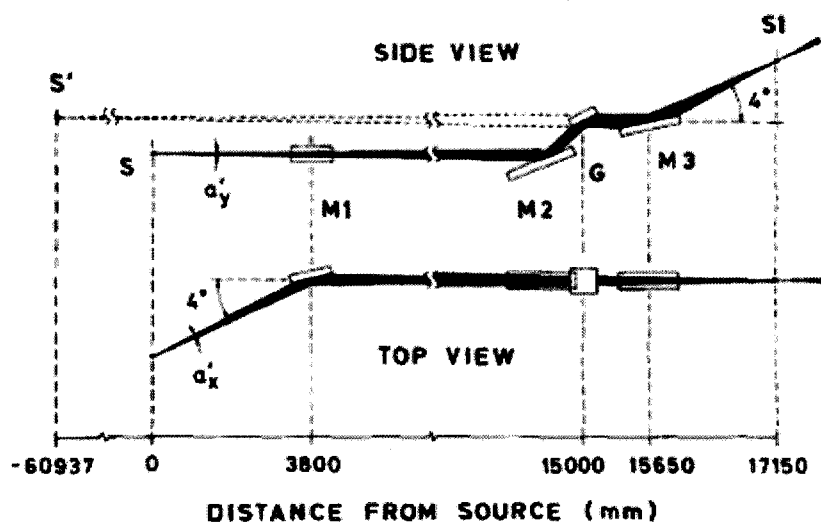
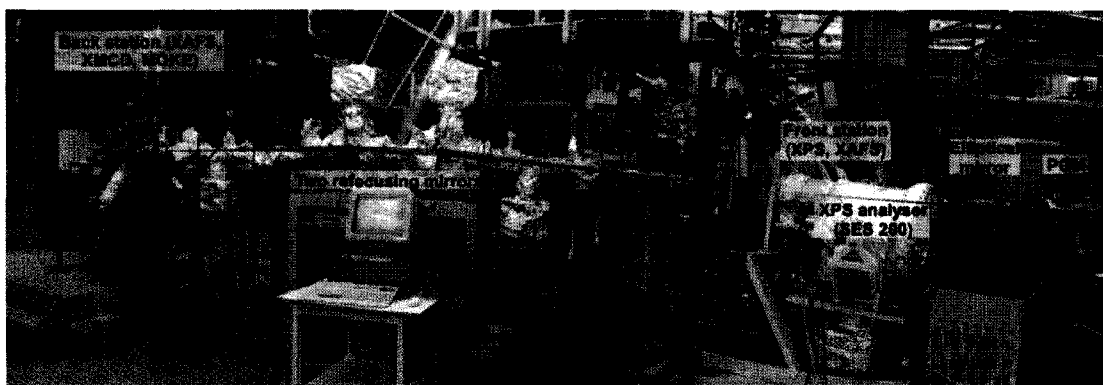


Figure 2.24: A digital image (top) and schematic [36] (bottom) of the beamline D1011 at MAX II, MAX-Lab, Lund, Sweden. The measurements were made in the back station, labeled in the upper left of the image. Samples were also loaded into the front station (right side) for analysis, but the spectra gathered from the front station are not capable of being corrected by the incident beam. Image is taken from the beamline's website - <http://www.maxlab.lu.se/beamlines/bld1011/>

2.8.1 Experimental setup for the investigation of functionalized nanosheets using XANES

Angular dependent XANES measurements about the carbon K-edge and preliminary theoretical modeling were utilized to study the defects created in the graphene planes of the nanosheets. These defects were intentionally created using the treatment described in 2.3.1 for the purposes of taking the first step towards improving the functionalizing graphene and graphene-like materials for new properties in the materials.

For these experiments, the nanosheets were grown via RF PECVD as previously described (section 2.2.1) on tungsten foil (0.1mm thick). The substrates were inspected ex-situ via Raman and SEM techniques for verification of growth quality before functionalization. The samples used include the 3hr acid-treated sample, the 3hr water-treated sample and as-deposited samples.

Prior to all measurements, the samples were heated *insitu* to 170°C overnight to remove surface absorbates. The measurements around the C K-edge were recorded in total electron yield (TEY) mode. Measurements were made with the incident beam perpendicular to the surface (0°) and at grazing angles (45° and 70°). The incident photon flux was monitored on a clean Au grid and was used to correct the XANES spectra. Spectra were pre-edge normalized at 270eV, a linear background was subtracted and then post-edge normalized at 320eV. Peak identification was based on the known value for copper (cleaned Cu sample holder, see Fig. 2.25).

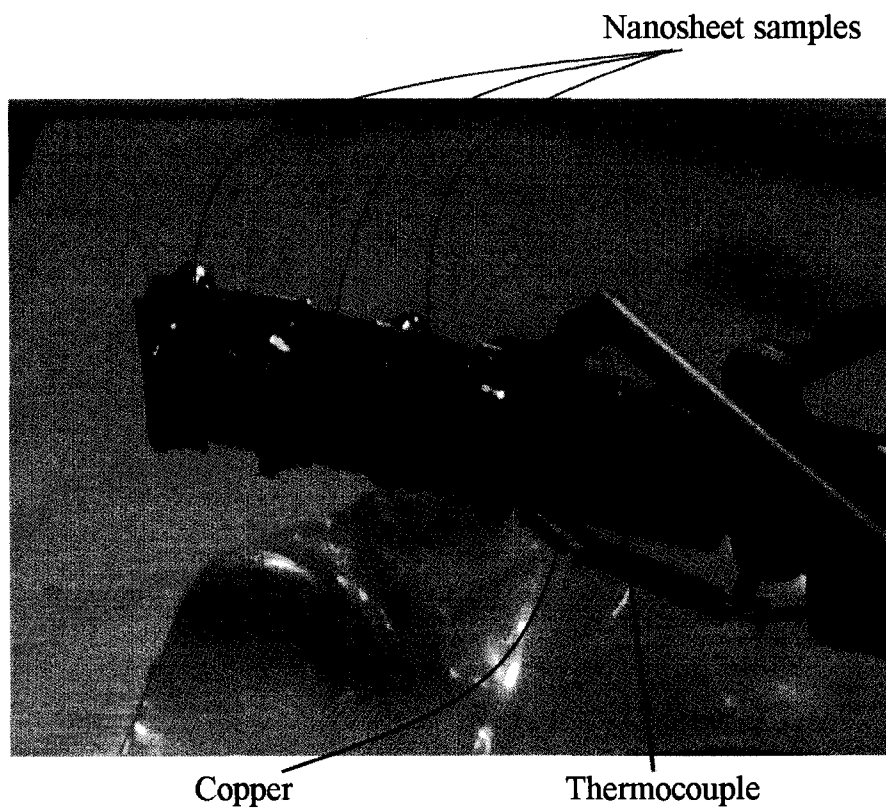


Figure 2.25: Photograph of the copper sample holder used for the x-ray adsorption analysis of as-deposited and functionalized nanosheets.

2.9 Thermal desorption spectroscopy (TDS)

Thermal desorption spectroscopy (TDS), also known as temperature programmed desorption (TPD), is a method used to measure the activation energy for desorption (ΔE_d) from a material's surface. In order to obtain this information experimentally, the material of interest is heated in ultra-high vacuum (UHV) with a linear temperature (T) ramp in the time domain. As the temperature increases, atoms and molecules on the surface of the material will increase in energy, allowing for surface diffusion, recombination and finally desorption from the surface. The partial pressure variations of these adsorbates is recorded by a mass spectrometer. When the pressure of adsorbates is plotted versus the time, a TDS spectrum is obtained. The mass spectrometer is capable of analyzing several mass/charge ratios during the experiment, allowing for the identification of several different species within a 25 ms period. A schematic of the experimental setup is provided in Figures 2.26 and 2.27. A digital image of a sample holder is provided in Figure 2.28.

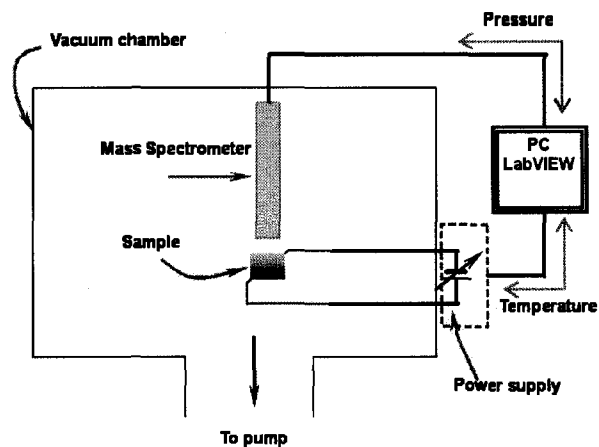


Figure 2.26: Schematic representation of the TDS experimental setup.

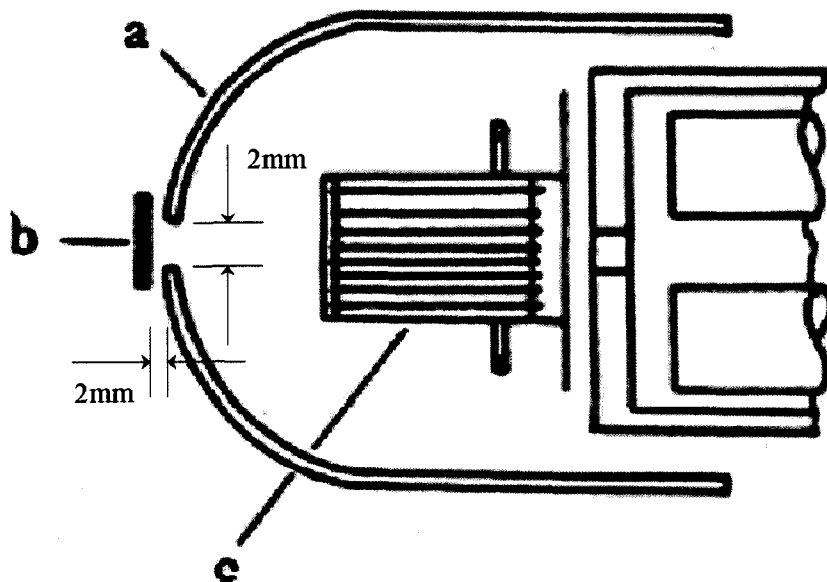


Figure 2.27: Schematic of Feulner and Menzel cup used (2mm diameter aperture) for enhanced resolution of TDS spectra. The cup is labeled (a), the sample (b) and the mass spectrometer (c).

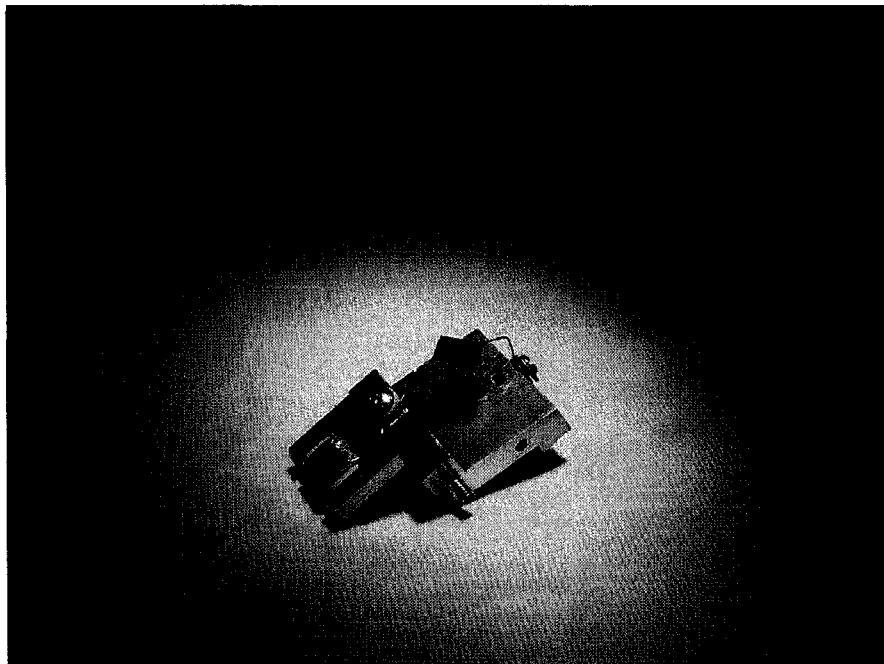


Figure 2.28: Photograph of the custom sample holder with sample used during the TDS experiments. The sample holder is mounted on a carousel and is then placed below the appeture of the Feulner and Menzel cup (as depicted in Fig. 2.27)

2.9.1 Experimental use of TDS for the inspection of functionalized carbon nanosheets

Due to the complexity of the curve that is obtained, a theoretical model is required for the specific desorption process. The desorption process is a sequence of surface reactions. For instance, as reported in [37] and [38], the focus was on the desorption of H₂ molecules which contains three surface reactions—the surface diffusion of H atoms, the recombination of the H atoms and the desorption of H₂ molecules—described by the Langmuir-Hinshelwood mechanism [39].

The rate of desorption (r_d) can be expressed as

$$r_d = k_d \cdot \theta^n \quad (2.12)$$

where k_d is the rate constant, θ is the adsorbate fractional coverage and n is the kinetic order of desorption ($n = 1$ for thermal decomposition and $n = 2$ for recombination desorption). The rate constant (k) can be expressed in Arrhenius form,

$$k_d = \nu \cdot e^{\left(-\frac{\Delta E_d}{kT}\right)} \quad (2.13)$$

where ν is the pre-exponential factor, k is Boltzmann's constant, ΔE_d is the activation energy of desorption, t is time and T is the temperature in Kelvin. Equations (2.12) and (2.13) are combined to form the Polanyi-Wigner equation

$$r_d = -\frac{d\theta}{dt} = \nu \cdot \theta^n \cdot e^{-\left(\frac{\Delta E_d}{kT}\right)} \quad (2.14)$$

where $(-d\theta/dt)$ is the desorption rate. The pre-exponential factor (ν) represents the total probability of desorption per second and is related to the adatom's vibrational frequency on the surface. Because each stretching movement of an adsorbate-surface bond in vibrational mode can be considered an attempt to break the bond, the frequency of the strength movement is equivalent to the total probability of desorption

per second. Equations (2.12) through (2.14) are the basis of the mathematical model used to deconvolute TDS data.

However, during the TDS experiments, the partial pressure is measured. The partial pressure is related to the desorption rate via

$$-V \left(\frac{dp}{dt} \right) + Q = S \cdot p \quad (2.15)$$

where V is the volume of the chamber, Q is the mass flow rate of desorption, S is the pumping speed and p the pressure. For our system, the pumping speed to volume ratio is so large that $dp/dt \ll (S/V)p$, allowing us to ignore the contribution of $-V(d\theta/dt)$ [37]. Equation (2.15) can then be reduced to

$$Q \approx S \cdot p \quad (2.16)$$

Assuming a single desorption energy for each mass to charge unit in question (e.g., CO₂, CO and H₂O) the desorption processes follow the Polanyi-Wigner equation (Eq. 2.14) [40]. The desorption rate is then given by

$$r(\theta) = - \left(\frac{d\theta}{dt} \right) = \nu \cdot \theta^n \cdot e^{\left(-\frac{\Delta E_d}{kT} \right)} \quad (2.17)$$

with the variables represent the same values as mentioned before. Combining (2.16) and (2.17), the partial pressure (p_i) and adsorbates fractional coverage (θ) of a species can be related by

$$p_i = C \cdot N_i \cdot \left(-\frac{d\theta_i}{dt} \right) \quad (2.18)$$

where C (Torr · sec) is a constant and N_i represents the total number of atoms diffusing with the same desorption activation energy. For ease of numeric computation in our process, p_{max} was scaled by arbitrary units so that p_{max} is set to 1000. The

relationship between the temperature (T) and time (t) is

$$T = 300 + \alpha \cdot t \quad (2.19)$$

where T is in Kelvin and α is the temperature ramp rate (for our system 10 K/sec).

Combining (2.17 - 2.19) we get equation

$$P_{total}^*(T) = \left(\frac{K \cdot C}{\alpha} \right) \cdot \sum_i N_i \cdot \nu_i \cdot \theta_i^n \cdot e\left(-\frac{\Delta E_{d,i}}{kT}\right) \quad (2.20)$$

K , C and α are constants in the equation and N_i , ν_i and $\Delta E_{d,i}$ are the key parameters that we are interested in as previously mentioned.

As discussed in [37,38], the work of Jong *et al.* [40] discussed different methods for the evaluation of desorption spectra. However, as was identified, there are problems with both 1st and 2nd order processes. For instance, 1st order processes are commonly described by the Redhead peak maximum equation,

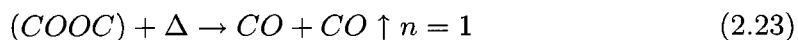
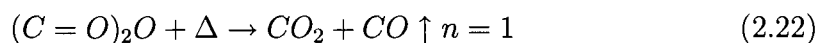
$$\Delta E_d = RT_m \left[\ln \left(\frac{\nu T_m}{\alpha} \right) - 3.46 \right] \quad (2.21)$$

but this equation requires a value for ν to be assumed—commonly values ranging from 10^{12} - 10^{14} Hz are chosen. However, researchers have reported an electron transition [37] component in addition to the vibrational energy transfer which affects the value of ν . The use of Gaussian curves does not accurately describe the kinetics of the desorption processes [37,38]. Conversely, the Polanyi-Wigner equation (Eq. 2.14) can conveniently be used to interpret both 1st and 2nd order processes by changing the value of n (1 for 1st order and 2 for 2nd order).

During the acid treatment, carboxylic acids and hydroxyls are formed (as discussed in section 3.3.1). As the samples are heated, surface reactions take place that allow for the formation of additional functional groups. During this process water is formed as a by-product and can be seen the H₂O spectra. This is known as dehydration and

is illustrated schematically in Figures 2.29 and 2.30. As demonstrated, the results of the dehydration event depend on the starting material. Either a carboxylic anhydride can form as the result of the dehydration between an acid and acid (Fig. 2.29), or a lactone can form as the result of the dehydration between an acid and a hydroxyl (Fig. 2.30). As the nanosheets continue to heat, enough energy is eventually provided for the decomposition—breaking apart—of the anhydrides and lactones as illustrated in Figures 2.31 and 2.32. These results and assignments are discussed in detail in section 3.3.1.

Our data involves both the thermal decomposition of defects and desorption of water created via the thermal decomposition of two functional groups as depicted schematically in Figures 2.31 and 2.32. In order to deconvolute the data, we must assume an order of the reaction and then confirm through our experimental studies. As illustrated in equations 2.22 through 2.24, we assume that the decomposition of functional groups is a 1st order process because the atomic masses that we measure in the mass spectrometer are already formed. The production of water is a 2nd order process because the OH must combine with H during the dehydration. Though [37] and [38] focus on hydrogen desorption and use only a 2nd order Polanyi-Wigner equation to describe the Langmuir-Hinshelwood mechanism, we can easily use the Polanyi-Wigner to describe a 1st order process as well by simply letting $n = 1$.



Previous reports on the thermal desorption of hydrogen from the surface and bulk

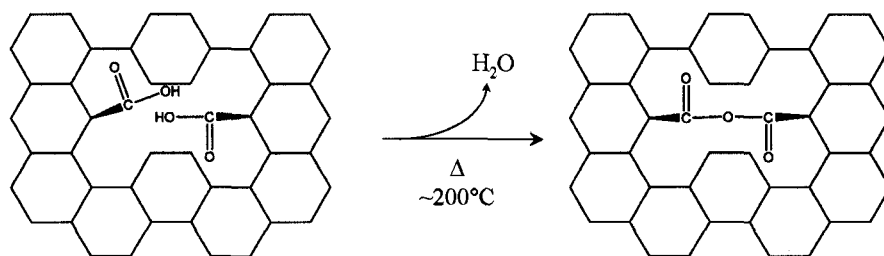


Figure 2.29: Schematic of dehydration event taking place on the surface of the carbon nanosheets between two carboxylic acid groups to form a carboxylic anhydride. H₂O must form from the combination of OH and H and is therefore assumed to be 2nd order.

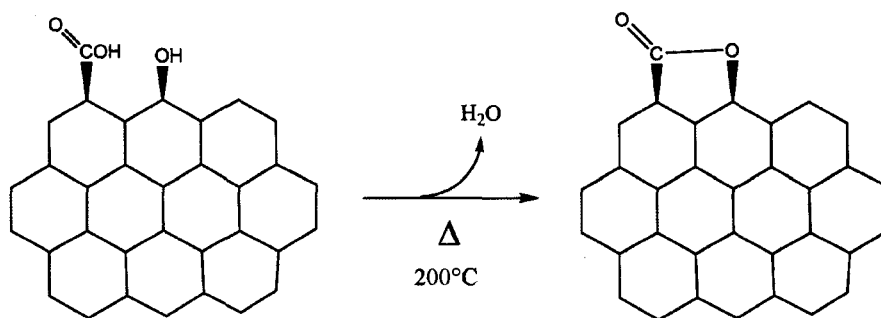


Figure 2.30: Schematic of dehydration event taking place on the surface of the carbon nanosheets between a carboxylic acid and a hydroxyl to form a lactone group. H₂O must form from the combination of OH and H and is therefore assumed to be 2nd order.

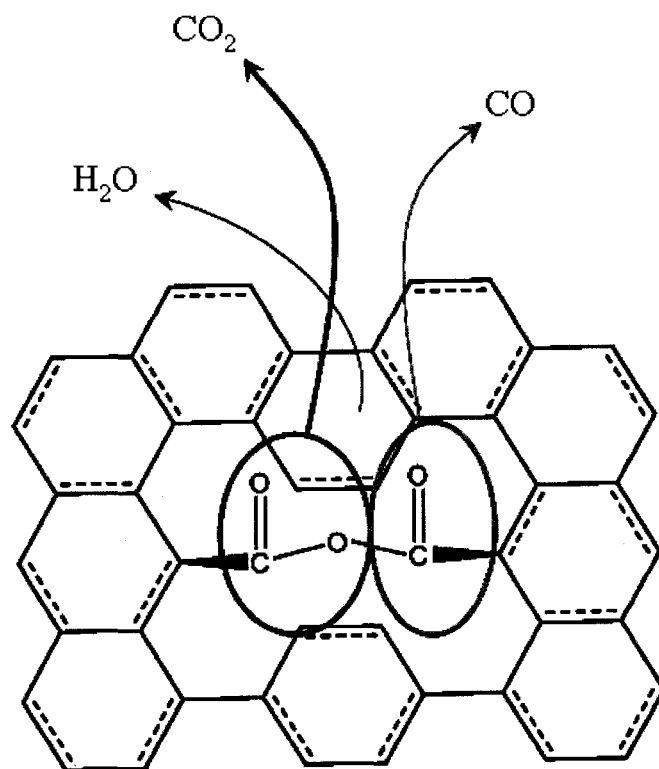


Figure 2.31: Schematic representation of the mechanism involved during the evolution of absorbed species leaving the surface of the functionalized nanosheets. Because the CO and CO₂ are already formed the thermal decomposition of the anhydride group is assumed to be 1st order.

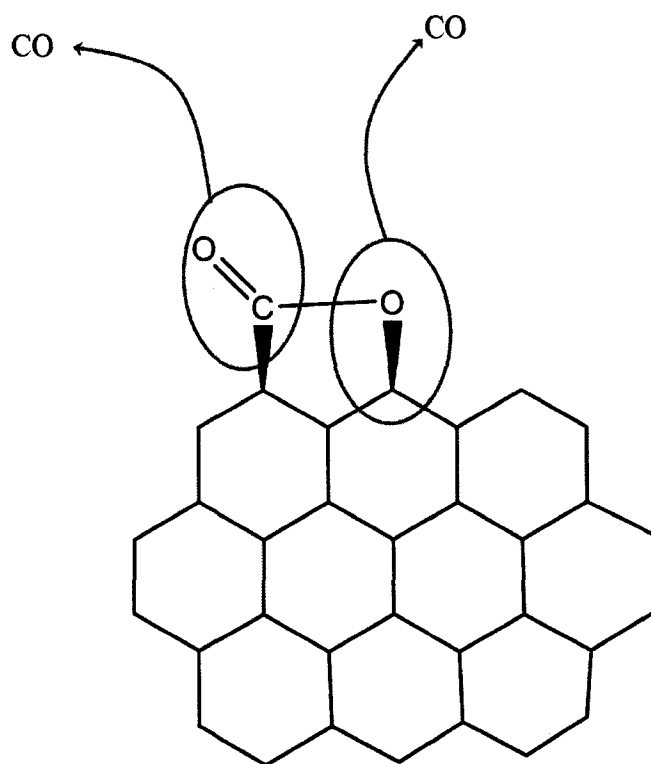


Figure 2.32: Schematic representation of CO leaving the surface of the functionalized nanosheets during the thermal decomposition of a lactone functional group. Because the CO species are already formed the process is assumed to be 1st order.

of carbon nanosheets have identified six different peaks for the bonding of hydrogen in the nanosheet system [37, 38]. The CH_4/H_2 plasma used for the growth of the carbon nanosheets generates hydrogen atoms and ions that are readily incorporated into the nanosheet system, either on the surface or in the bulk or the system. As the temperature of the system is increased, the hydrogen absorbed on the surface at different sites and in the bulk is released and can be quantitatively measured. This same concept forms the foundation of using TDS for identification of oxygen-decorated defects. However, due to the amount of hydrogen that is incorporated in the growth process, there is a concern about blocking information from the functionalization of the nanosheets. Therefore, the samples were vacuum fired after nanosheet deposition and before acid-treatment to remove as much of the hydrogen from the system before functionalizing the samples.

The tantalum foil substrates ($6 \times 6 \times 0.075 \text{mm}^3$) used during the TDS work were sanded (1200 grit) and cleaned with acetone and then isopropanol (with sonication) to remove large inherent structures for the surface and to create a relatively smooth surface for growth. Post-deposition, the samples were inspected *ex-situ* via Raman and SEM to insure quality growth. The samples were then vacuum-fired. After the firing, nanosheet samples were placed in the acid-treatment setup as previously described (Section 2.4).

Rhenium wires (0.125mm diameter) were spot welded to the tantalum substrates so that they could be resistively heated from room-temperature to 1000°C . Individual samples were admitted into the preparation chamber ($p \approx 1 \times 10^{-8} \text{Torr}$) and aligned with the RGA ion source aperture (Feulner-Menzel cup). Afterwards, the samples were placed in the analysis chamber ($p < 1 \times 10^{-10}$) for inspection. The samples were heated at a ramp rate of 10K/sec from room temperature to 1000°C . The data presented is only up to 700°C to separate the sample emission from the heating of the Feulner-Menzel cup.

The sample was positioned on one of the two carousel stations to which power can be supplied and placed on axis with the ion source of an SRS RGA100TM quadrupole mass spectrometer (QMS) for TDS analysis.

2.10 X-ray photoelectron spectroscopy (XPS)

Originally coined ESCA (electron spectroscopy for chemical analysis) by Siegbahn and co-workers [41], XPS is one of the most commonly used surface analysis techniques currently in use today because the exceptional combination of quantitative and qualitative information that is provided by the technique, its ease of operation and its availability for commercial use.

The fundamental principles of the technique are quite straightforward, but the interpretation of the data can become quite convoluted and difficult. The sample's surface is irradiated with soft x-rays, as low as 21.22 eV for HeI sources and high as 1487 eV for Al K_α or 1254 eV for Mg K_α sources. When the photon, with the energy $h\nu$, interacts with an electron in level X of the sample, the entire energy is transferred to the electron which is then ejected with a kinetic energy (E_{kin}) that can be measured, assuming that E_{kin} is greater than the binding energy of the electron (EB) and that there is enough energy to overcome the small work function term, Φ_S . This interaction can be explained by (Eq. 2.25) below and is shown schematically in Figure 2.33.

$$E_{kin}(h\nu, X) = h\nu - E_B - \Phi_S \quad (2.25)$$

The photoelectrons of interest for XPS come from the core levels of atoms and because no two elements share the same set of energies as their binding energies, measurement of these photoelectrons provides elemental analysis. As can also be seen from (2.25), the measured energy (E_{kin}) is strongly dependent on the binding energy of the electron. Therefore, changes in the kinetic energy of the photoelectrons are a reflection of changes in the chemical environment of the atom, leading to chemical analysis of the system.

While XPS is concerned with the primary photoelectron and their kinetic en-

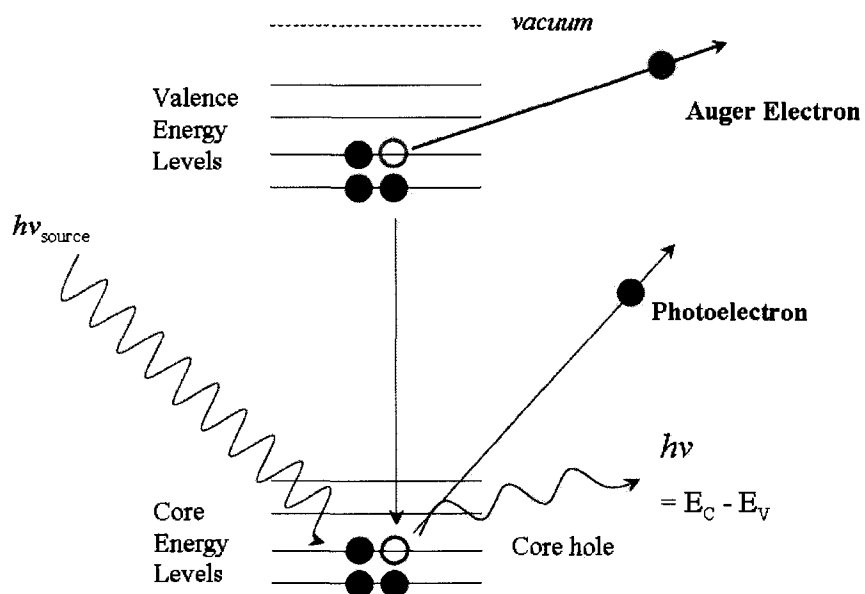


Figure 2.33: Schematic representing the three processes that can occur during an XPS experiment. The initial x-ray photon is represented by the black line and the initial photoelectron and hole created during photoionization are represented by the red dot and circle respectively. The blue dot represents a higher level electron that can fill the hole and release energy as another photon during x-ray fluorescence (blue line) or as another electron (Auger electron, green dot) during the Auger process.

ergies, there are two other processes that can occur during photo-ionization, x-ray fluorescence and the Auger process. During x-ray fluorescence, the core electron is emitted and the hole is filled by the relaxation of a valence electron, releasing radiation equal to the energy difference between the shells. Analysis of this energy can provide information about the energy levels of the sample.

During the Auger process, again, a core-level electron is emitted and a higher energy electron relaxes to fill the hole. However, instead of releasing energy in the form of a photon, another electron, with a binding energy equal to the transition, is released. This is called the Auger electron. The energy of the Auger electron is independent of the source energy, but the kinetic energy of the photoelectrons resulting from direct photoionization increases as the energy of the source is increased. This difference allows for the differentiation of Auger and photoelectrons. Auger Electron Spectroscopy (AES) is often used in conjunction with XPS.

The distance traveled by an electron, through a material matrix (M) with some kinetic energy (E), before making an inelastic collision is called the inelastic mean free path (imfp) $\lambda_M(E)$. This distance depends only on M and E and for the electrons utilized by XPS and AES the value for λ is quite small, which enables use of these techniques for the surface analysis of samples [42]. Previous results from XPS and AES are presented in the following section. A schematic representation of the three processes (direct photo-ionization, the Auger process and X-ray fluorescence) can be found in Figure 2.33. The XPS used during the course of these experiments is located at Stanford University, Palo Alto, California and housed in Stanford's Nanocharacterization Laboratory, courtesy of Professor Michael Kelly. A schematic representation of a typical XPS system is show in Figure 2.34.

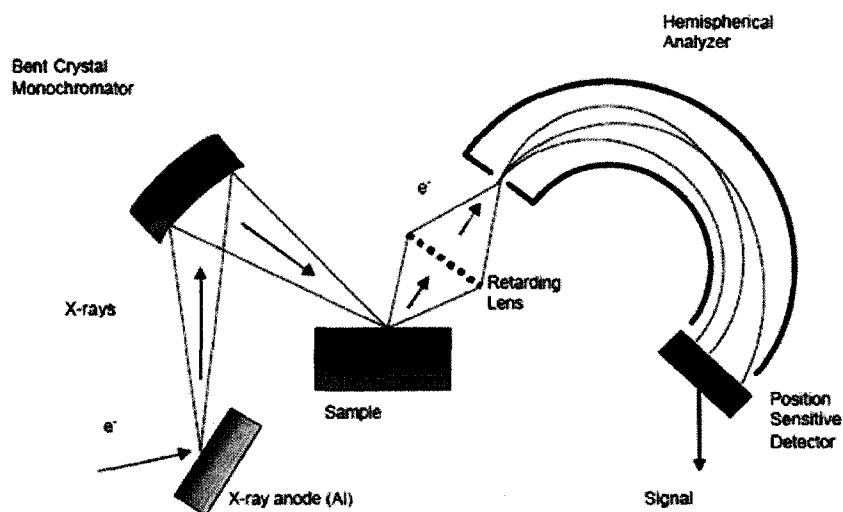


Figure 2.34: Schematic representation of a typical XPS system [43]. The XPS used for these experiments is located in Stanford University's Nanocharacterization Laboratory (SNL). The instrument is an SSI S-Probe Monochromatized XPS Spectrometer, which uses $\text{Al}(K_{\alpha})$ radiation (1486 eV) as a probe. This instrument permits the analysis of areas as small as 100 microns in diameter, and features high sensitivity and good energy resolution. A Leybold Hereaus ion gun for depth profiling and software for automatic spectral identification is also available. The instrument was operated by Dr. Michael Kelly. <http://www.stanford.edu/group/snl/>

2.10.1 Experimental setup for XPS inspection of functionalized carbon nanosheets

XPS was used to determine the surface composition of as-deposited carbon nanosheets and the functionalized carbon nanosheets. Previous characterization of the as-deposited nanosheets [20] showed only a carbon peak and a small oxygen peak associated with absorbed water. As is shown via previous studies of nanotubes, XPS can illustrate the presence of oxygen containing functional groups such as lactones, quinones, hydroxyls and carboxylic acids [44]. The XPS investigation of functionalized nanosheets consisted of three types of samples, as-deposited nanosheets, 3hr acid-treated nanosheets and 3hr water-treated nanosheets.

Samples were loaded into the XPS and pumped down to a base pressure of $\approx 1 \times 10^{-8}$ Torr. Each sample was subject to a room temperature survey scan, varying the detector energy from 0eV to 1400eV. Each sample was then heated to 150°C and held for 10 minutes to remove water absorbed on the surface. Samples were heated to 200°C, 350°C and finally 450°C with the C(1s) and O(1s) high resolution spectra taken at each interval.

2.11 Summary

In this chapter, the techniques and procedures used throughout the course of this research were discussed for reference and the experimental setup as it applies to our research was outlined. As the complexity of the systems under investigation grows combinations of techniques must be utilized to confirm orientations, bonding structures and chemical environments. The next chapter will present the results of the above mentioned experiments and the impact on the functionalization of carbon nanosheets.

Chapter 3

Experimental results and discussion of XANES, TDS and XPS experiments

3.1 Introduction

In the previous chapter, the fundamental principles of different materials characterization tools were presented. The setup and experimental design used to study the effects of acid-treatment towards the functionalization of carbon nanosheets was also outlined. Raman spectroscopy demonstrated an increase in the disorder of the graphene system via an increase in the D and G' peaks and a decrease in the G peak after acid treatment. Fourier transform infrared spectroscopy supports the presence of oxygen in the chemically modified nanosheets. These results suggest that the acid treatment is controllably introducing oxygen decorated defects into the graphene lattice of the carbon nanosheets, however, they are not definitive enough to make this assignment based on this data alone. In this chapter, the results of the XANES, TDS and high resolution XPS experiments are presented and discussed in detail. The XANES results illustrate oxygen created defects in the nanosheet system. Deconvolution of the TDS spectra identifies the defects as carboxylic acid and hydroxyl groups. Finally, inspection via high resolution XPS and sub-peak identification supports these assignments. The impact of these identifications and assignment are discussed along with

future experiments that could continue the characterization of the functionalization experiments.

3.2 X-ray absorption near-edge spectroscopy

As was discussed in the section 2.7, x-ray absorption near-edge spectroscopy is a technique that involves the irradiation of a sample with soft x-rays, followed by the excitation of core electrons to unoccupied molecular orbitals. This absorption is measured through the ejected electrons and a spectrum is produced. When a material has a different local environment, a shift of the available transitions will be noticeable. For this purpose, XANES was chosen to identify the creation of defects by an acid treatment in the carbon nanosheet system.

3.2.1 Results and interpretation of data from x-ray absorption near-edge spectroscopy (XANES)

As-deposited carbon nanosheet samples compare well with highly oriented pyrolytic graphite (HOPG) as shown in Figure 3.1. However, the acid- and water-treatment of samples produces peaks not seen in the HOPG or as-deposited spectra, Figure 3.2.

The experiments reveal three distinct features that are of interest. The first at ≈ 284.5 eV is a result of the C=C 1s - π^* transition [45, 46]. The last feature is composed of two peaks which are attributed to the C-C 1s - σ^* transition [45, 46]. The second feature is also composed of two peaks and has been contributed to inter-layer interactions in the graphitic system [47], σ^* C-H resonances or more recently to oxygen containing groups, π^* C-O resonances [45, 46, 48, 49]. For ease of reference, we designate these features as A, C and B respectively. The middle features, B1 and B2 (Fig. 3.3), are the focus of our study as we correlate these peaks to oxygen-containing functional groups as well.

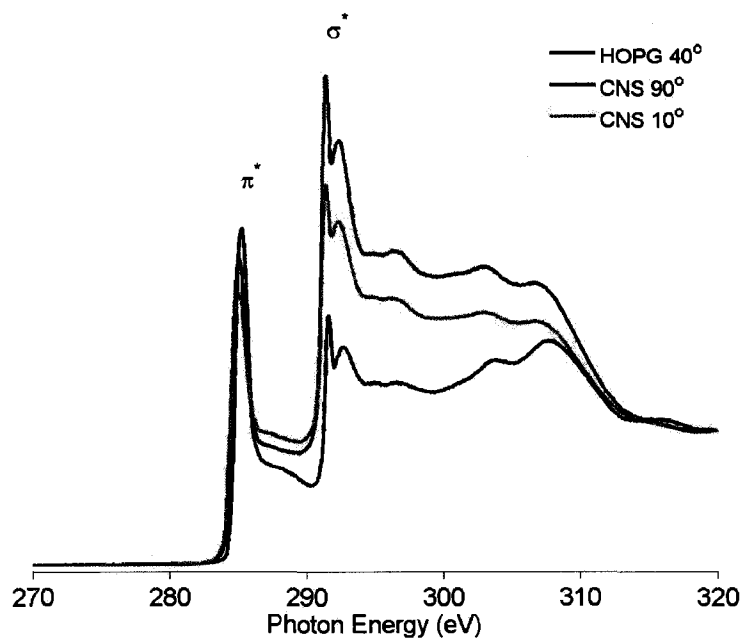


Figure 3.1: XANES spectra comparing HOPG (spectrum provided by Dr. Alexei Preobrajenski, MAX-Lab) and as-deposited nanosheets. Note the alignment of the π^* and σ^* peaks at 285eV and 291eV respectively. The spectra have been pre- and post-edge normalized and a linear baseline subtracted for ease of viewing and comparison. The y axis is a normalized intensity and has been removed to avoid confusion.

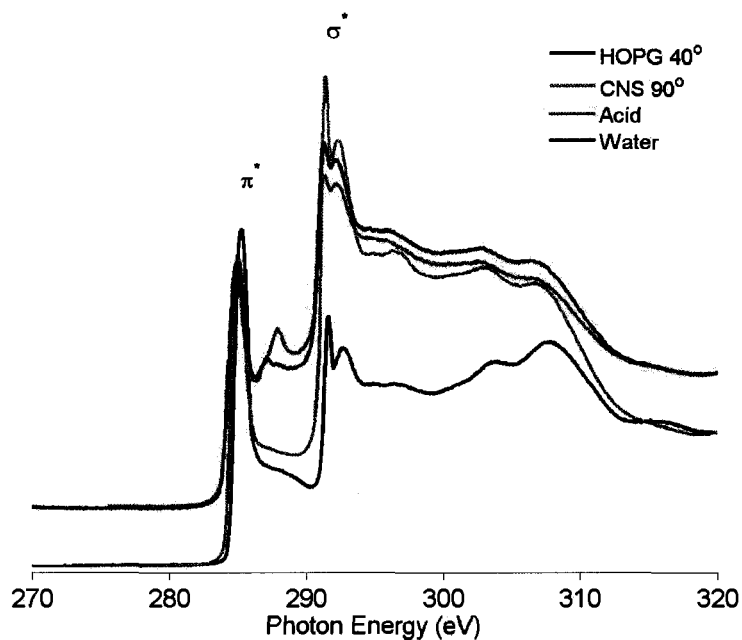


Figure 3.2: XANES spectra of as-deposited, acid-treated and water-treated nanosheets. Notice the creation of the two peaks between the π^* and σ^* peaks.

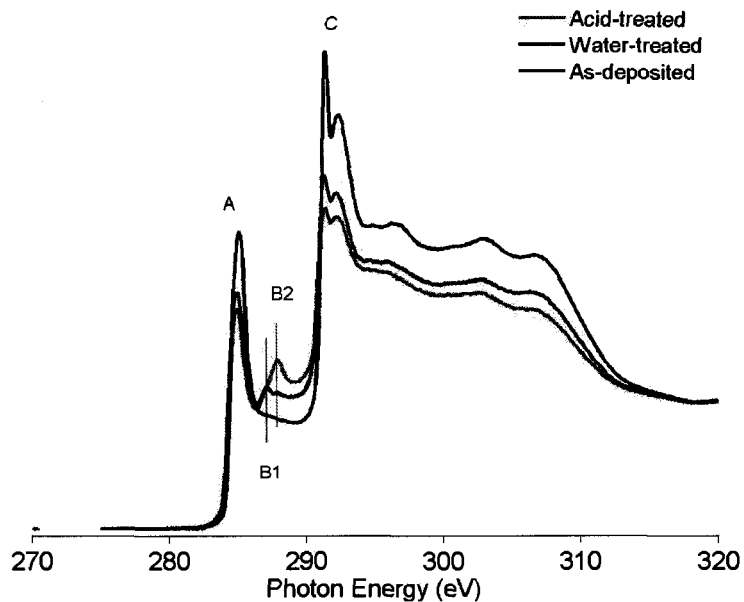


Figure 3.3: XANES spectra of the acid-treated, water-treated and as-deposited nanosheets with the π^* and σ^* peaks labeled as A and C respectively and the defect peaks labeled as B1 and B2. All spectra were collected at 90° from grazing.

For the nanosheet system, it is clear that the π^* and σ^* peaks do not show the angular dependence expected for a free-standing graphene system or for a horizontal graphene system. In a system composed of only vertical graphene sheets, the π^* resonance (A) would have a maximum intensity at normal incidence (to the substrate) and a minimum at grazing incidence. While the σ^* resonance would have a maximum at grazing incidence (to the substrate) and a minimum at normal. In an only horizontal system, the exact opposite would be true. However, as shown in Figure 3.1, we see a strong π^* and σ^* resonant intensities at grazing and normal angles. This is due to the contribution of both horizontal and vertical graphene planes (as illustrated in Figure 2.3 (c)).

As is shown in Figure 3.4, both the acid-treated and water-treated samples exhibit the B1 and B2 peaks, though the B2 peak is much more pronounced in the acid-treated samples. The B1 peak appears to remain constant. This suggests that the B2 peak is a result of defects more strongly introduced to the graphene system during the acid treatment. We have assigned the B2 resonance to σ^* resonances of C-O bonds, formed by bond cleavage in the C-C network during the acid treatment. Our identification is supported by the improved wetting of the nanosheet samples, the relative decrease in the intensity of the A and C peaks to the B features, corresponding to a relative decrease in the C-C π^* and σ^* transitions. Initial XPS characterization indicates that the acid-treated samples have a 30% higher O:C ratio compared with the water-treated samples and a 100% higher O:C ratio compared to the as-deposited sample, which contained up to 2-3% O (with no heating). Also, the absence of Cl in the XPS spectra rules out C-Cl bonds as the origin of the B2 peak.

As seen in Figure 3.5, the B2 resonance is most pronounced at grazing incidence. We assume that the free-standing graphene sheets of the nanosheet system are more susceptible to electrophilic attack by the hydronium ion [50] due to pyramidalization and π misalignment that is present at the edges and curvatures of the sheet walls

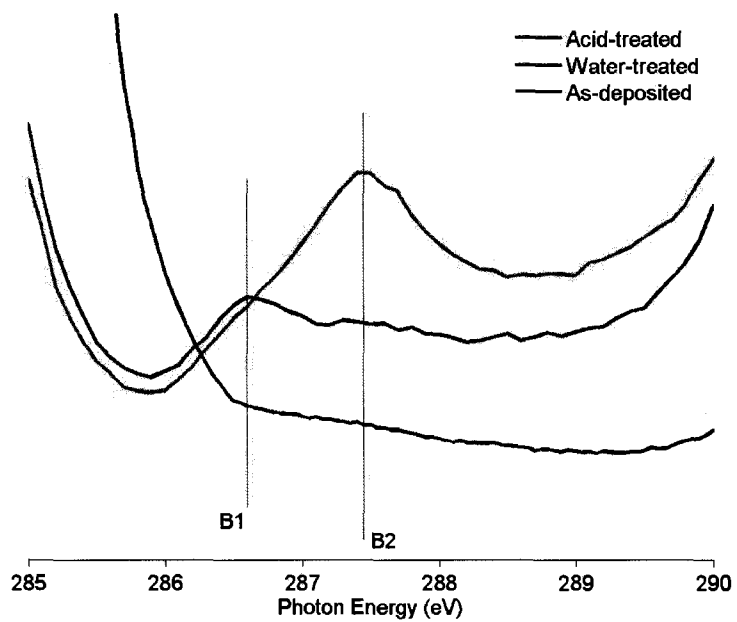


Figure 3.4: Close up of the B1 and B2 features observed in the XANES spectra. As can be seen, both B1 and B2 peaks are absent from the as-deposited sample (black), but present in both the acid- (green) and water-treated (blue) samples with different intensities.

[51, 52]. Therefore, most defects will be created on the surface layers of the vertical sheets, leaving the basal layers mostly unaffected. However, while the strong angular dependence that we see supports this assertion, a more rigorous investigation would need to be undertaken to prove it. The angular dependence demonstrated could be the result of a surface area phenomenon, but this was not considered to be of critical importance. Our results suggest that the B2 resonance possesses σ^* character, i.e. involving bonds within the plane of the sheets. In Figure 3.6 the angular dependence exhibited by the water-treated nanosheet sample is shown. These results suggest that the B1 resonance of the water-treated samples exhibits σ^* character as well. However, the strong dependence shown by the B2 feature is not present. The lack of the B1 feature in the as-deposited nanosheet samples tends to rule out assignment of the B1 peak to σ^* C-H bonds. As shown previously, as-deposited nanosheets possess C-H bonding on the surface [37] and we would expect to see the B1 feature in the as-deposited samples if this feature arose from the C-H bonds. Therefore, while tentative, we have assigned the B1 feature to π^* resonances of C=O. These assignments agree with our preliminary calculations [14] and with assumption that the sidewalls of the nanosheets provide a more reactive surface based on pyramidalization and the possibility of π misalignment that is observed with nanotubes.

We can see a difference in the B1 and B2 peaks based on time and temperature of acid-treatment, with B2 being more pronounced with acid-treatment, than with water-treatment, and increasing with longer treatments. However, a direct comparison can not be made by plotting the spectra at this time. The angular dependence measurements were made without monitoring the initial beam and therefore its contribution can not be subtracted out of the spectra. As the sample is heated, the intensity of the B1 and B2 peaks decrease as shown in Figure 3.7 and Figure 3.8. The ratio of B1/B2 is dependent upon the type of functionalization treatment (water vs. acid) that the sample received, (Fig. 3.4). After heating to a very high temperature

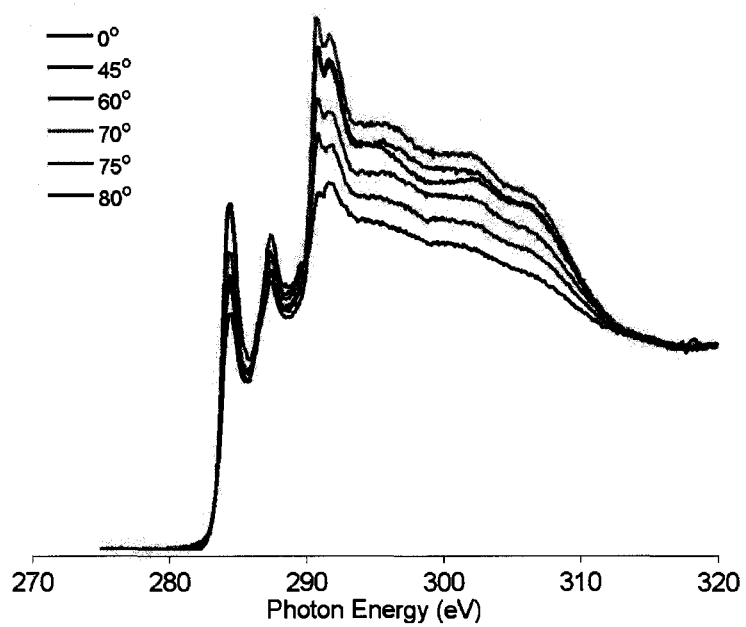


Figure 3.5: XANES spectra of acid-treated nanosheets. As the angle of incidence from normal increases (towards grazing) the B2 feature becomes more pronounced with respect to the other features. This indicates the σ nature of bonds that are the cause of the B2 resonance.

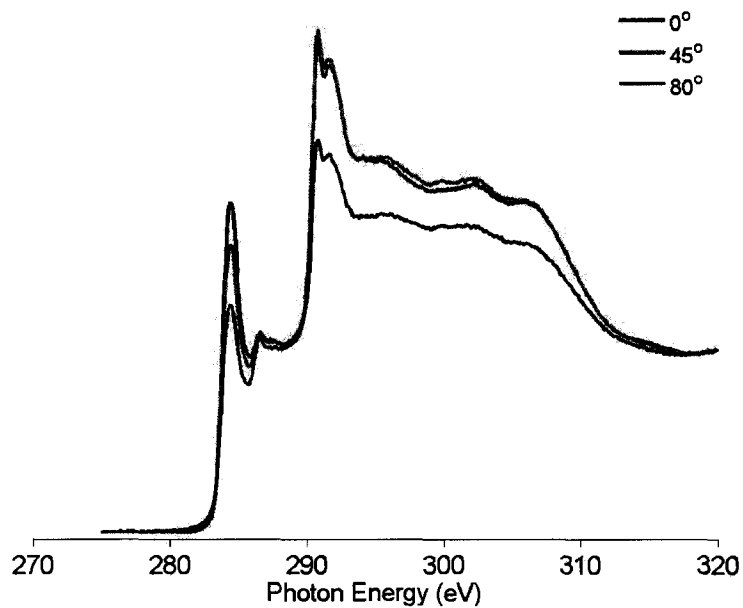


Figure 3.6: XANES spectra of water-treated nanosheets. As the angle of incidence from normal increases the B1 feature becomes more pronounced with respect to the other features. This should indicate a σ nature of the bonds that are the root of the B2 resonance. However, no B1 feature is observed in the as-deposited samples, indicating that the feature is not a C-H σ^* resonance and because the resonance is not as strong as the dependence of the B2 peak, the feature is tentatively assigned to C=O π^* resonance, in agreement with previous nanotube work.

($\gg 320^\circ\text{C}$), the spectra compare well to that of HOPG, Figure 3.9.

Preliminary calculations and modeling, using density functional theory, of a di-vacancy introduced in the graphene plane has successfully reproduced the spectroscopic features (in simplified form) that we see in the XANES results. In Figure 3.10 (left) a schematic of a di-vacancy defect is provided. The blue dots represent the carbon atoms and the yellow represents the charge density of the electron states near the defect. As can be seen from the density of states calculations (Fig. 3.10 right), the carbon atoms near the defect site have an increase in states available near the Fermi level, while the atoms away from the defect do not experience this shift and present the density of states expected for a pure graphene layer. The presence of these calculated mid-gap states not only supports the XANES spectroscopic features, but also suggests that the defects created in the nanosheet system can increase the conductivity of the system.

In order to further investigate these theories, acid-treated and as-deposited nanosheets were electrically contacted with a tungsten nano-manipulator inside a focused ion beam/scanning electron microscope (FIB/SEM). The tip was polished in-situ to 10 - 20nm by using the Ga^+ beam, which led to a reduction of oxygen on the tip and better definition of the tip/nanosheet contact area. Strong contact between the tip and the individual nanosheets was observed through a slight bending of the nanosheet. When contact was not sufficiently strong, tip vibrations and drift led to a delamination of the tip and was observed as a current drop in the measurements. A current - voltage (I/V) measurement of the sheet was performed by flowing current from the tip to the grounded substrate. The voltage was scanned from -1 to 1V in 30-40 seconds. Three to five measurements were taken at the same location. Because of the density of nanosheets, it was possible to obtain multiple measurements (≈ 400) per sample. Representative results are shown in Figure 3.11. As shown, the conductivity of the functionalized nanosheets has increased by an order of magnitude over that of the

as-deposited nanosheets. These experimental results have shown that we were able to tune the properties of the carbon nanosheets through the introduction of defects. The introduction of the mid-gap states seen in Figure 3.11 produces a regime of metallic character in the nanosheets, allowing for the increase in conductivity.

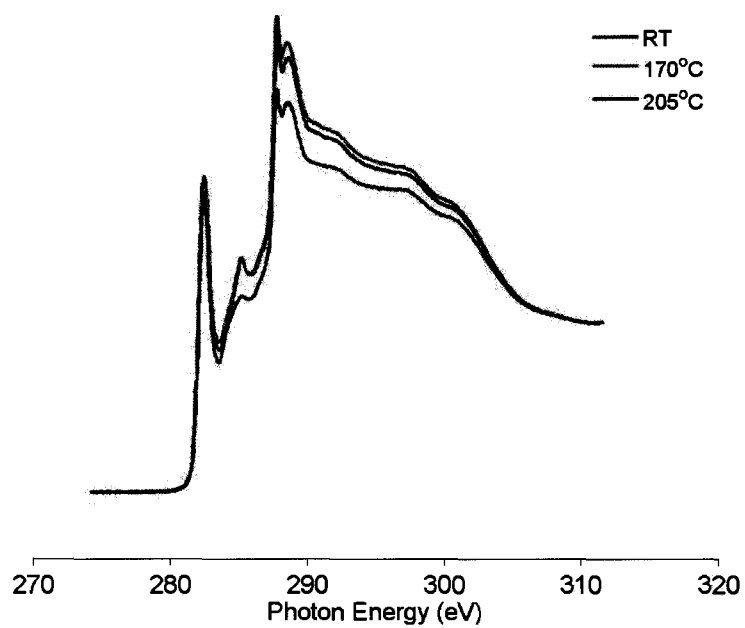


Figure 3.7: XANES spectra of 3 hour acid-treated nanosheets that are being heated stepwise. Notice the decrease in the B2 feature and the start of the deconvolution of the shoulder (the B1 peak).

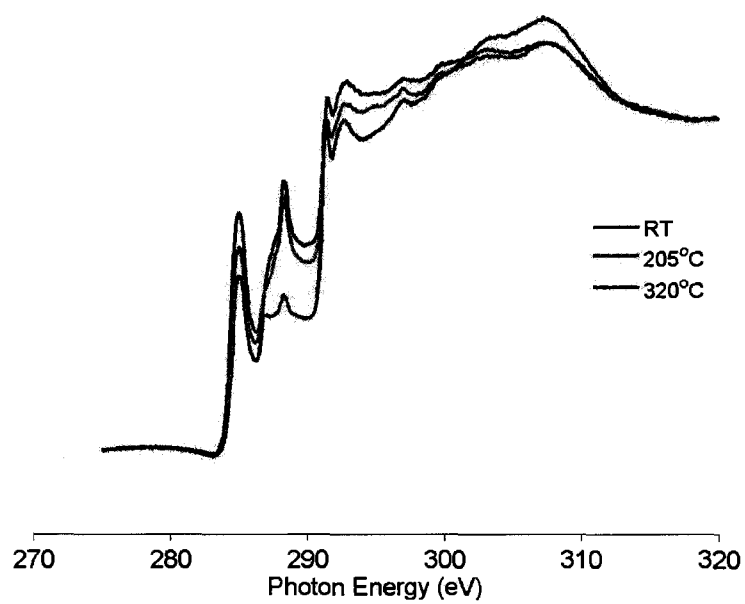


Figure 3.8: XANES spectra of 23 hour acid-treated nanosheet samples that are being heated stepwise. These spectra were taken in the front chamber of the beamline and therefore the initial beam can not be subtracted out. However, the clear evolution of the B1 and B2 peaks can be seen after heating the sample above $\gg 320^{\circ}\text{C}$.

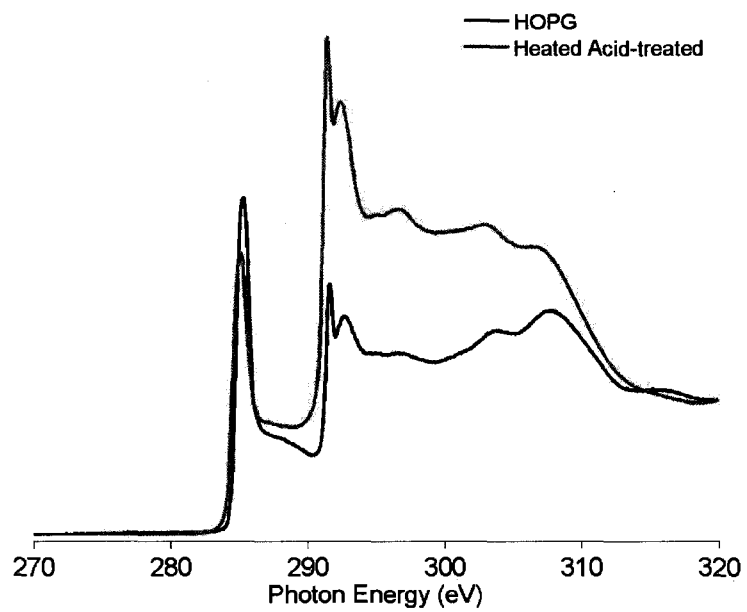


Figure 3.9: XANES spectra taken of acid-treated carbon nanosheets after heating samples to very high temperature $\gg 320^{\circ}\text{C}$ showing the disappearance of the B1 and B2 defect features.

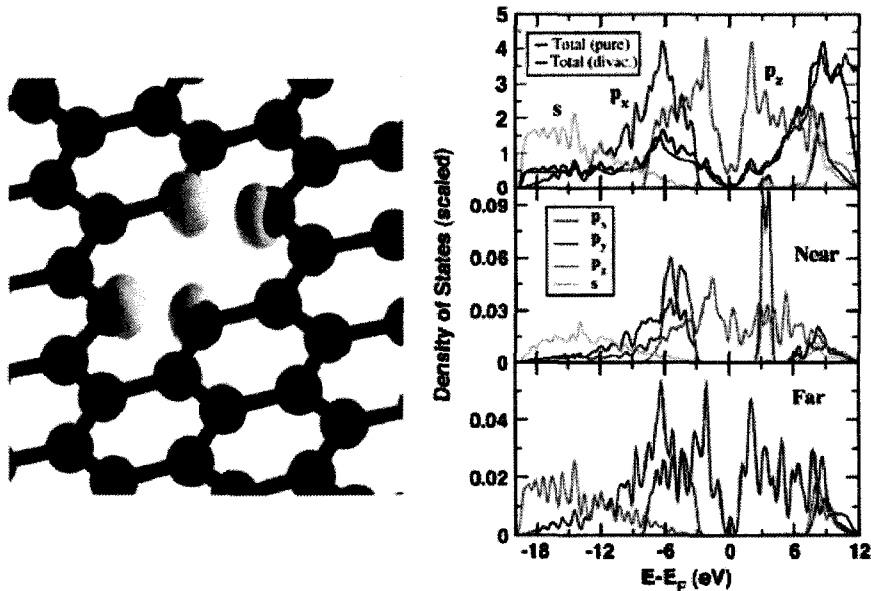


Figure 3.10: A schematic of the di-vacancy defect created in a graphene layer (left). The blue represents the carbon atoms that make up the graphene layer and the yellow is representative of the charge density of the electron states near the defect site. The density of states (DOS) as calculated for a pure graphene layer and a graphene bilayer with a di-vacancy (right top). The DOS for atoms near the defect (right middle) and far away from the defect (right bottom) [14].

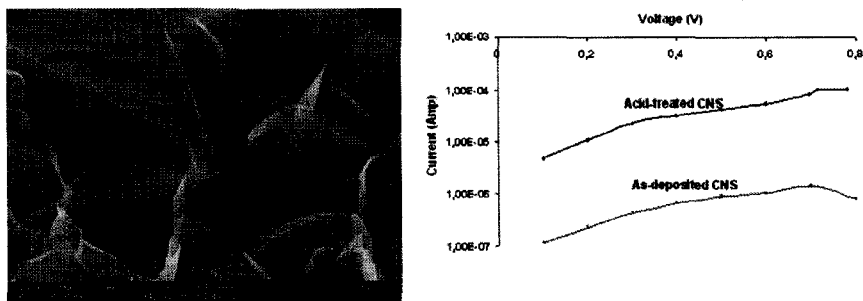


Figure 3.11: SEM image (left) of modified AFM/SEM tip making contact with a single carbon nanosheet. By sweeping the voltage and measuring the current of the nanosheet systems (functionalized and as-deposited), the increased conductivity of an order of magnitude is shown (right).

3.2.2 Summary of XANES experiments

Defect creation in the carbon nanosheet system via acid treatment was confirmed via XANES and supported with density functional theory calculations. The B1 feature that has previously been assigned to both C-H σ^* and C=O π^* transitions was tentatively assigned to C=O π^* transitions because no such feature was observed in the as-deposited samples. The B2 feature was assigned to C-O σ^* transitions in agreement with previous literature. Calculation of the local density of states predicts the features observed in the experimental data, offering further support of defects created by the acid and water treatments.

These calculations suggest that the defects introduced via the functionalization of the nanosheets could enhance the conductivity of the carbon nanosheets by the introduction of new levels close to the Fermi level of the system. In support of this hypothesis, experimental evidence showing the increased conductivity of the carbon nanosheet system was shown. These results lend credence to the calculations and our assumptions. Based upon the results from the XANES and density functional theory calculations we have developed a novel way to introduce functionality and new properties to a graphene layer [14]. However, identification of the exact chemical nature of the functional groups is needed to further nanosheet technology. This classification will allow for the tailoring of electronic and chemical properties of the nanosheet material through further chemical reactions. Thermal desorption spectroscopy was employed for the identification and the results will be discussed in the next section.

3.3 Thermal desorption spectroscopy

Thermal desorption spectroscopy (TDS) is a technique that involves the heating of a substrate in a vacuum environment and by measuring the pressure of different gases that desorb from the surface. For the following work, TDS was employed in an effort to classify the exact chemical functionality of the defects identified with XANES. By using TDS, we are able to not only categorize the composition of the defects, but also the stability of the defects.

3.3.1 Identification of the TDS features

As mentioned previously in section 2.3, Raman spectroscopy of the nanosheet samples was utilized to investigate the effects of the functionalization on the nanosheet system. As was shown in Figure 2.7—and again in Figure 3.12 for convenience—the D peak and $G'(2D)$ increases while the G peak intensity decreases as expected during the creation of defects that shorten the order of the graphene system. Though we can identify the creation of defects via Raman, we can not quantify the functional groups with Raman alone. The functional groups can also be created on the edges of the nanosheets. Because these edges already contribute to the disorder of the graphene system, their contribution does not increase when they are functionalized and a method such as TDS is required.

A TDS spectrum of a typical Ta substrate is shown in Figure 3.13. Notice the large CO_2 peak around 250°C that dominates the spectrum. This peak was not expected and has caused a complication in the deconvolution of the TDS data. Due to the substrate's contribution to both the CO_2 and CO spectra, peaks before 280°C will be left out of our analysis.

A comparison of the CO spectra for as-deposited, water- and acid-treated carbon nanosheets is shown in Figure 3.14. The literature indicates that the presence of a

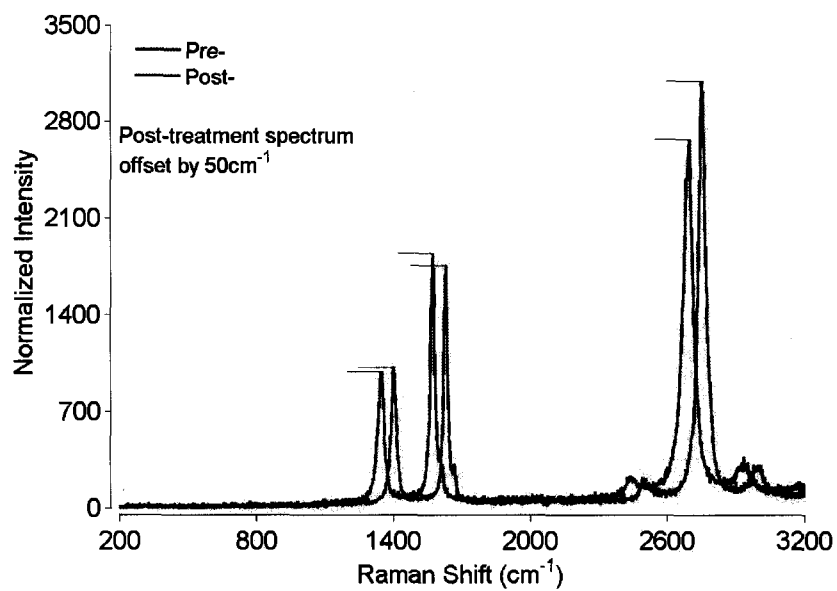


Figure 3.12: Representative Raman spectra of pre- and post-functionalization carbon nanosheets. The blue line represents the nanosheets after being vacuum fired, but before the functionalization treatment. The red line represents the same sample after undergoing functionalization through a three hour acid treatment. The data of the functionalized nanosheets (red) has been offset by 50 cm^{-1} to aid in viewing.

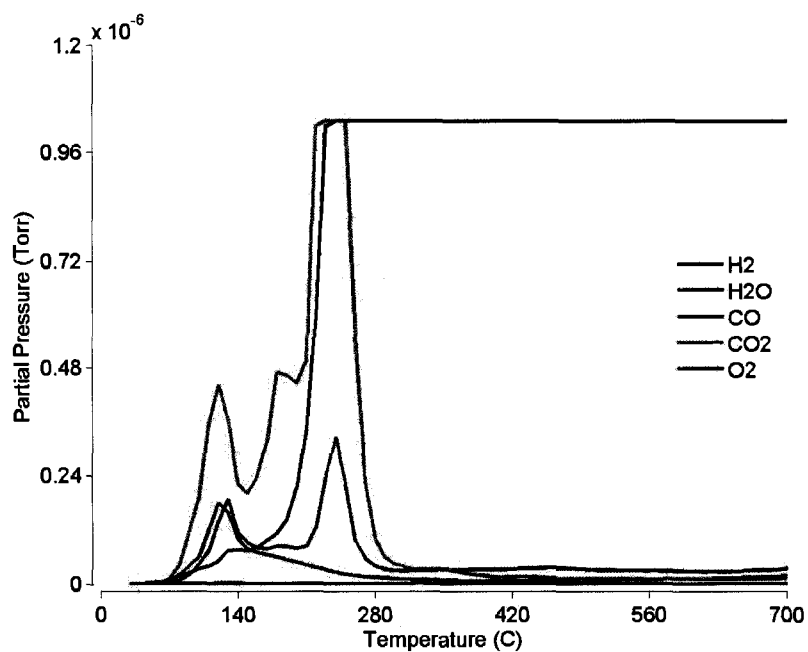


Figure 3.13: TDS spectrum of a tantalum substrate. Notice the dominating CO₂ peak (green) and large contribution to CO (blue). Because of these contributions, the features in the acid- and water-treated nanosheets appearing before 280°C will be left out of the analysis.

CO peak around 400°C is the result of the decomposition of anhydrides and that peaks around 570°C are the result of hydroxyl groups [44, 53–55]. Both are present in the spectrum of the acid-treated sample. However, only the anhydride peak at $\approx 400^\circ\text{C}$ is present in the as-deposited samples. The water-treated sample is more complicated with a peak falling in between the values for anhydrides and hydroxyls. This peak can be assigned to a high binding anhydride or to a low binding hydroxyl.

Figure 3.15 contains the CO–2 spectra of the as-deposited, water- and acid-treated samples. The acid-treated spectrum produces three areas of interest. The first feature of interest is around 280°C - 290°C. It is possible that this peak results from the decomposition of carboxylic acids though due to the large contribution from the substrate the identification of this peak is not possible at this time. The second peak of interest is the peak located at 400°C, representative again of the decomposition of an anhydride group. The final peak of interest is the peak located at $\approx 530^\circ\text{C}$. Due to the presence of a hydroxyl peak in the CO spectrum, it is possible that this CO₂ peak results from desorption of lactone groups, formed during a dehydration process of a carboxylic acid and a hydroxyl. The literature does not identify a specific peak for lactones, but instead offers that the desorption of lactones will be seen in the CO₂ spectra after anhydrides (400°C), but before pyrone type groups [53, 55].

The water-treated spectrum offers two peaks of interest; both centered around 400°C. The presence of two peaks so close to 400°C indicates the presence of high and low binding anhydride groups. The assignment of these peaks to anhydrides supports the assignment of the previously observed CO peak to a high binding energy anhydride instead of hydroxyl groups and is further supported by the lack of a lactone type peak in the CO₂ spectra that is seen with the acid-treated sample.

The presence of a CO₂ peak at 400°C in the as-deposited spectrum is again representative of anhydride groups. Both the CO and CO₂ feature in the as-deposited spectra is unexpected. The nanosheet system does not contain oxygen as shown by

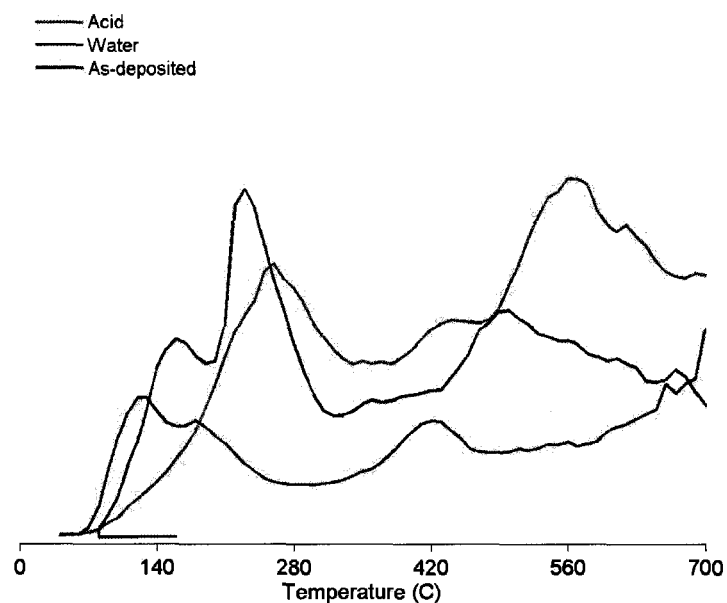


Figure 3.14: Comparison of the CO spectra for as-deposited, water- and acid-treated carbon nanosheet samples. The peaks at 400°C are representative of anhydrides and the peak in the acid-treated spectra at 570°C is deemed the result of hydroxyl groups. The peaks before 280°C are not considered in the discussion due to substrate contribution (not shown here).

previous characterization experiments (i.e. Auger and XPS) [20]. Their presence suggests surface reactions taking place on the surface of the nanosheets during the heating of the substrates. Boehm [55] suggests a possible aging mechanism that may cause the incorporation of water into the nanosheet matrix. This process in combination with surface reactions could explain the observed anhydride peaks after heating in the as-deposited sample.

Inspection of the H₂O spectra from the as-deposited, water- and acid-treated samples offers insight to the presence of anhydride and lactone type functional groups. As can be seen in Figure 3.16, the H₂O spectrum of the as-deposited carbon nanosheets possesses a single peak with its maximum at 120°C. This peak is used as the reference for all other data and is assigned to desorbing atmospheric water. However, this peak does tail, supporting the identification of surface reactions taking place on the as-deposited nanosheets, which explain the presence of the anhydride peak at 400°C in the CO₂ and CO spectra. The water- and acid-treated samples both possess a second water peak that has an even higher intensity than that of the peak at 120°C. The second peak in the water-treated spectrum is located at 160°C while the second peak in the acid-treated sample is located at 210°C. The presence of these peaks support the assertion that there is a dehydration event taking place, resulting in the creation of anhydride-type defects in both the water- and acid-treated samples (schematic shown in Figure 3.17) and possibly in lactone type defects (acid only). This proposed reaction is supported by the presence of the CO and CO₂ peaks at 400°C in both water- and acid-treated samples, as well as the hydroxyl peak at 570°C (CO spectrum) and lactone peak at 530°C (CO₂ spectrum) in the acid-treated spectra. For ease of reference, schematics of the functional groups mentioned in this section are provided in Figure 3.18.

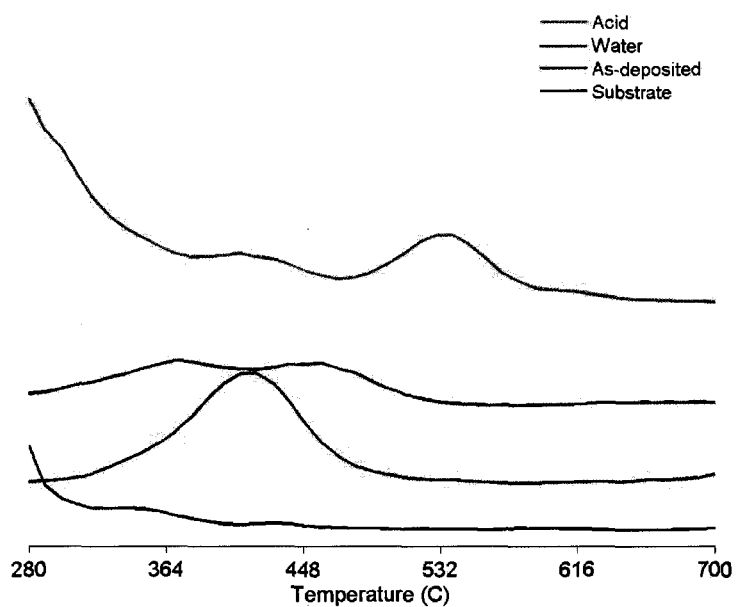


Figure 3.15: Comparison of the CO₂ spectra for as-deposited, water- and acid-treated carbon nanosheet samples. The acid-treated spectrum (green) produces three areas of interest. The first around 280°C, the second at approximately 400°C and the third at 530°C. The water-treated spectrum (blue) has two peaks associated with the anhydride location around 400°C and the as-deposited spectrum (red) has only the peak at 400°C. The substrate spectrum (black) shows no structure after 280°C.

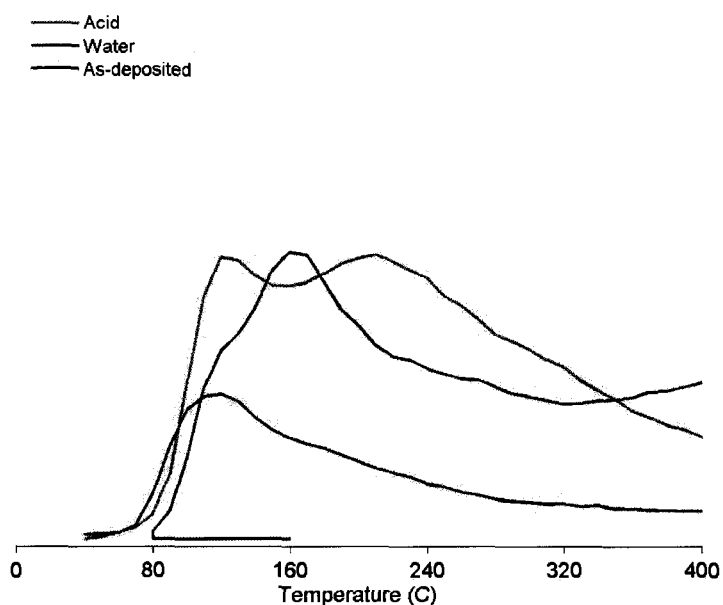


Figure 3.16: Comparison of the H₂O spectra for the as-deposited (red), water- (blue) and acid-treated (green) carbon nanosheet samples. The second peak in the water-treated spectrum is centered at 160°C and the second peak of the acid-treated sample is centered at 210°C. The presence of these peaks suggest a dehydration event between carboxylic groups, possibly a carboxylic and hydroxyl (acid only), resulting in the presence of anhydride and lactone groups respectively. The increase of the peak intensity at 120°C supports the hypothesis of the decreased hydrophobic behavior of the functionalized carbon nanosheets.

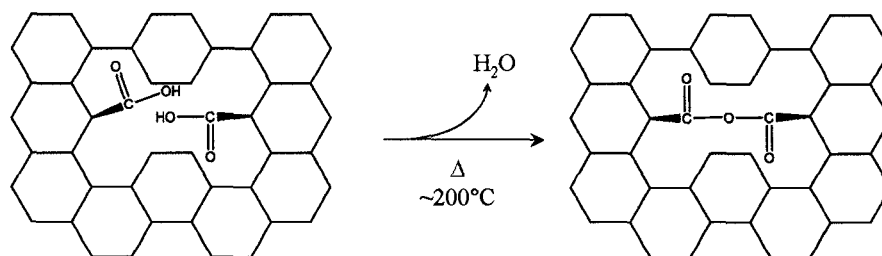


Figure 3.17: Schematic of dehydration event taking place on the surface of the carbon nanosheets between two carboxylic acid groups to form a carboxylic anhydride.

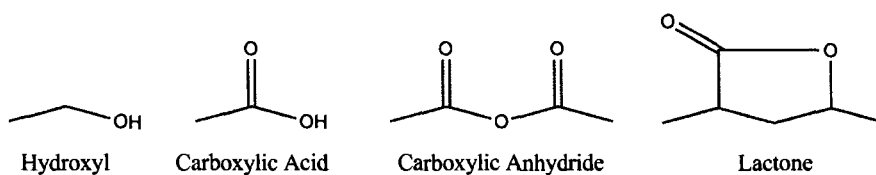


Figure 3.18: Schematic of possible functional groups created by the acid treatment as well as by subsequent surface reactions induced by thermal treatment of the nanosheet samples. The junctions in the schematic represent carbon atoms unless otherwise labeled.

3.3.2 Deconvolution of the TDS spectra

As was mentioned in section 2.9.1, deconvolution of our TDS spectra is complicated by the combination of both 1st and 2nd order processes. The thermally activated decomposition of anhydride, lactone and hydroxyl defects are assumed to be 1st order processes, but desorption of the water molecules produced during the dehydration is a 2nd order process. Section 2.9.1 mentioned that we can use 1st and 2nd order Polanyi-Wigner equations to help deconvolute and analyze the spectra.

Utilizing code generated previously [37], small modifications were made to adjust to the different spectra. Inspection of the acid-treated CO₂ spectrum via this mechanism can be used to identify ΔE_d , the desorption energy of the molecules, N_i , the number of desorbing molecules and ν , the pre-exponential factor associated with the vibrational frequency of the molecule. However, using a first order equation did not produce a satisfactory fit, as shown in Figure 3.19. A second order equation was then used to fit data producing a much better fit as shown in Figure 3.20. This fit suggests that desorption of CO₂ from the functionalized carbon nanosheets is indeed a second order process. In order to determine the validity of this assumption, however, a more rigorous study would need to be completed. One should be able to plot the rate of desorption vs. one over the temperature in Arrhenius form to determine the order of the process. For this fitting routine, the number of peaks to be used in the deconvolution must be entered before beginning. For our purposes, we began with a small number and increased the number until we received a satisfactory fit. For example, for the CO₂ acid-treated spectrum, we started with four peaks and increased to six. The sixth peak is not visible because it fits the tail of the data. This was observed with all of the fits. We stopped with the lowest satisfactory number. More experiments are suggested, involving not only inspection of the application of the Polanyi-Wigner equations in the MATLABTM program, but also of the TDS work itself, utilizing another substrate such as gold that does not contribute to the CO and

CO₂ spectra.

The results of the second order fit are shown in Table 3.1. The values for N_i allow for the calculation of the total number of desorbing molecules for the sample. From this a percentage of molecules per defect feature allows for the calculation of defect specific density calculations by relating the total number of molecules (N_{total}) to the pressure (p) by (3.1)

$$N_{total} = \frac{2S}{kT_{room}} \cdot \int_0^{\infty} p \cdot dt \quad (3.1)$$

However, with the current setup, such a calculation requires a specific knowledge of the pumping speeds for each of the relevant chemical species desorbed. This is experimentally difficult. However, one can assume that the variation follows equation 3.2, where S_i is known. Experimental results with no contribution from the substrate would be required for an accurate assessment of e.g., carboxylic type defects vs. hydroxyl type defects. The results of fitting the CO spectrum (Fig. 3.21 and Table 3.2) as well as the H₂O spectrum (Fig. 3.22 and Table 3.3) are provide for comparison.

$$\frac{S_2}{S_1} \propto \sqrt{\frac{m_2}{m_1}} \quad (3.2)$$

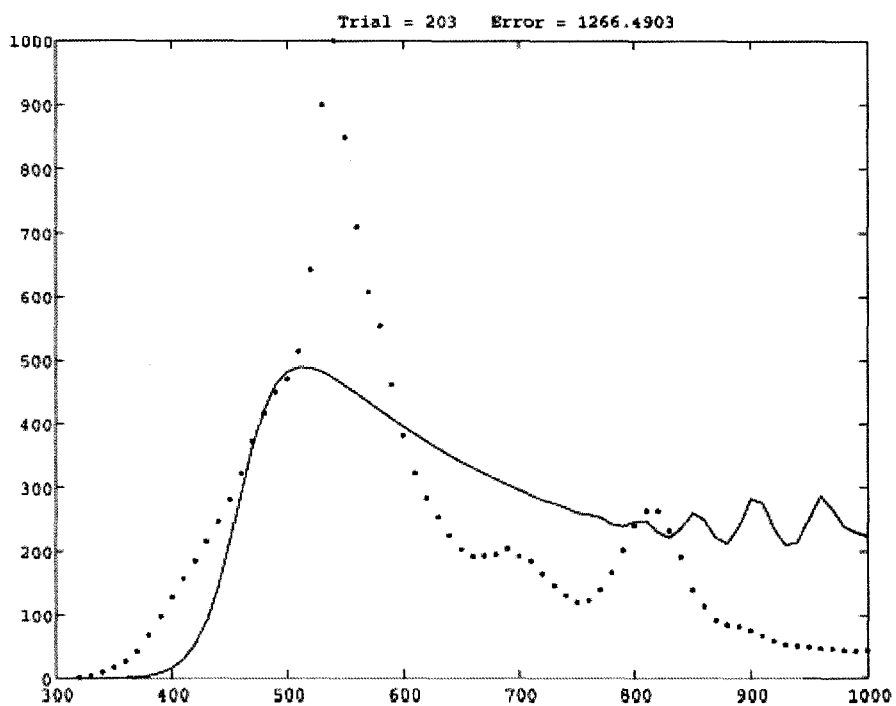


Figure 3.19: Deconvolution of the CO₂ acid-treated spectrum using a first order Polanyi-Wigner equation, producing an unsatisfactory fit. The program did not run for more than 300 iterations before kicking out with the above fit, suggesting that was the best fit possible with the current parameters. The x-axis is temperature and the y-axis is in arbitrary units as described previously in section 2.9.1.

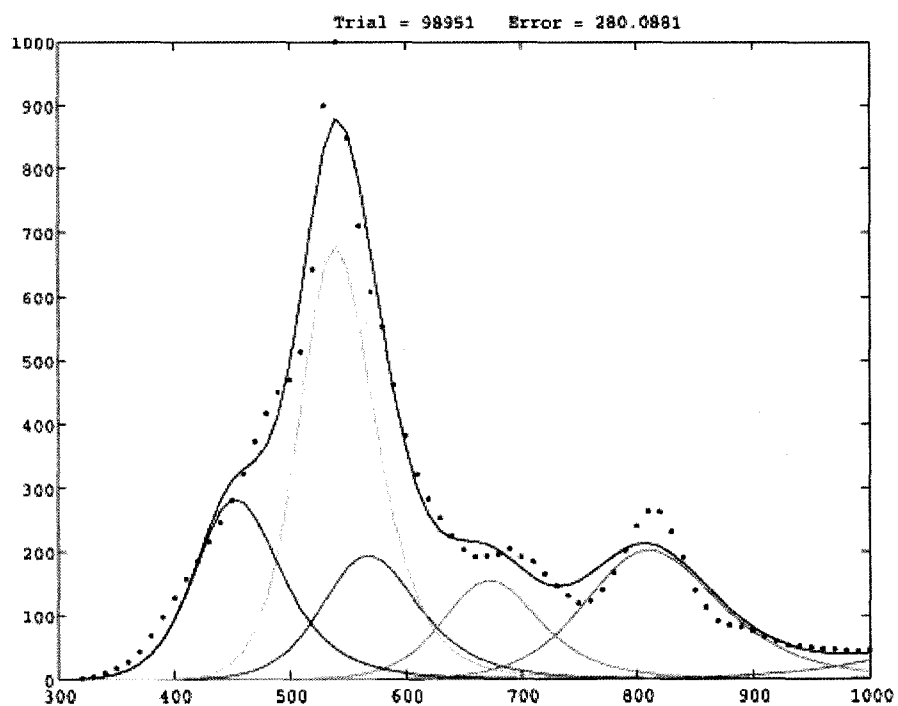


Figure 3.20: Deconvolution of the CO₂ acid-treated spectrum using a second order Polanyi-Wigner equation, producing a satisfactory fit. With larger iterations and more peaks, a better fit is possible. However, there is a trade off based on the fit and computational time and for the purposes of these experiments the requirements were met with fewer iterations and peaks. The x-axis is temperature and the y-axis is in arbitrary units as described previously in section 2.9.1.

Table 3.1: Results for the calculation of $\Delta E_{d,i}$, N_i , and ν_i for the acid-treated carbon nanosheet CO₂ spectrum fit with a second order Polanyi-Wigner equation.

Peak i	$\log_{10}N_i$	$\log_{10}\nu_i$	$\Delta E_{d,i}$ (eV)
1	5.2717	0.0000	0.0534
2	4.7677	8.9488	1.1347
3	4.7400	11.4148	1.6243
4	2.7959	2.6388	2.7827
5	4.5572	6.3161	0.5690
6	4.9309	7.3698	0.8024

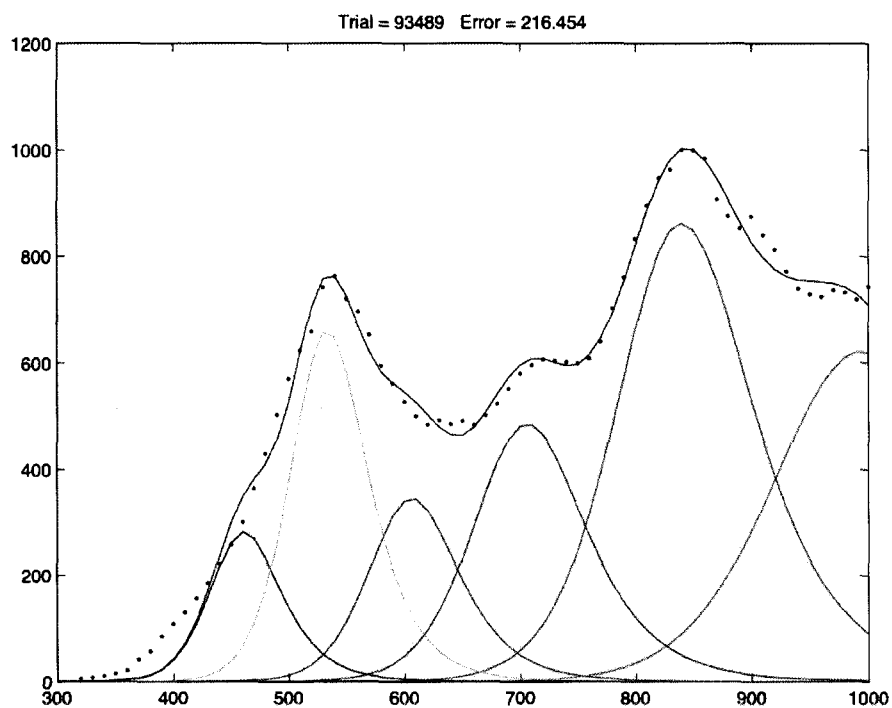


Figure 3.21: Deconvolution of the acid CO spectrum using a second order fit, providing a satisfactory fit.

Table 3.2: Results for the calculation of $\Delta E_{d,i}$, N_i , and ν_i for the acid-treated carbon nanosheet CO spectrum fit with a second order Polanyi-Wigner equation.

Peak i	$\log_{10} N_i$	$\log_{10} \nu_i$	$\Delta E_{d,i}$ (eV)
1	4.3704	8.4692	0.8048
2	5.1370	7.7492	1.3940
3	4.5564	8.8479	1.1147
4	5.1258	6.4498	1.4227
5	4.8035	8.0128	1.1964
6	4.7748	9.0988	1.0009

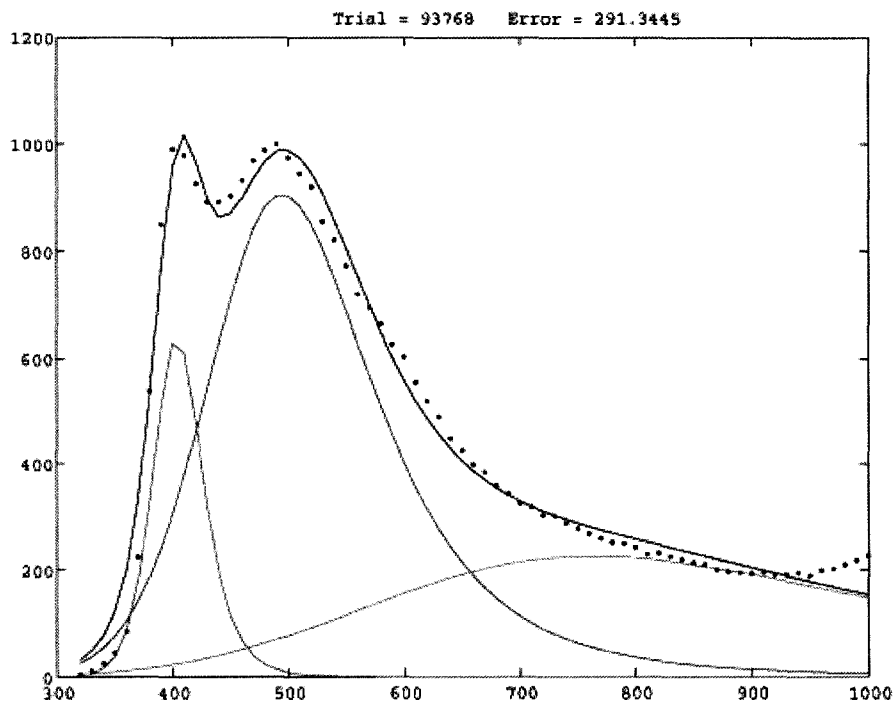


Figure 3.22: Deconvolution of the acid H₂O spectrum assuming second order, provides a satisfactory fit. The second feature is fit with the largest peak, supporting the dehydration events.

Table 3.3: Results for the calculation of $\Delta E_{d,i}$, N_i , and ν_i for the acid-treated carbon nanosheet H₂O spectrum fit using a second order Polanyi-Wigner equation.

Peak i	$\log_{10} N_i$	$\log_{10} \nu_i$	$\Delta E_{d,i}$ (eV)
1	5.2441	2.9020	0.3636
2	4.5555	11.3348	0.9181
3	5.1911	0.0032	0.2184

3.3.3 Summary of TDS experiments

Inspection of the oxygen decorated defects created by acid- and water-treatments to the carbon nanosheet system via TDS appears to be successful. From the data gathered, we were able to identify that the defects were terminated with both carboxylic acid and hydroxyl groups. We were also able to recognize surface reactions taking place on the surface of the carbon nanosheets for both functionalized and as-deposited nanosheet systems. These reactions created carboxylic anhydride groups on both functionalized and as-deposited sheets and with the functionalized nanosheets lactone groups were created as well. We were also able to show reduced hydrophobic behavior in the functionalized carbon nanosheets as evidenced by the large water peak (Fig. 3.16) at 120°C for both the acid- and water-treated samples. This data is in agreement with the XANES data and supports the assignment of the B1 and B2 feature to C=O π^* and C-O σ^* transitions respectively. Because oxygen has a higher effective nuclear charge, its orbitals lie at lower energies than the ones of the corresponding carbon atom. This results in overlap between the oxygen's $2p$ orbital with the carbon's $2s$ orbital. Therefore, the π^* transition of C-O will be slightly closer to the fermi level, but also the σ^* transition will be closer to the fermi level. Therefore, the DOS near the fermi level and just above the fermi level are increased for a C-O functional group. Using the Polanyi-Wigner equation and MATLABTM we were able to identify the stability of these defects—via their binding energies—in the nanosheet system and give a quantitative guess as to the number of defects created.

Due to the complications arising from both 1st and 2nd order processes occurring simultaneously in the spectra, contributions from the substrate and surface reactions exact quantification of defect density and defect classification was not possible. As a result of the interference from the substrate, high resolution XPS was utilized in an attempt to make an exact identification of the functional groups and the results are discussed in the next section.

3.4 High resolution X-ray photoelectron spectroscopy

Even though the TDS work was successful in the identification of the functional groups introduced via acid- and water-treatment of carbon nanosheets, there was a desire to know the exact local environment of the defects. The contributions from the substrate affected the deconvolution of the TDS spectra. Hence, due to its extreme surface sensitivity, x-ray photoelectron spectroscopy (XPS) was chosen for further investigation of these defects.

3.4.1 Interpretation of XPS data

The literature reveals numerous accounts of high resolution XPS studies on oxygenated carbon systems. The characterization of the graphene systems in [44, 53, 55] is representative of these systems. For these systems, the main peak at 284.6 eV is assigned to the C=C environment that dominates these systems. Shoulders that result at or around 286 eV are assigned to carbon atoms that are bound to a single oxygen atom via a single bond, such as with ether or alcohol type defects (Fig. 3.23 (a) and (b) respectively). Shoulders at 287 eV are assigned to carbon atoms that are double bonded to an oxygen atom, e.g. a carbonyl type defect (Fig. 3.23 (c)) and features at 289 eV assigned to carbon atoms that are bound to two oxygen atoms, e.g., a carboxylic acid (Fig. 3.23 (d)) [44].

As can be seen in Figure 3.24, a room temperature survey scan shows only carbon and oxygen present in the as-deposited, water- and acid-treated samples. The acid-treated spectrum shows oxygen content of 7.7% while the water-treated spectrum reveals content only a little lower at 6.8%. The as-deposited spectrum shows extremely high oxygen content of 6.8%. Previous results have shown values around 1% [20]. However, upon heating the samples to remove water absorbed on the surface

of the nanosheets from the atmosphere, the percentage of oxygen drops to $< 2\%$ for the as-deposited, 3.6% for the water-treated and 4.5% for the acid-treated spectra.

Inspection of the high resolution C(1s) spectra of the as-deposited nanosheets (Fig. 3.25), the acid-treated nanosheets (Fig. 3.26) and the water-treated nanosheets (Fig. 3.27) samples with sub-peak identification reveal structure similar to that illustrated by reference [44]. The sub-peaks of the acid- and water-treated samples show a fourth peak (illustrated in purple), that the literature has identified as a carbon atom bound to two oxygen atoms, not present in the as-deposited nanosheet spectra. After heating the nanosheet samples to $\approx 150^\circ\text{C}$, we see that this fourth sub-peak of interest disappears in the acid- and water-treated spectra (Fig. 3.28 and Fig. 3.29 respectively). However, this sub-peak *appears* in the as-deposited spectrum (Fig. 3.30), supporting our surface reaction hypothesis. Continued heating of the samples produces only the three sub-peaks for the as-deposited, acid- and water-treated samples as shown by the representative spectrum shown in Figure 3.31.

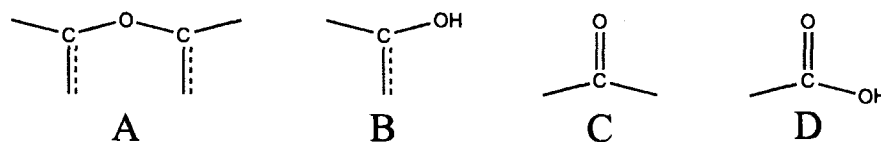


Figure 3.23: Schematic representation of the possible functional groups and bonding configurations of carbon atoms seen in high resolution XPS from sp^2 type carbon systems with oxygen defects. A) an ether type defect, B) an alcohol type defect, C) a carbonyl type defect and D) a carboxylic acid defect.

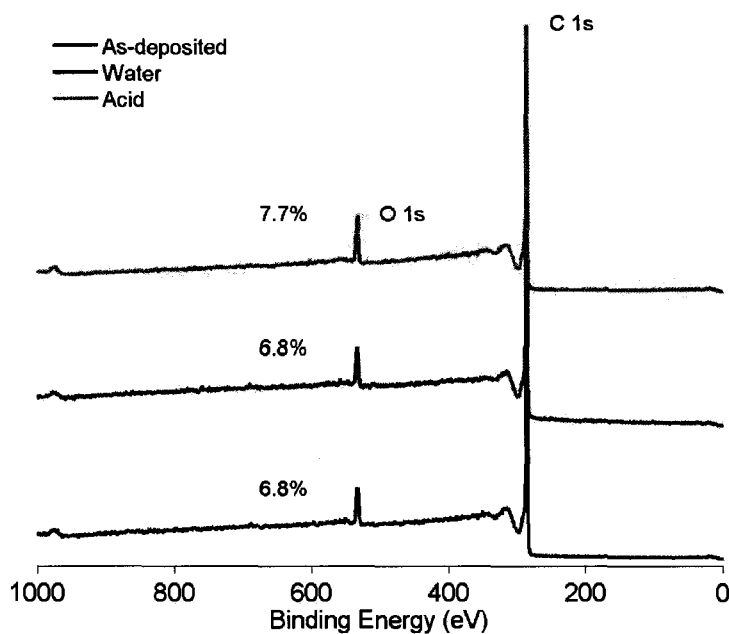


Figure 3.24: Room temperature survey scans of as-deposited (black), water-treated (blue) and acid-treated (green) carbon nanosheets. Oxygen and carbon are the only observable features in the spectra.

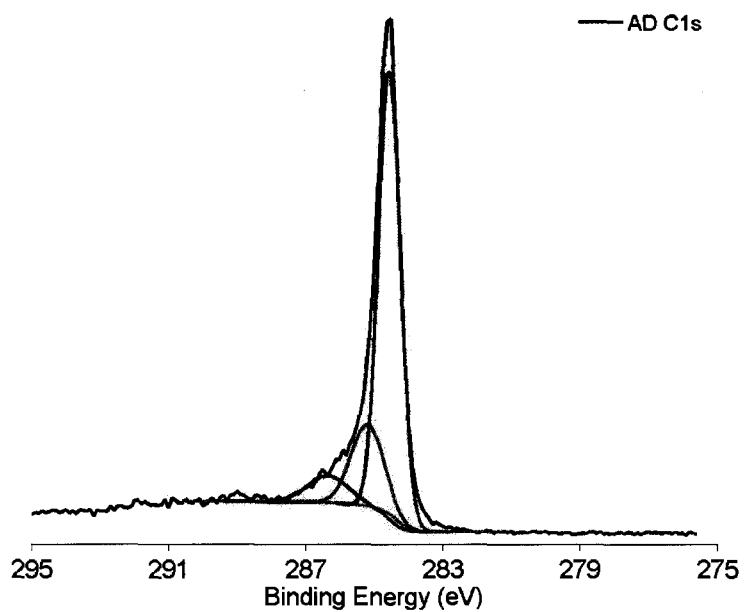


Figure 3.25: High resolution C(1s) spectrum of as-deposited carbon nanosheets with sub-peak identification. The blue sub-peak is assigned to the C=C of the system, the green sub-peak assigned to the C-O of the system and finally the red sub-peak to the C=O of the system. The y-axis has been removed to avoid confusion, but is in units of electron counts.

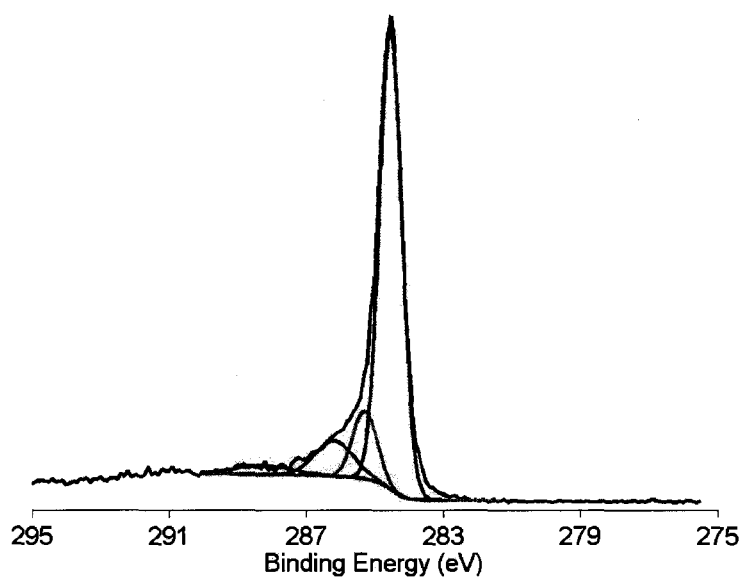


Figure 3.26: High resolution C(1s) spectrum of acid-treated carbon nanosheets with sub-peak identification. The blue peak is assigned to the C=C of the system, the green sub-peak to the C-O, the red sub-peak to the C=O, and finally the purple sub-peak to the COO of the system. The fourth sub-peak is not present in the as-deposited nanosheets implicating the change bonding of the C atoms in the system with defect creation.

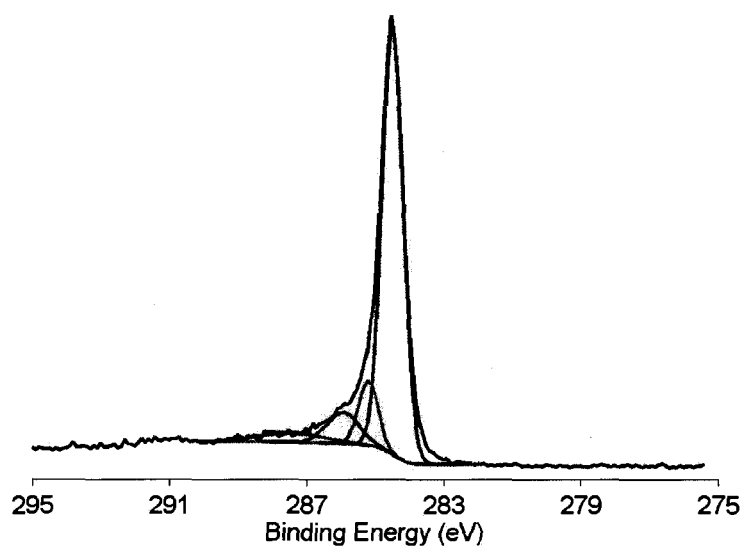


Figure 3.27: High resolution C(1s) spectrum of water-treated carbon nanosheets with sub-peak identification. The blue peak is assigned to the C=C of the system, the green sub-peak to the C-O, the red sub-peak to the C=O, and finally the purple sub-peak to the COO of the system. The fourth sub-peak is not present in the as-deposited nanosheets illustrating the change in bonding of the C atoms in the system with defect creation. The presence of the fourth sub-peak in the high resolution C(1s) spectra supports our findings of defect creation via a water-treatment as well as acid-treatment.

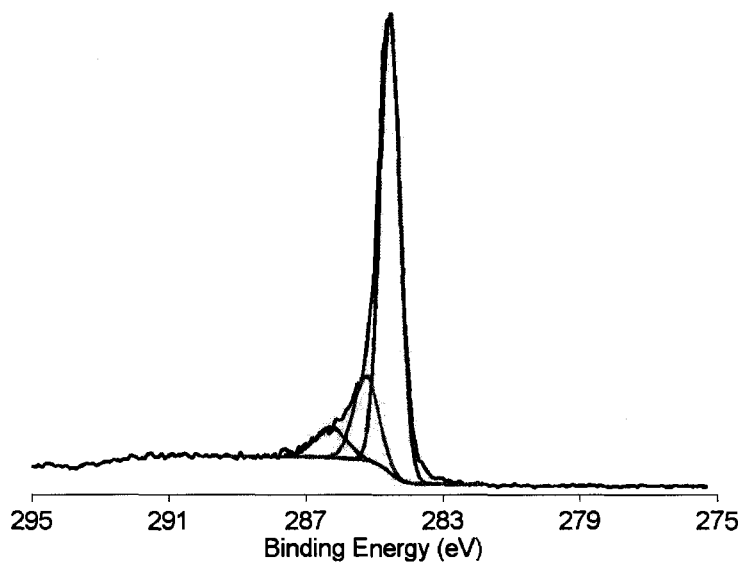


Figure 3.28: High resolution C(1s) spectrum of acid-treated carbon nanosheets after heating to $\approx 150^{\circ}\text{C}$, with sub-peak identification. The blue peak is assigned to the C=C of the system, the green sub-peak to the C-O, and the red sub-peak to the C=O. The fourth sub-peak, assigned to the COO of the system, has disappeared. This supports the disappearance of the oxygen signal from the survey scan and supports the surface reaction theory.

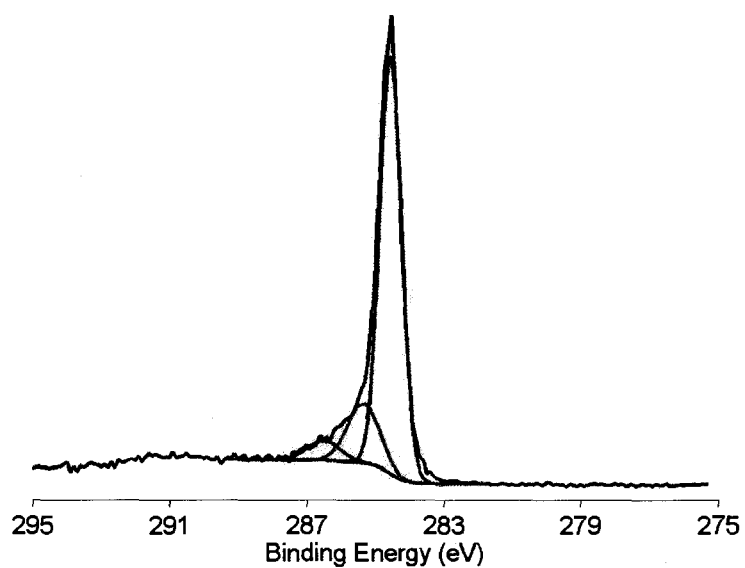


Figure 3.29: High resolution C(1s) spectrum of water-treated carbon nanosheets, after heating to $\approx 150^\circ\text{C}$ with sub-peak identification. The blue peak is assigned to the C=C of the system, the green sub-peak to the C-O, and the red sub-peak to the C=O. The fourth sub-peak, assigned to the COO of the system, has disappeared, supporting the surface reaction hypothesis.

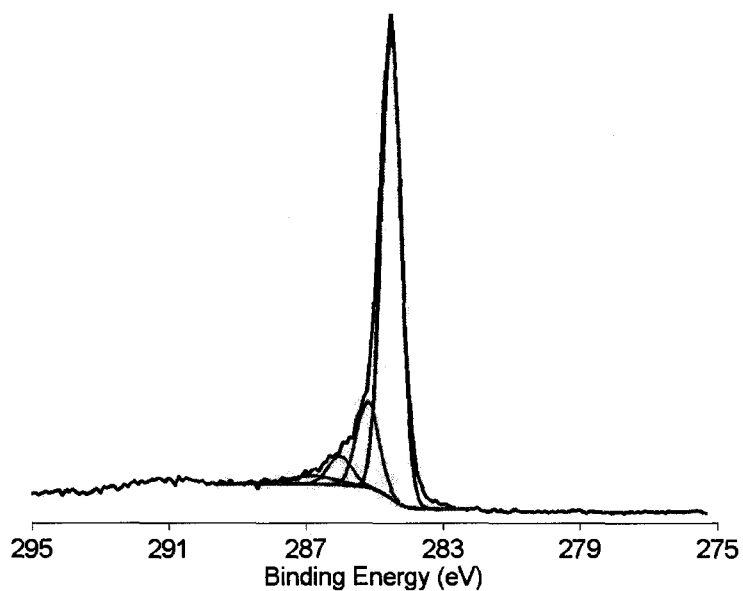


Figure 3.30: High resolution C(1s) spectrum of as-deposited carbon nanosheets after heating to $\approx 150^{\circ}\text{C}$ with sub-peak identification. The blue peak is assigned to the C=C of the system, the green sub-peak to the C-O, the red sub-peak to the C=O, and finally the purple sub-peak to the COO of the system. The appearance of the fourth peak in the as-deposited sample after heating supports the surface reaction hypothesis as well.

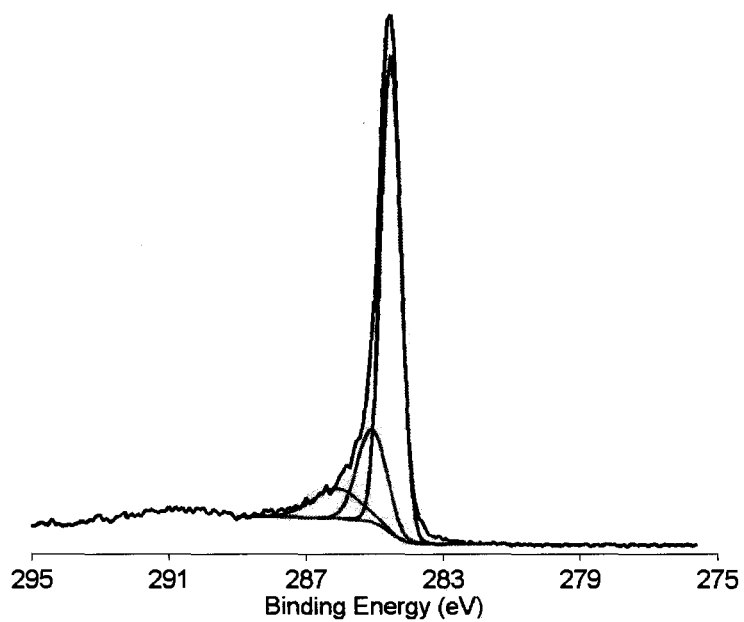


Figure 3.31: High resolution C(1s) spectrum of acid-treated carbon nanosheets after continued stepwise heating to $\approx 450^{\circ}\text{C}$. This spectrum is characteristic of all samples during and after the completion of the heating process.

High resolution O(1s) spectra are also present in the literature, but it is much more difficult to differentiate and assign these peaks. There are WO₃ impurities created during the acid treatment so we expect to see peaks at 530eV resulting from the WO₃ crystals (Φ Electronics). However, the peaks of interest are at 532eV for the CO peak generated by the creation of defects on the graphene walls of the nanosheets. The peaks at 532eV are expected to decrease as the temperature of the sample is increased, signifying desorption of oxygen from the surface. However, because no signature from the tungsten substrate is present in the survey scan, the WO₃ cannot be responsible for sub-peaks and its contribution is considered negligible due to a very low concentration of the crystals.

In agreement with the literature, however, exact assignment of the high resolution O(1s) sub-peaks is difficult. As shown in Figures 3.32 - 3.34, the as-deposited, acid-treated and water-treated spectra all produce two sub-peaks during the fitting routine. The relative intensities of the lower energy sub-peaks from the spectra support the association of the lower energy sub-peaks with water from the ambient absorbed on the surface of the samples. As shown in Figures 3.32 - 3.37 the percentages of the lower energy sub-peaks are 46% (as-deposited), 59% (acid-treated) and 63% (water-treated) at room temperature and 30% (as-deposited), 34% (acid-treated) and 18% (water-treated) after heating to $\approx 150^{\circ}\text{C}$, respectively.

With continued step-wise heating, all of the samples do not follow the same trend. When the as-deposited sample is heated to $\approx 350^{\circ}\text{C}$, the higher energy sub-peak becomes the weaker of the two peaks (Fig. 3.38). This stays the same when the sample is heated to $\approx 450^{\circ}\text{C}$ (not shown). For the acid-treated samples, the higher energy peak remains the stronger of the two peaks throughout the heating process as illustrated in Figure 3.39 (heating to $\approx 450^{\circ}\text{C}$). The water-treated samples produce yet another trend. The higher energy peak is the weaker of the two after heating to $\approx 200^{\circ}\text{C}$ (Fig. 3.40), but then becomes the stronger sub-peak after heating to \approx

450°C (Fig. 3.41). The complications of the sub-peak fitting routine make a direct assignment too difficult. However, the trends expressed by the changing relative percentages between the lower and higher energy peaks supports the data gathered from XANES and TDS in the assignment of oxygen decorated defects and the presence of surface reactions.

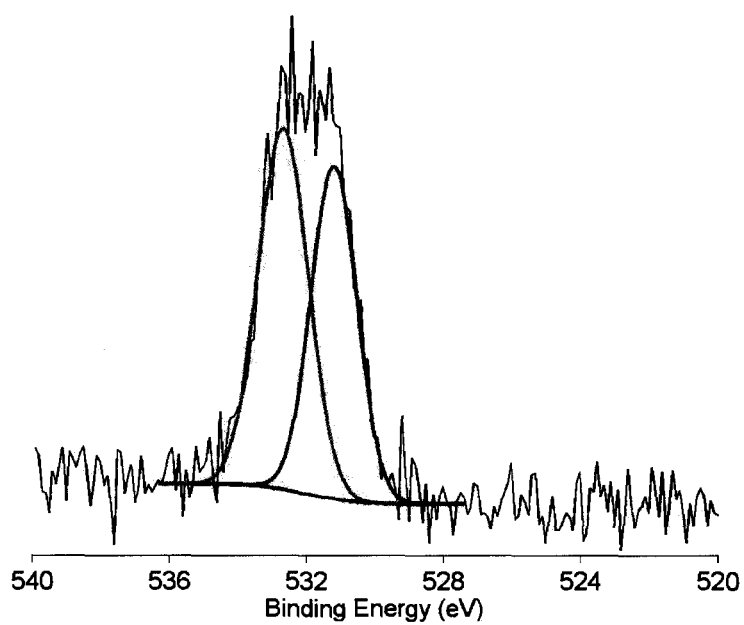


Figure 3.32: High resolution O(1s) spectrum of the as-deposited carbon nanosheets with sub-peaks. In our spectra, the high binding energy peak is attributed to C=O and the lower binding energy peak is attributed to both C-O and atmospheric water.

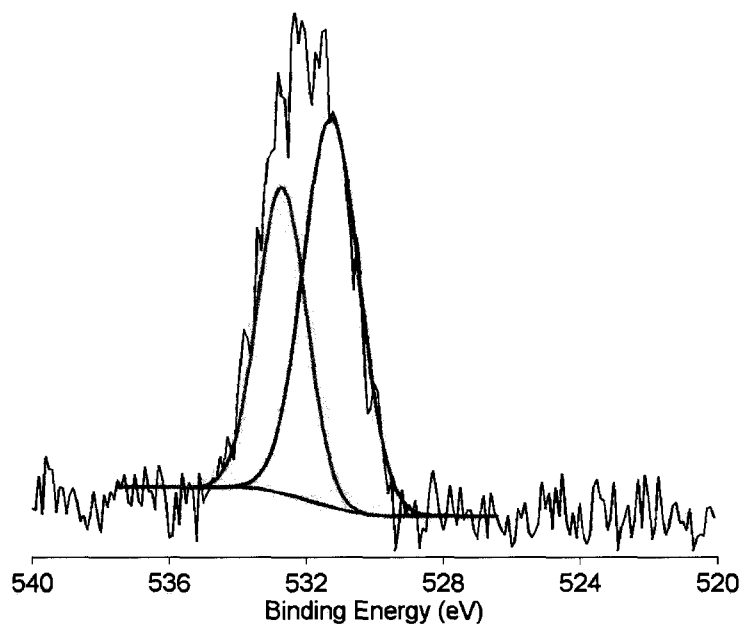


Figure 3.33: High resolution O(1s) spectrum of acid-treated nanosheets with sub-peaks. The change in relative peak intensity compared to the as-deposited nanosheet spectrum suggests that the lower energy sub-peak is associated with atmospheric water.

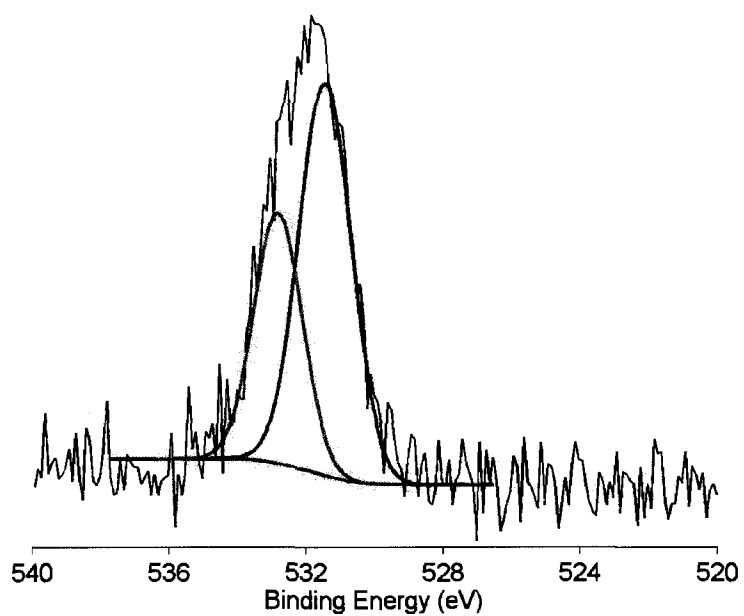


Figure 3.34: High resolution O(1s) spectrum of water-treated nanosheets with sub-peaks. The change in relative peak intensity compared to the as-deposited nanosheet spectrum suggests that the lower energy sub-peak is associated with atmospheric water.

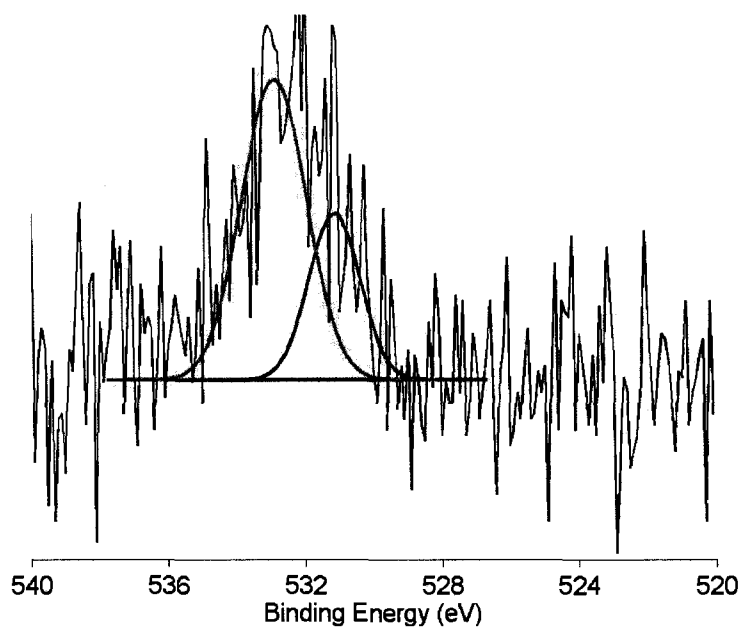


Figure 3.35: High resolution O(1s) spectrum of as-deposited nanosheets with sub-peaks after heating to 150°C. The intensity of the lower energy sub-peak has decreased, supporting the association of this sub-peak with atmospheric water. It should be noted that the overall intensity of these peaks is much lower than the intensities shown previously, but has been adjusted for the ease of viewing.

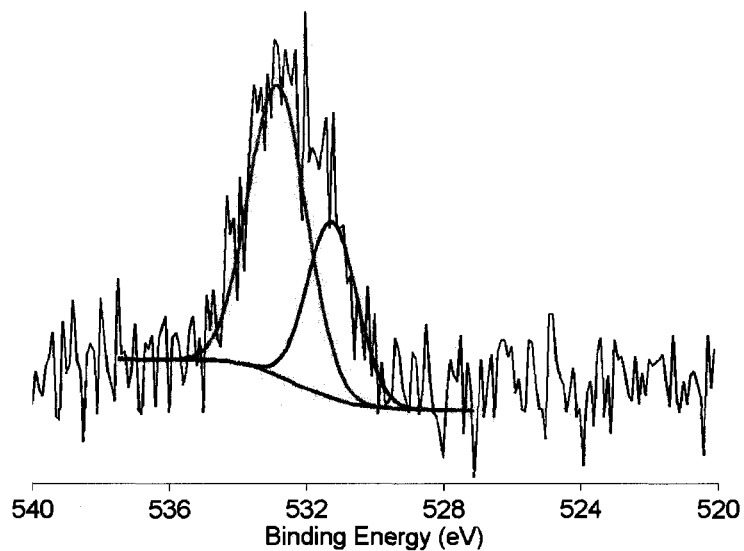


Figure 3.36: High resolution O(1s) spectrum of acid-treated nanosheets with sub-peaks. The intensity of the lower energy sub-peak has decreased, supporting the association of this sub-peak with atmospheric water. It should be noted that while the overall intensity of these peaks is less than for the room temperature acid spectrum, it is larger than the intensity for the 150°C as-deposited sample.

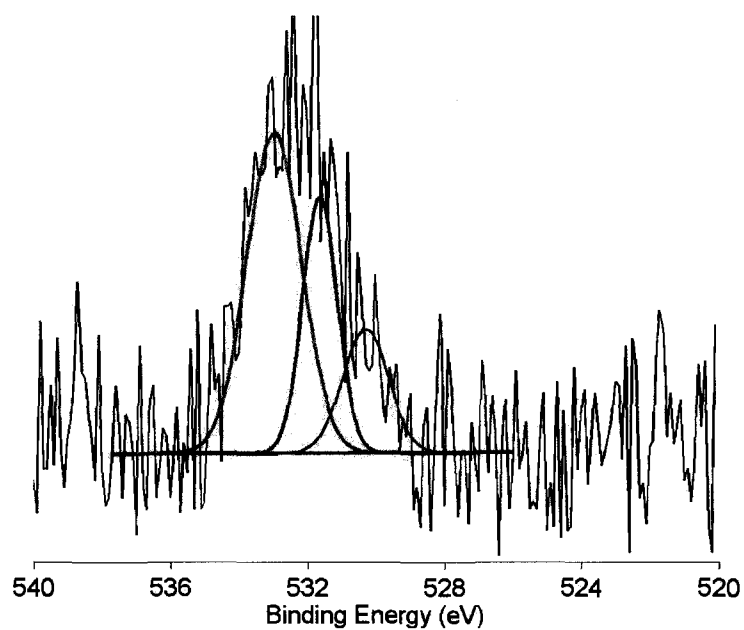


Figure 3.37: High resolution O(1s) spectrum of water-treated nanosheets with sub-peaks. The intensity of the lower energy sub-peak has decreased, supporting the association of this sub-peak with atmospheric water. Also, the appearance of the third sub-peak (represented in purple) supports the hypothesis of surface reactions taking place during the heating of the samples.

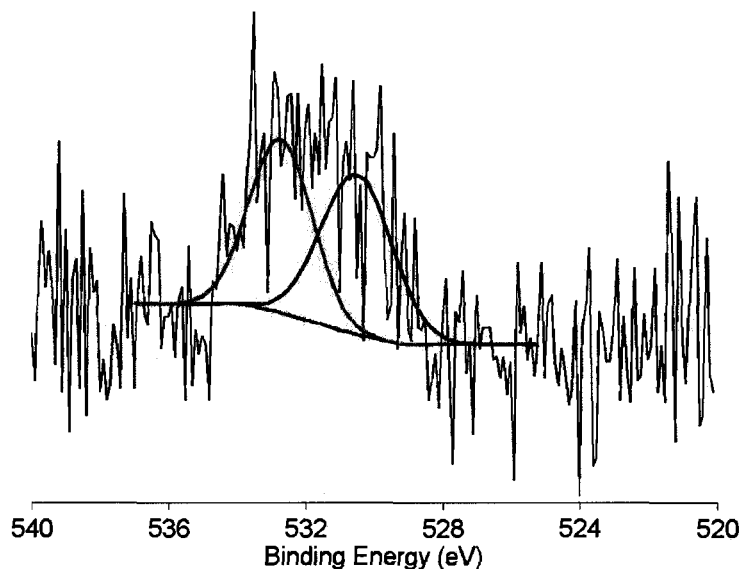


Figure 3.38: High resolution O(1s) spectrum of as-deposited nanosheets with sub-peaks after heating to $\approx 350^{\circ}\text{C}$ in which the lower energy peak becomes the stronger of the two sub-peaks (based on percentages, 51%).

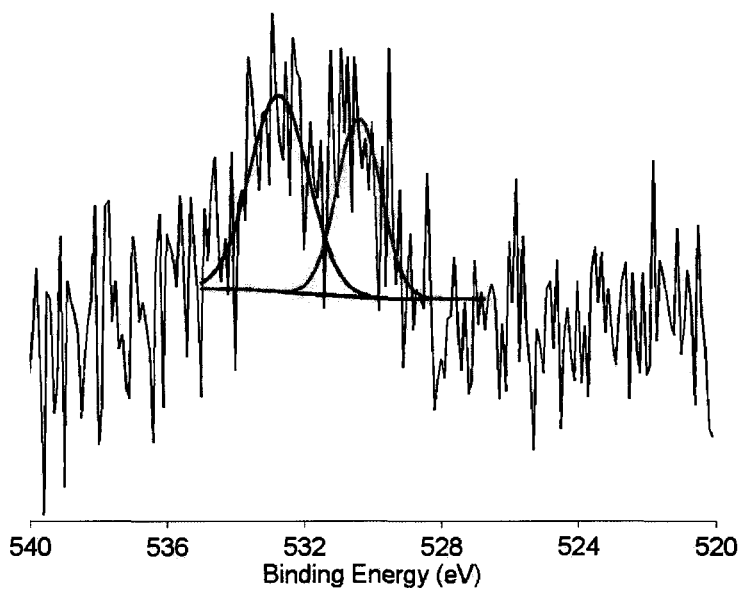


Figure 3.39: High resolution O(1s) spectrum of acid-treated nanosheets with sub-peaks after heating to $\approx 450^{\circ}\text{C}$ showing that the higher energy sub-peak remains the dominant peak (based on percentages, 60%).

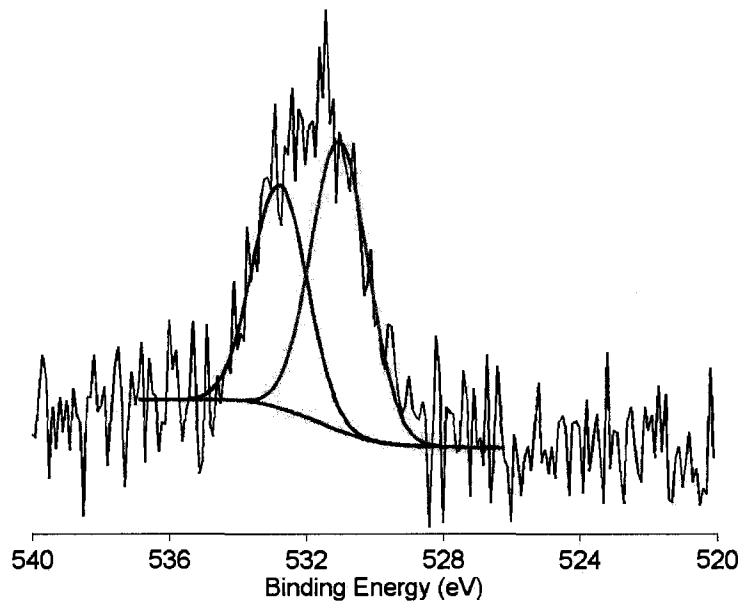


Figure 3.40: High resolution O(1s) spectrum of water-treated nanosheets with sub-peaks after heating to $\approx 200^\circ\text{C}$ at which point the lower energy sub-peak becomes the dominant peak.

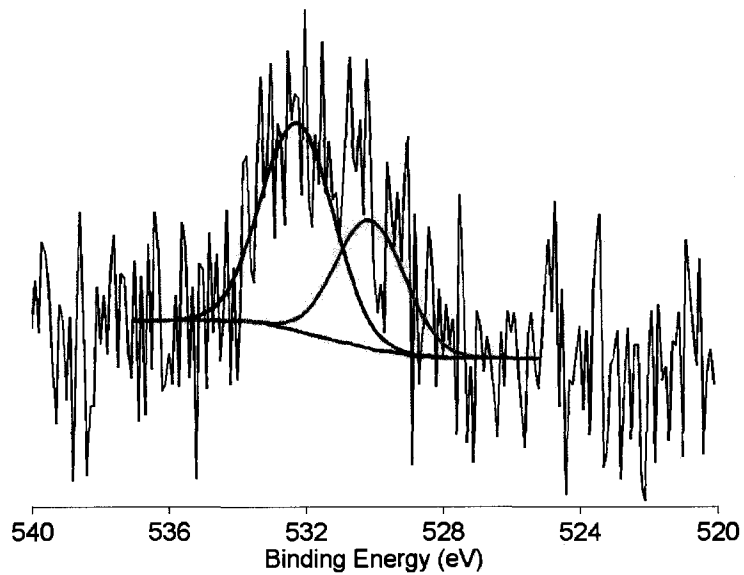


Figure 3.41: High resolution O(1s) spectrum of water-treated nanosheets with sub-peaks after heating to $\approx 450^\circ\text{C}$ at which point the higher energy sub-peak becomes the dominant peak.

3.4.2 Summary of XPS results

The high resolution XPS experiments resulted in sub-peaks for both the C(1s) and O(1s) spectra that are in agreement with values previously reported for carbon systems with oxygen defects. Sub-peak fitting of room temperature, high resolution C(1s) scans produced three sub-peaks in the as-deposited nanosheets and four sub-peaks in both the acid- and water-treated samples. The fourth sub-peak that is present in the acid- and water-treated samples, but missing from the as-deposited samples, supports our assertion of functionalization via acid- and water-treatments. The literature has identified this fourth sub-peak as corresponding to a COOR-type functional group. As the samples are heated this fourth sub-peak disappears from the acid and water spectra. However, after heating the as-deposited nanosheets to $\approx 150^\circ\text{C}$, the fourth sub-peak appears in the spectrum. After subsequent heating the sub-peak is no longer present. These trends support the presence of surface reactions that take place on the carbon nanosheets during the XPS and TDS experiments. The temperature at which these changes are observed ($\approx 150^\circ\text{C}$) also supports dehydration events. These events result in the creation of additional functional groups, i.e. anhydrides and lactones.

The sub-peak fitting of high resolution O(1s) scans also produced results in agreement with the TDS experiments. The lower binding energy sub-peaks were associated with atmospheric water and with the CO functional groups. The higher binding energy sub-peaks were associated with the COOR-type functional groups. This is in agreement with the literature. However, the presence of the C-O and the C=O sub-peak in the as-deposited nanosheets complicates deconvolution of the data. Because there are peaks in the TDS spectra that we associate with anhydrides, we would expect to see C-O and C=O sub-peaks in the XPS spectra, but only after heating the samples and creating functional groups.

Due to the complications of the sub-peak fitting, an exact assignment of the struc-

tures to specific bonding arrangements is difficult. Also, the atomic percentages of oxygen present in the samples are not enough to account for the sub-peak structure seen in the C(1s) spectra alone. However, the trends observed from the C(1s) and O(1s) spectra both provide evidence for surface reactions that take place during the heating of the nanosheet samples, in agreement with the results of the TDS work. Only oxygen and carbon are seen in the survey scans which also support the assignment of the defects created to oxygen decorated defects first made as a result of the XANES work.

The sizes of the resulting sub-peaks of the XPS spectra can be used to give an estimation of the relative surface concentrations. However, this requires the XPS system to be calibrated to an extent that was not possible for these experiments. Further calibration of a system dedicated only to the study of functionalized nanosheet, along with samples treated for varying amounts of time are required for a more conclusive identification of the surface composition of the functionalized nanosheets.

3.5 Summary and discussion of functional group characterization

The nature of defects created in the graphene system of carbon nanosheets was characterized via x-ray absorption near-edge spectroscopy (XANES), thermal desorption spectroscopy (TDS) and high resolution x-ray photoelectron spectroscopy (XPS). As a result, it was shown that functional groups are created by both acid- and water-treatments of the nanosheet system. The spectroscopic features observed via XANES were attributed to C-O σ^* transitions (B2) and C=O π^* transitions (B1). The removal of the defect features was observed by heating the samples to $> 320^\circ\text{C}$, suggesting that the oxygen containing groups could be removed by thermal activation. The presence of oxygen containing functional groups was verified and the nature of the groups identified using TDS as defined in Table 3.4. Signature peaks observed in the acid-treated spectra consisted of carboxylic acids (CO_2 , $\approx 280^\circ\text{C}$), anhydrides (CO and CO_2 , $\approx 400^\circ\text{C}$), lactones (CO_2 , $\approx 530^\circ\text{C}$) and hydroxyls (CO, $\approx 570^\circ\text{C}$). These peaks along with the H_2O spectrum allowed for the identification of surface reactions on the nanosheets, resulting in the anhydride and lactone type peaks, therefore assigning the defects created to carboxylic acids and hydroxyl groups which is in agreement with the literature and supports the XANES findings. Signature peaks observed in the spectra of the water-treated samples were anhydrides (CO and CO_2 , $\approx 400^\circ\text{C}$), along with the second peak in the H_2O spectrum, again supporting surface reactions. Due to the lack of carboxylic acid peaks (CO_2 , $\approx 280^\circ\text{C}$) or hydroxyls (CO, $\approx 570^\circ\text{C}$) in the spectra, however, these surface reactions become more important. It is likely that the signal from the carboxylic acid type defects was ignored due the CO_2 spectrum from the substrate and that the water-treatment did not result in the formation of hydroxyl groups. The final support for the surface reactions during the heating of the samples came from the as-deposited nanosheets with the presence of an anhydride peak (CO and CO_2 , $\approx 400^\circ\text{C}$) with no defects observed in the room temperature

Table 3.4: Results of TDS peak identification

Spectrum	Peak Temp (°C)	As-deposited	Acid-treated	Water-treated
CO ₂	280	n/a	carboxylic acid	n/a
	400	anhydride	anhydride	anhydride
	530	n/a	lactone	n/a
CO	400	anhydride	anhydride	anhydride
	570	n/a	hydroxyl	n/a
H ₂ O	120	atmospheric H ₂ O	atmospheric H ₂ O	atmospheric H ₂ O
	160	n/a	n/a	dehydration rxns
	210	n/a	dehydration rxns	n/a
	tail	dehydration rxns	dehydration rxns	dehydration rxns

XANES spectra. This again supports surface reactions on the nanosheet samples. The observed trends in the H₂O spectra for all samples show evidence supporting the reduction of the hydrophobic behavior of carbon nanosheets after functionalization. High resolution XPS was not able to specifically identify changes in bonding through the sub-peak fitting routine due to difficult deconvolution. As-deposited samples presented a higher O:C ratio than previously observed. One concern is the “aging” of the carbon nanosheets as mentioned in Boehm et al [55] and the incorporation of oxygen into the material. The oxygen content of the acid- and water-treated samples was identified as being higher than that of the as-deposited samples. This agrees with the TDS and XANES data. Though quantification is not possible without calibration, it may be possible to quantify the reduction in hydrophobicity via the oxygen content. Also, the observed trends and values supports the presence of oxygen decorated defects in the functionalized nanosheets and the surface reactions that take place during the heating of the samples.

In summary, based on our data we were able to identify the functional groups created via the acid-treatment as carboxylic acids and hydroxyls while the water-treatment only produced carboxylic acids. The idea of creating functional groups via water treatment however is quite counter intuitive. As mentioned previously, the as-

deposited nanosheets are quite hydrophobic and graphene structures are chemically inert, making interactions with deionized water unlikely. However, this is not without precedent. Yang et al [56] found that sonication of nanotubes in deionized water produced functional groups as well. The primary (CH_3) carbon atoms can oxidize to primary alcohols (C-OH), then aldehydes (C=O) and finally to carboxylic acids (COOH). Secondary carbon atoms (CH_2) can oxidize to secondary hydroxyls (C-OH) and then to ketones (C=O) while the tertiary carbon atoms (CH) can only oxidize to alcohols (C-OH). The findings in reference [56] support our assignments, with the B1 XANES peak being representative of $\text{C=O } \pi^*$ transitions due to the presence of carboxylic acid groups and ketone groups. Also, the lack of hydroxyl groups for the water-treated samples in the CO TDS spectrum suggests that there is not enough energy to oxidize the tertiary CH atoms. From the TDS work of Zhao et al [37] we know that there are CH sites available for this oxidation process in the as-deposited nanosheets at lower binding energies, making these sites more likely to be oxidized with low energy (heating only to $\approx 100^\circ\text{C}$).

The presence of the hydroxyl feature in the acid treated samples supports our claim that we are creating di-vacancy defects, decorated with hydrogen and hydroxyl groups as well. By creating these decorated defects, we should see a larger contribution of OH than observed with the water-treated samples. We do in fact see a large B2 feature in the XANES (assigned to $\text{C-O } \sigma^*$) that is a result of these hydroxyl groups as well as the COH in the carboxylic acids. We also see the hydroxyl peak in the CO TDS spectra.

Density functional theory calculations were applied to the system and reproduced the spectroscopic features (in simplified form) observed in the XANES spectra [14]. From the density of states calculations it was suggested that the conductivity of the nanosheets could be increased through the introduction of defects in the graphene system of the nanosheets. Experimental evidence, for the first time, was provided that

measured the conductivity of the vertical graphene layers of the nanosheet system. The increased conductivity of the nanosheet system through chemical modification was shown by the modified and unique procedure.

Finally, a routine for the further investigation of defect control, including the concentration of defects, was outlined. It was shown that by using a MATLABTMscript, data from the TDS experiments were fit with 2nd order Polanyi-Wigner equations and values such as the number of molecules desorbing from the surface for a particular temperature were calculated. With further calibration of the XPS system, it would be possible to compare the atomic percentages of oxygen (and decreases based on heating) to the values seen from the TDS work. These values could then be used to identify concentrations of different defects created at similar sites, i.e. both carboxylic and hydroxyl defects at Stone-Wales defects, versus the same defects (i.e. hydroxyls) present on different sites (i.e. Stone-Wales or vacancy). Because this was not considered critical for the identification of these defects and in supporting the development of carbon nanosheets as a viable option for high surface area electrodes, a more rigorous investigation is needed.

In the next chapter, the applicability of functionalized carbon nanosheets is illustrated by their use as nanostructured templates during an ALD process. The procedure and results of this process will be presented and discussed.

Chapter 4

Atomic layer deposition of titanium dioxide nanostructures

4.1 Introduction to atomic layer deposition (ALD) of titanium dioxide

Atomic layer deposition (ALD) is a process for depositing thin films on substrates of varying composition. ALD makes use of self-limiting, sequential surface reactions to maintain precise control over the thickness of the films. ALD is similar to CVD, however, ALD is split into two half-reactions and the precursor materials are kept separate. This allows for atomic-scale deposition control. The use of ALD makes it possible to deposit atomically thin films of uniform thickness over porous substrates, inside deep trenches and around particles [57].

High surface area films are of importance to a variety of applications. ALD allows for the growth of uniform films over substrates with varying geometries, including nanostructured substrates. Therefore, as proof of concept for the applicability of functionalized carbon nanosheets, ALD was used to deposit TiO_2 films using carbon nanosheets as a template. The results are uniform, high surface area TiO_2 films which can be used in a variety of applications.

4.2 Motivation for deposition of TiO₂ on carbon nanosheets

Metal oxides are an important group of materials with a wide range of thin film applications. One example is TiO₂ which can be used in photocatalysis [58], photovoltaics [59] and in gas sensors [60]. Many of these applications require a nanostructured film with a very large surface area and with good control of grain size and phase composition. Several authors have reported on the deposition of such nanostructured TiO₂ films. This includes both depositions of nanobowls, nanotubes and other structures using atomic layer deposition (ALD) [61], as well as anodization of titanium to fabricate nanoporous TiO₂ films [62]. An alternative method to produce nanostructured TiO₂ with a large surface area is to use a template structure in combination with a deposition process with very good step coverage such as ALD. In the ALD technique, reactant pulses are separated by purging pulses. Reactant gas species saturate the surface of the substrate during each pulse and growth is achieved through self-limiting surface reactions. This enables the ALD technique to conformally cover geometrically complicated surfaces since gradients in the partial pressure of the reactant gas species can be compensated with longer gas pulses.

Recently, a new type of carbon nanostructure, called carbon nanosheets, has been produced using radio frequency plasma enhanced chemical vapor deposition (RF PECVD) [22]. As can be seen in the scanning electron microscopy (SEM) image in Figure 4.1, the nanosheets consist of standing structures made up of 1-7 graphene layers perpendicular to the substrate.

The sheets are typically $\approx 1 \mu\text{m}$ high and are formed on top of a $\approx 10 - 20 \text{ nm}$ thick graphite-like film. Surface areas of about $1000 \text{ m}^2/\text{g}$ have been observed for the nanosheets [22] making these structures suitable as a template for oxide films. Furthermore, the nanosheets are conducting which can be an important requirement in many applications (e.g. photovoltaics). For a more detailed description of the

synthesis and characterization of nanosheets, see references [6, 7].

A problem with using carbon nanosheets is that nucleation of an oxide film from molecular precursors in, e.g. an ALD process, may be limited on the fairly inert graphene-like surfaces. In principle, this can be handled by the introduction of defects which would increase the sticking coefficient of precursor molecules. In this chapter we demonstrate ALD of nanostructured TiO_2 on nanosheet templates and also show how the nucleation of the oxide film can be controlled by an acid-treatment which induces defects in the graphene surface.

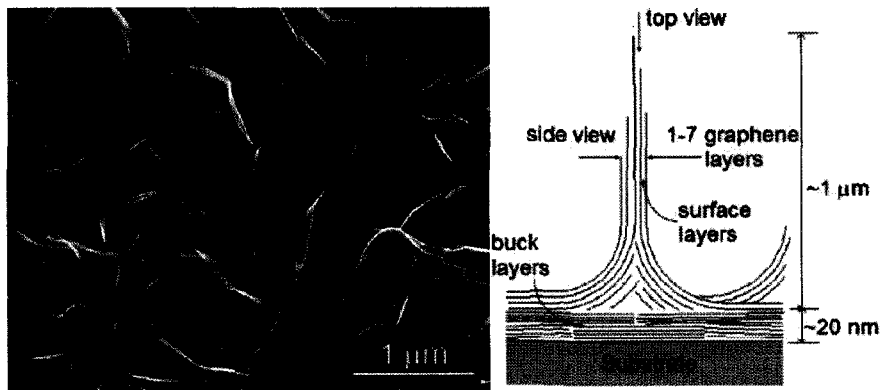


Figure 4.1: Left: SEM image of carbon nanosheets deposited on a tungsten substrate. Right: Schematic figure of the nanosheet structure.

4.3 Experimental setup

Carbon nanosheets were grown using a Radio Frequency Plasma Enhanced Chemical Vapor Deposition (RF PECVD). RF power was inductively coupled into the deposition chamber using a copper, planar coiled antenna. Tungsten foil as-received (purchased from Alfa Aesar, 0.1 mm, 99.95% metal basis) was used as substrates for the purpose of this study. No special treatment was applied before or after the acid treatment of the nanosheets. Using a resistive four-inch heater, substrates were heated in a hydrogen atmosphere to a growth temperature around 700°C. Once the desired temperature was reached, methane was introduced as the carbon feedstock at a flow rate of 4 sccm. The hydrogen flow rate was kept at a constant 6 sccm throughout the growth process. Growth time was kept at 15 minutes for these experiments. After growth, the methane flow rate was returned to zero, with the plasma still ignited for 3-5 seconds, to remove any amorphous carbon from the surface of the nanosheets. The samples were then inspected via scanning electron microscopy (SEM Hitachi S-4700) operating at 15kV and Raman spectroscopy (Renishaw inVia, excitation laser 514nm) for a morphological background.

TiO₂ thin films were deposited using the precursor combination TiI₄ and H₂O in an onsite-built hot-wall horizontal flow-type ALD reactor that has been described in detail elsewhere [63]. TiI₄ (Alfa Aesar, 99.9% purity) was used as the titanium source and evaporated from a semi-open quartz boat inserted at 108°C. Prior to the deposition the TiI₄ was heat treated at 100°C at 2 Torr to remove any water. Deionized water was used as the oxygen source and was evaporated from an external container at room temperature. N₂ was used as purging gas and carrier gas for the TiI₄ and H₂O. Four pulses were used to deposit the TiO₂ and these four pulses are referred to as a cycle. The first pulse was a TiI₄ pulse, the second and fourth pulses were purging pulses and the third pulse was the H₂O pulse. All pulses were 30 seconds to ensure saturation of the surface. 50, 75 and 100 cycles were used to deposit TiO₂

on the nanosheets. The nanosheets were placed on a TiN-coated titanium substrate holder and all depositions were made at a deposition temperature of 300°C and a total pressure of 2 Torr.

The non acid treated carbon nanosheets were used as-received. The acid treatment was made in concentrated HCl at 95°C for 6 hours, a more detailed description can be found elsewhere [14]. Samples used for the TEM study were deposited on tungsten TEM grids. TEM images and EELS were made on a FEI Tecnai F30ST (300 kV) instrument. A LEO 1550 instrument was used to make the SEM images. GIXRD were made on a Philips Xpert X-ray diffractometer using Cu K α radiation. The relative Ti content in the films was examined by XRFS using a Spectrolab X2000 spectrometer.

4.4 Results and discussion

Figure 4.2 shows an SEM picture of a titanium oxide film deposited on a carbon nanosheet template at 300°C using 100 ALD cycles with TiI₄ and H₂O as precursors. A detailed description of the TiO₂ ALD process can be found in reference [64]. The first pulse is the metal source pulse, the second pulse is a purging pulse, the third pulse is an oxygen containing pulse and the fourth and final pulse is a second purging pulse. If the process parameters are properly chosen, the number of cycles used rather than the concentrations of precursors in the gas phase determines the growth rate. As can be seen in Figure 4.2, a more or less continuous film is obtained after 100 cycles with fairly large crystallites, about 5-20 nm. However, these films contain pinholes suggesting that the conducting nanosheet substrate is not completely covered.

The lack of adsorption sites, defects, on the inert surface of sp² hybridized carbon can cause nucleation problems [65] and lead to an island growth mechanism. This was also observed in this study as illustrated in Figure 4.3. It can be seen that 50

ALD cycles result in a film of sparsely separated islands of titanium dioxide. After 75 ALD cycles the film still consists of islands and a continuous film requires at least 100 ALD cycles (see Fig. 4.2). Furthermore, all films deposited in this study on as-deposited nanosheets contained pinholes which can be explained by a slow nucleation rate during the initial stages of growth.

The nucleation can be improved by increasing the defect density on the carbon nanosheets. Recently, Coleman *et al.* have demonstrated that an acid-treatment of the nanosheets with HCl induce defects in the graphene structure [14]. Such defects can be favorable adsorption sites for precursor molecules and an improved nucleation rate is therefore possible. This was investigated in a set of experiments using carbon nanosheet samples acid treated in HCl at 95°C for 6 hours. A more detailed description of the acid treatment can be found in reference [14]. As can be seen in Figure 4.4, the nucleation density was considerably improved by the acid treatment and a more or less continuous film of titanium dioxide is obtained after only 50 ALD cycles.

The film appears to consist of separated crystallites of titanium dioxide surrounded by an amorphous matrix of the same material although some short range order is noticeable. Furthermore, no indication of pinholes can be seen in the films deposited on the acid-treated nanosheets. X-ray fluorescence spectroscopy (XRFS) showed that the amount of TiO₂ deposited also increased for the acid-treated samples. The intensity of the Ti peak in the XRFS spectra for acid-treated samples was about 70% higher compared with non-acid treated samples deposited in the same experiment.

X-ray diffraction (XRD) analysis showed that titanium oxide films on both the as-deposited and acid-treated nanosheets contained the anatase phase of TiO₂ (see Fig. 4.5). XRD measurements on samples deposited with only 50 ALD cycles did not show any crystalline peaks, which can be explained by the small crystallite sizes as well as the small amount of material deposited.

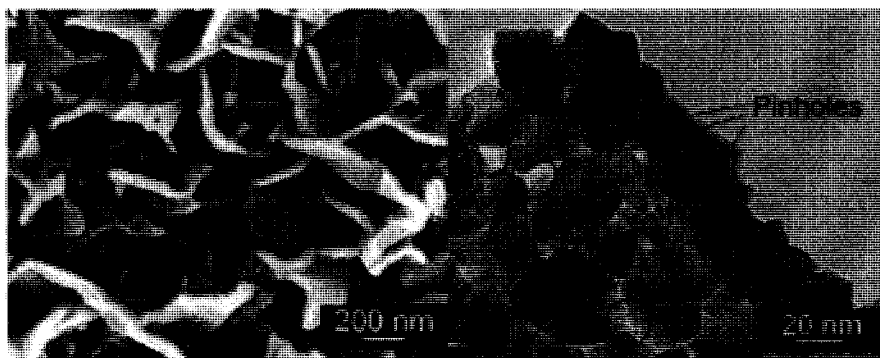


Figure 4.2: Left: SEM image of a titanium dioxide film deposited on as-received nanosheets deposited on W at 300°C using 100 ALD cycles. The nanosheets are viewed from the top. Right: TEM image of a sample with carbon nanosheets grown on a tungsten TEM grid using the same deposition parameters as the sample in the SEM image. The single nanosheet is viewed from the side. Pinholes are highlighted in the TEM image.

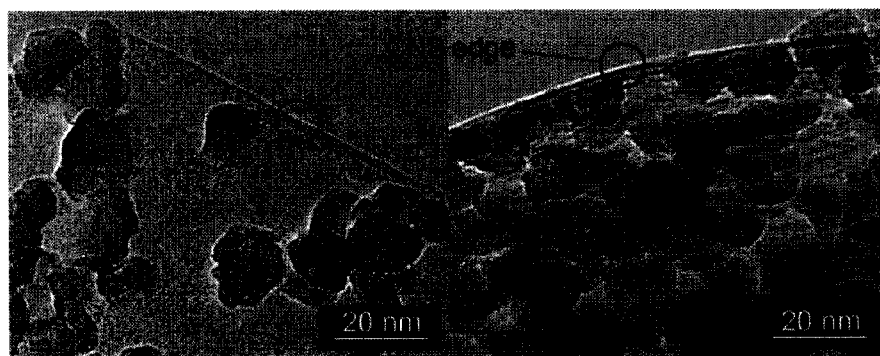


Figure 4.3: Samples deposited with TiO_2 at 300°C on as-received carbon nanosheets showing a non-continuous film after 50 ALD cycles (left) and 75 cycles (right). The sheets are viewed from the side.

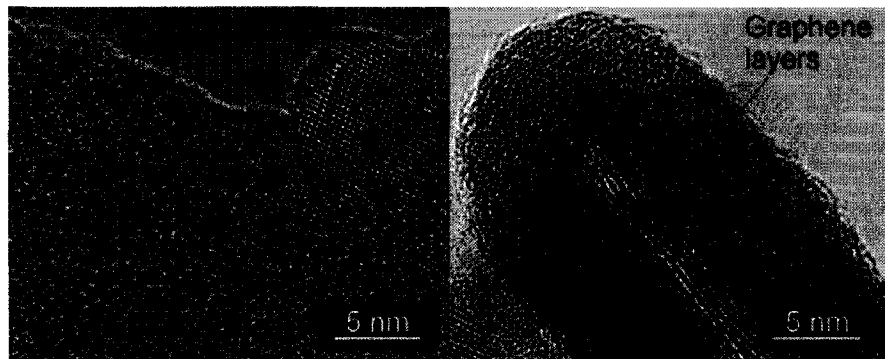


Figure 4.4: TEM image of acid-treated nanosheets deposited with 50 ALD cycles of TiO_2 at 300°C . Left: Sample viewed from the side perpendicular to the graphene planes. Right: Sample viewed from the side showing the graphene layers of a carbon nanosheet.

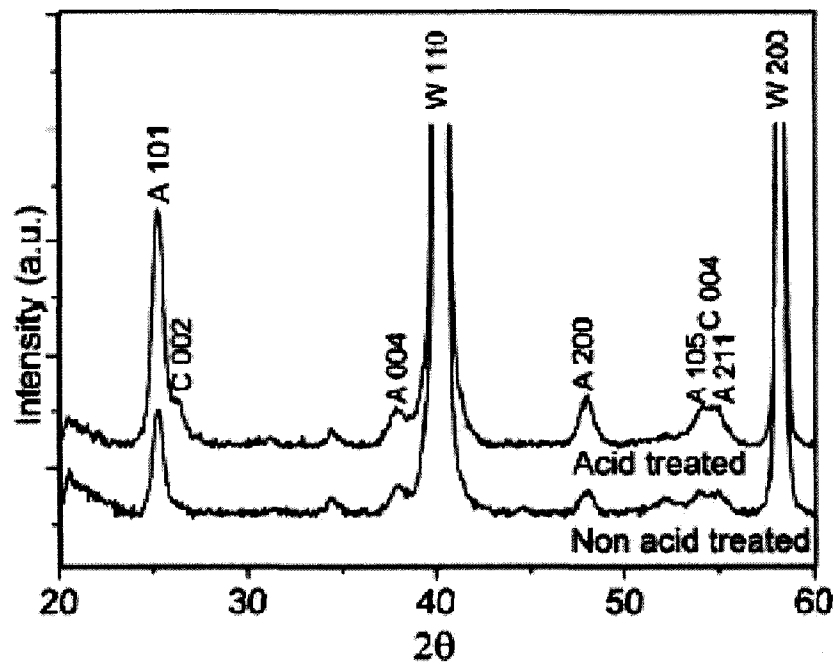


Figure 4.5: Diffractogram of samples deposited with 100 ALD cycles on acid-treated nanosheets and non acid-treated nanosheets. Peaks attributed to anatase, nanosheets and tungsten are marked with A, C and W, respectively.

No rutile reflections could be found in any of the deposited films. This agrees with an earlier ALD study using the same precursor combination and a deposition temperature of 300°C, where anatase was also deposited [64]. It should be mentioned that if there is a lattice match between the substrate and any of the TiO₂ phases, rutile may be formed [66]. However, in this study there is no lattice match between the substrate used and either of the two titanium dioxide phases.

The Raman study confirmed that anatase is present in all films. Typical Raman spectra of samples deposited on both acid-treated and non acid-treated carbon nanosheets can be seen in Figure 4.6. The samples were deposited under the same conditions using 50 ALD cycles while the spectrum in the insert in Figure 4.6 was deposited using 100 ALD cycles. The well known bands of anatase can be seen at 147, 404, 521 and 635 cm⁻¹ [67]. The intensity is higher on the acid-treated samples since more material is deposited on this substrate.

The results above clearly show that the nucleation of the TiO₂ film is improved by acid-treatment. As discussed above, this procedure is known to introduce defects [14] and we can therefore attribute the improved nucleation to the presence of such defects. They can act as reactive adsorption sites, especially if they are OH-terminated. Gas phase species will thus have more adsorption sites on acid-treated samples, which will result in a higher initial growth rate. The adsorbed species also adsorb stronger to these sites and the surface mobility of the adsorbed precursor molecules becomes significantly reduced. This fact together with the higher nucleation rate will result in the initial formation of a larger number of smaller crystallites on the acid-treated nanosheets, in agreement with the results above. Furthermore, the difference in nucleation rate can also explain the difference in crystalline quality observed in Figures 4.2-4.4. The slower initial nucleation and growth on the non acid-treated nanosheets result in larger, well-defined crystalline grains and a film with many pinholes while the defect-rich acid-treated substrate initially yields a less well-crystallized film with a

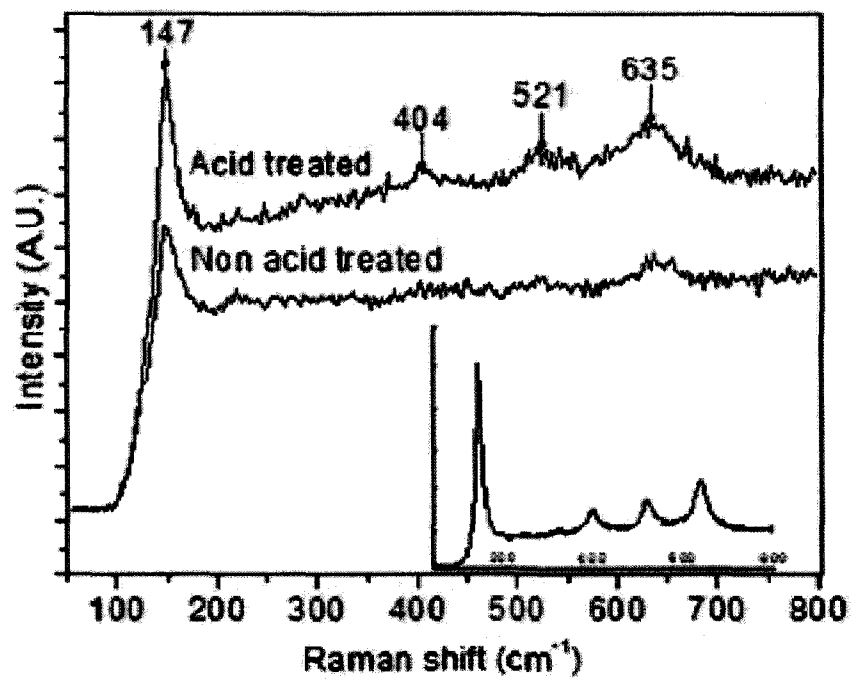


Figure 4.6: Raman spectra of TiO_2 deposited on acid-treated and non acid-treated carbon nanosheets using 50 ALD cycles. The insert shows a Raman spectrum of an acid-treated sample deposited using 100 ALD cycles.

mixture of crystalline grains and amorphous matrix, but without pinholes. It should be noted, however, that amorphous regions were also occasionally observed on the non acid-treated sample. In general, this was found on edges where the top of the sheets has been broken off and where the edge was several nanometers thick (see Fig. 4.7).

This can be explained by the fact that edges of the as-deposited carbon nanosheets are H-terminated [37], Bagge-Hansen:2008aa since the deposition is carried out in a methane/hydrogen atmosphere. These H-terminated edges are not very reactive adsorption sites. However, thicker edge regions created by the damaged nanosheets will expose highly reactive edge atoms with dangling bonds. The unsaturated bonds will quickly react with the ambient and to a large extent be terminated by OH groups due to dissociative adsorption of H₂O. Thus the damaged edges will resemble the defects in the acid-treated samples and also give similar nucleation and growth conditions.

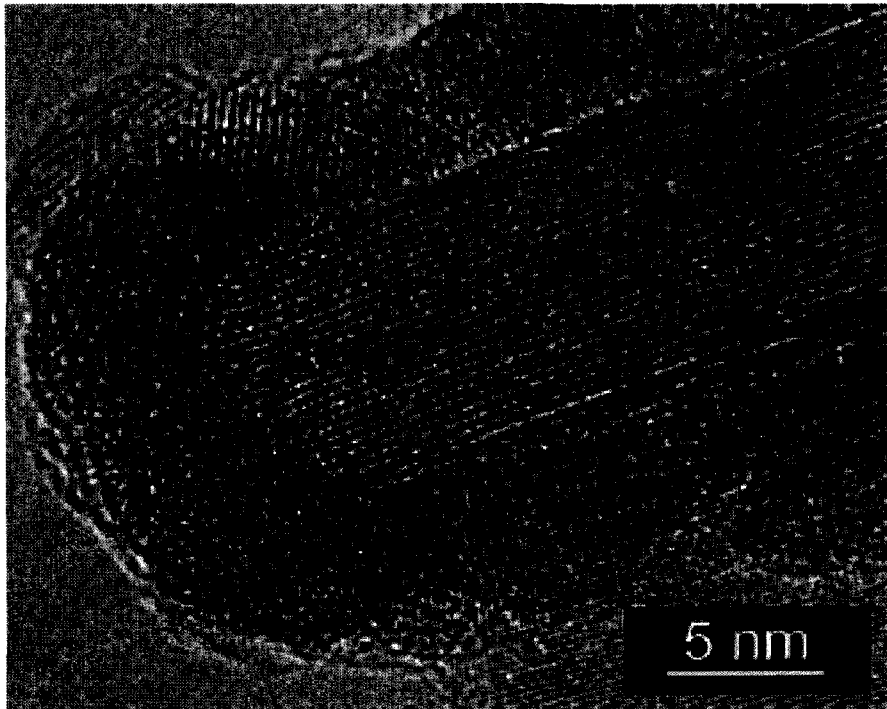


Figure 4.7: TEM image of carbon nanosheet where the top has been broken off and the titanium dioxide deposited on the top is amorphous.

4.5 Summary of carbon nanosheets as nanostructured template

In summary, thin films of nanostructured TiO_2 have been successfully deposited with ALD using carbon nanosheets as a template. The initial nucleation and growth of the films could be controlled by an acid-treatment process prior to film growth which is known to introduce defects in the nanosheets. The TiO_2 on the defect-rich nanosheets nucleated faster and resulted in a film with no observable pinholes consisting of crystalline grains in an amorphous matrix. XRD and Raman spectroscopy confirmed that the crystalline parts of the films contained the anatase TiO_2 phase. Although we have yet not measured the surface area of the TiO_2 it is clear that the nanosheet template, together with the ALD technique makes it possible to make nanosheet-like structures of this oxide with surface areas similar or higher than the surface area of the template ($\approx 1000 \text{ m}^2/\text{g}$). We propose that the carbon nanosheets in combination with ALD can be used to deposit a wide range of sheet-like nanostructures of different metal oxides for a potential use in numerous applications.

In further support of carbon nanosheets being used as high surface area electrodes, the nanosheets were spin cast with a variety of polymers to study the nanosheet polymer surface interactions. As a result, the conformal coating of carbon nanosheets and incorporation into polymeric films was confirmed. During this investigation, a process to transfer as-deposited nanosheet films to zero thermal-budget substrates was identified. As a proof of concept measurement, the nanosheets were spin cast with polymers commonly used in organic photovoltaics (such as MEH-PPV) and photoluminescence measurements made. These results will be presented and discussed in the next chapter.

Chapter 5

Conformal coating and transfer of carbon nanosheet films to a zero thermal budget substrate

5.1 Introduction

The previous chapter addressed the applicability of functionalized carbon nanosheets. We successfully demonstrated the effects that functionalizing the nanosheets can have on the creation of nanostructured TiO₂ films and illustrated the continuous films that were a result of the acid-treated nanosheets. In this chapter, the process of conformally coating the carbon nanosheets with a polymeric material and the transfer of the as-deposited nanosheet film to a zero, thermal-budget substrate is described. A brief introduction to the materials and process used is provided, but not discussed in detail. This work was performed in support of the development of carbon nanosheets as a high surface area electrode material. As a proof of concept, carbon nanosheets were incorporated into a polymeric film of poly[2-methoxy-5-(2'-ethyl-hexyloxy)-1,4-phenylene vinylene] (MEH-PPV) and the photoluminescence of the composite measured.

5.2 Motivation for the conformal coating of carbon nanosheets

Recently carbon-based nanostructures and materials have become a popular subject of research due to their unique thermal, mechanical, electrical, and optical properties. For example, the strong C-C bonds of graphene-based systems allow for excellent thermal conduction at room temperature and the conjugation of the sp^2 lattice enables extremely high electron mobility. The use of carbon nanostructures as a component in polymer composites has been limited by several factors including the lack of ability to control the alignment of the structures, poor dispersion of the material in the polymer matrix, incompatibility with the high temperatures required for the nanostructure growth, and the presence of, or complication of removing, non-carbon species.

Carbon nanosheets are new class of carbon nanostructure composed of free-standing, vertical graphene structures (1 - 7 layers) and horizontal basal planes (10 - 20 layers) with a measured surface area of 1086 m²/g [20]. Because of their high surface area and electronic robustness [68], carbon nanosheets offer unique possibilities for use as high surface area electrodes. However, initial experiments involving the incorporation of the nanosheets into a polymeric film revealed some difficulties (Fig. 5.1). Polymers were spin cast onto the nanosheet films, resulting in the formation of large voids and air bubbles in the films.

Because nanosheets, like other carbon nanostructures, require a high growth temperature, growth of carbon nanosheets on temperature sensitive substrates is not a viable option. Therefore, the ability to easily transfer the nanosheets and pattern them via standard photolithography techniques [69, 70], without the use of a heat treatment step [71], greatly increases the potential of nanostructures in various applications.

Several approaches currently being investigated for the transfer of other carbon

nanostructures include solution based printing methods [72], self-assembly [73], surface modification [74], micro-contact printing, hot embossing [75, 76] and electric field assisted patterning [77]. However, the largest of the problems is retaining the substrate normal morphology during the transfer process. Recent success has been reported via casting a polymer solution around the nanotube arrays, but removal of the polymer [78, 79] is not mentioned. Other attempts have also been made to create free films of carbon nanotubes and to transfer them to different substrates [76, 80], but each offer difficulties of their own. Sunden et al [76] showed success in transferring carbon nanotubes via a micro-contact procedure. The nanotubes retained their vertical orientation, but because of the catalyst involved in the growth, the nanotube tips were broken when the growth substrate was removed. Huang et al [80] were able to transfer nanotubes but needed to float the films in a HF/H₂O solution and then had to lift off the films with a grid which is then used as a stamp during the micro-contact procedure.

In this chapter we illustrate the use of novel spin-coating techniques to conformally coat and fill nanosheets with a variety of polymers. A thermosetting polyimide was chosen for its chemical resistance and thermal properties. Room temperature vulcanizing (RTV) silicone was chosen for its widespread use in applications and solvent resistance. Polystyrene was chosen for its solubility in common solvents. As a result of the conformal coatings, carbon nanosheet films were successfully transferred to zero thermal-budget substrates without damaging the original morphology.

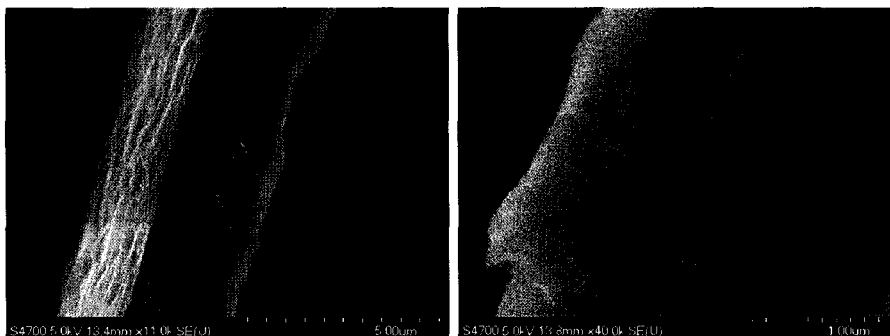


Figure 5.1: Unsuccessful spin casting of carbon nanosheets with polymeric material. The surface interactions between the polymer and the nanosheets produced poor wetting and no filling between the nanosheets with polymeric material. Further support for the poor incorporation of the nanosheets into the polymeric material is the high density of nanosheet edges visible from these cross-sectional images.

5.3 Experimental

For the purposes of this study, carbon nanosheets were grown using a standard radio frequency plasma enhanced chemical vapor deposition (RF PECVD) chamber previously described in detail in [6, 7, 19] and in section 2.2.1. Typical deposition parameters were a substrate growth temperature of $\approx 700^\circ\text{C}$, a RF power of 900W, and a total pressure of $\approx 100\text{mTorr}$. Growth times ranged from ten to twenty minutes depending on the desired sheet height and density. The substrates were heated to growth temperatures in a hydrogen atmosphere (flow rate of 6 sccm). Once the desired temperature was reached, methane was introduced into the chamber at a flow rate of 4 sccm. After deposition, the methane rate was cut to zero with the plasma still ignited in order to remove any amorphous carbon that was present on the side-walls of the sheets. Finally, the substrates were allowed to cool in a hydrogen atmosphere before removing to ambient. During these experiments, silicon wafers (100mm, (100), SSP, both doped and un-doped) were used as growth substrates. The substrates were used as-received with no special treatment prior to deposition. The samples were not subjected to any post-deposition treatments before characterization or the start of the transfer process. Samples ranged from 5mm x 5mm wafer pieces to whole 101.6mm wafers, therefore allowing the successful transfer of large areas of nanosheet films.

The surface morphology of the deposited carbon nanosheets was characterized via scanning electron microscopy (SEM Hitachi S-4700) operating from 5kV to 30kV in SE collection mode. The degree of graphitization was determined using Raman (Renishaw inVia, excitation laser 514nm). Use of the Ferrari method, as described in reference [33], allowed for the comparison of various growths utilizing the I_D/I_G ratio obtained via Raman spectroscopy.

Polystyrene (Alfa Aesar, FW 125000-250000, beads) was used as the transfer agent. The transfer substrates were made from room temperature vulcanizing (RTV)

silicone. 2-Butanone (MEK), N-methylpyrrolidone (NMP) and mineral spirits were the solvents used during these experiments. Spin casting was accomplished using a Chemat KW-4A Precision Spin-Coater with a GAST, model DOA-P101-AA, vacuum pump.

5.4 Results and discussion

Spin casting is a simple technique that can be used to produce very thin, and uniform, polymeric films. The technique utilizes centrifugal force, linear shear stress, and homogeneous evaporation of a solvent on a substrate that is rotating about its central axis. The speed at which the substrate is spinning, volatility of the solvent, along with viscosity of the polymer solution and the substrate size typically determine the thickness of the film, as illustrated by Figure 5.2. However, during the spin casting of carbon nanosheets, it was determined that in order for a conformal coating and complete wetting of the nanosheets, particular interest must be paid to the solvent of choice and the viscosity of the polymer solution. A solvent that was too volatile did not allow for complete coverage of the nanosheet film and resulted in only partial coatings. Solvents that were too effective, i.e. a solvent that the polymer material had an extremely high solubility in, quickly re-dissolved the already cast polymer, resulting in poor film quality and large material consumption. Polymer solutions that were too viscous did not allow for the filling between sheets and solutions that were too dilute produced no coating at all.

Also, the standard practice for addition of the polymeric material involves adding the material while the substrate is spinning at what is considered a low spin rate (e.g., ≈ 1000 rpm) for a small amount of time and then ramp to a high spin rate (e.g., ≈ 4000 rpm) for a longer period of time. For coating of the carbon nanosheets, this practice was not followed. The polymer solutions were found to be incorporated into

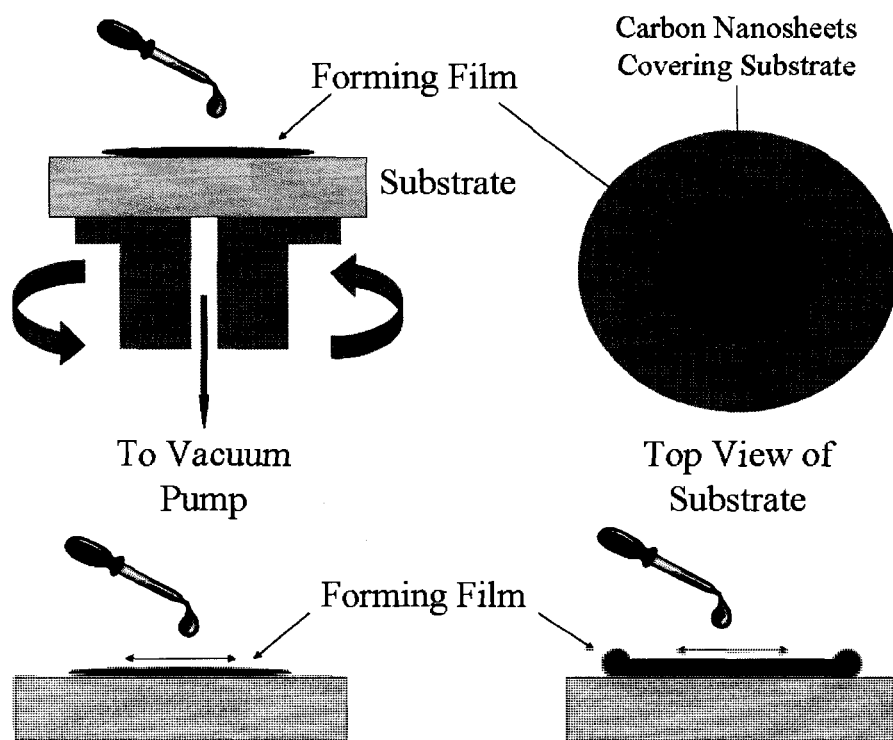


Figure 5.2: Schematic illustrating the spin casting setup and procedure that results in the creation of a uniform film. During spin casting, the substrate (light blue) is placed on a chuck and is held in place via vacuum. As the substrate is spinning, material (dark blue) is added to the center of the substrate and the film is created. Typically, the thickness of the film will depend upon the viscosity of the solution, the volatility of the solvent, and the speed at which the film is cast.

the nanosheets best when initially added to a stationary substrate and then ramped to a low and finally high spin rate. Subsequent loadings need to be applied via the standard method to prevent the solvent from re-dissolving the already cast polymeric material.

By casting the initial film with a stationary substrate, ramping to a low spin rate (< 400 rpm) and finally ramping only to a moderate rpm (≈ 1000 rpm) we were able to conformally coat the nanosheets as shown in Figure 5.3 (a). Subsequent loadings gradually filled the spaces between the sheets and resulted in uniform films, free of voids (Fig. 5.3 (b), (c)).

As mentioned previously, polystyrene was chosen as a polymer for casting because it is cheap, readily available and can be easily dissolved in common solvents. One of the areas of concern was the role of the solvent in the spin casting and wetting process. The polystyrene solutions were made using different solvents (MEK and NMP) and at different viscosities. As a result many different polystyrene/nanosheet films were made and then set aside for subsequent inspection. During this process, it was observed that as the polystyrene films—cast as previously described—dried, the composite films appeared to buckle, as illustrated in Figure 5.4. Further investigation demonstrated that this process occurred more frequently on un-doped silicon wafers and that the film could be removed with forceps without damaging the film. Inspection of the growth wafer after removal of the film showed no sign of a graphene structure left on the surface. Also discerned was the ability to control the cracking of the film (as seen in Fig. 5.4) by removing the excess polystyrene from the edges of the growth wafer. During the spin casting the excess polystyrene wraps around and under the edge of the substrate. If this is removed before it dries then the film does not undergo the stress created by contraction towards the center of the substrate and towards the edge which results in the cracking.

These observations resulted in a new branch of research focused on the transfer

of the carbon nanosheet films to non-growth substrates. Of obvious significance were polymeric substrates, because, as discussed above, the temperatures required for the growth of carbon nanosheets eliminated polymeric substrates as an option. Due to its resistance to solvents and flexibility, silicone (PDMS) was of interest.

Silicon wafers, for support, were placed on top of the drying polystyrene and then removed after the polystyrene/nanosheet composite had formed. Other wafers were then spin cast with solutions of RTV silicone and mineral spirits (it is important to note that the silicone solutions were prepared by placing the silicone in the solvent before it vulcanized) and then placed in contact with the exposed basal layers of the nanosheet film. The polymer solutions were given time to dry and then the top wafer was removed. Our first efforts resulted in tearing of the polystyrene/nanosheet film (as shown in Fig. 5.5). To avoid this issue, the top 'support' wafer was placed on a hot plate and heated to $\approx 200^\circ\text{C}$, above the T_g , but below the T_m of polystyrene. This allowed for the removal of the top wafer with minimal damage to the underlying nanosheet film. The polystyrene was then washed away with MEK and/or NMP—MEK showed the best results—by immersing the film in solvent and then using a pipette and clean solvent while holding the substrate at an angle (as demonstrated in Fig. 5.6). The clean nanosheet films could then be left on the silicon wafer or the silicone adhesive layer could be removed. This process is outlined in the schematic in Figure 5.7.

Continued work with this process resulted in the creation of flexible substrate, nanosheet films. As outlined by the schematic in Figure 5.8, we were able to remove the polystyrene/nanosheet composite film and place the adhesive layer directly on the basal layers without spin casting as well. These flexible substrates were created through solution as well as by doctor blading the silicone across the back of the composite film with a razor blade (as shown in Fig. 5.9).

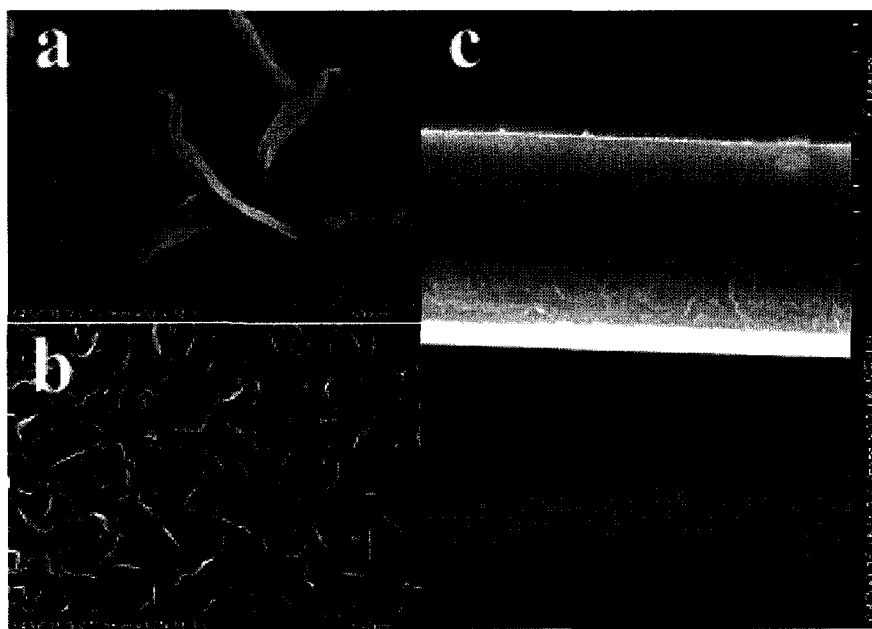


Figure 5.3: The conformal coating of nanosheets (a) as made evident by the thickness of the individual sheet in the center of the image (thickness $\approx 40\text{nm}$ as compared to as-deposited thickness $\approx 1\text{nm}$). Subsequent loadings fill the spaces between sheets (b) and produce films with no voids (c).

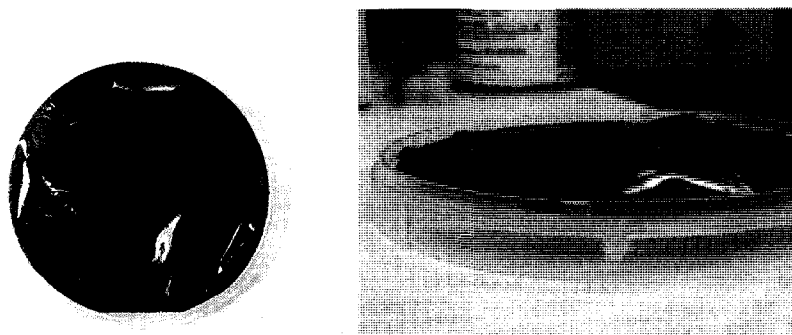


Figure 5.4: Buckling of polystyrene/nanosheet composite films as observed during the drying process.

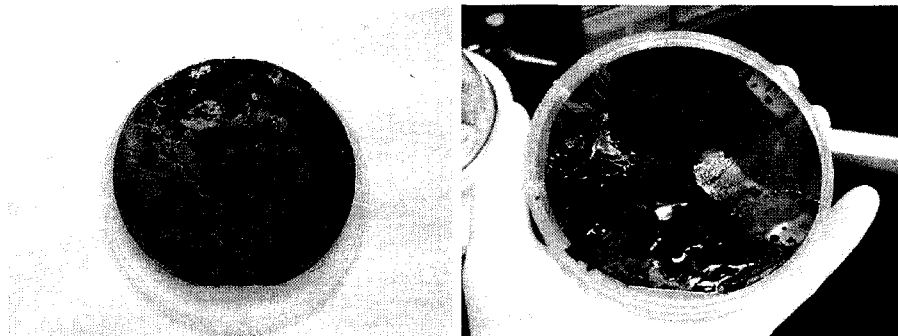


Figure 5.5: Damaged nanosheet/polystyrene film as a result of removing the support wafer without prior heating.

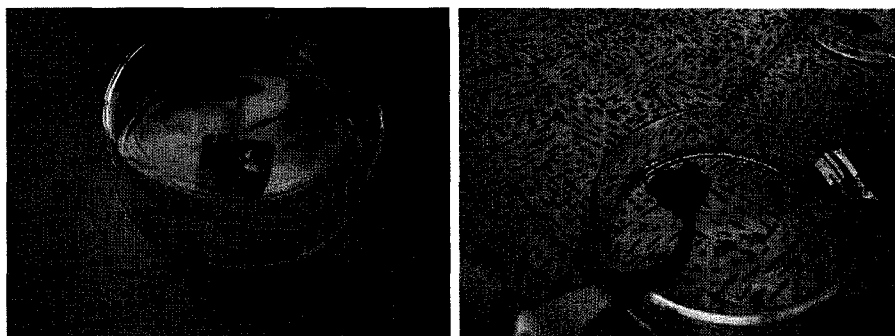


Figure 5.6: Pipette technique used to rinse away remaining polystyrene film after removal of the support substrate. These images are taken from smaller samples early during the testing of this technique but are representative of the process.

Raman spectroscopy (Fig. 5.10) and SEM (Fig. 5.11) were used to characterize the post-transfer nanosheets. As illustrated, during the described transfer process the nanosheets retain their original morphology. The nanosheets are not charging during the SEM imaging process, suggesting that the inherent electronic properties of the nanosheets are preserved as well. However, in order to support this, four-point probe measurements were made on transferred films. By measuring the sheet resistance for the nanosheet samples the resistivity (ρ) was obtained using the relationship (Eq. 5.1)

$$\rho = R_{square} \cdot d \quad (5.1)$$

where R_{square} and d are the sheet resistance and film thickness, respectively [20]. Based on SEM and profilometry measurements of other samples, a film thickness of 12nm was used for all calculations. The results are presented in Table 5.1 and support the retention of nanosheet properties through the transfer process. Due to the thin nature of the nanosheet films, the soft polymeric substrate and the nature of the four-point probe measurements, it is extremely difficult not to puncture the nanosheet films. This could explain the increase in the observed sheet resistance. The expansion of this transfer process to thermoplastic polymers and stiff substrates such as silicon wafers are also of interest and are being investigated. The four-point probe measurements were carried out using a Jandel Multi-height Probe, linear probe instrument from Luna and a comparable instrument at NRL.

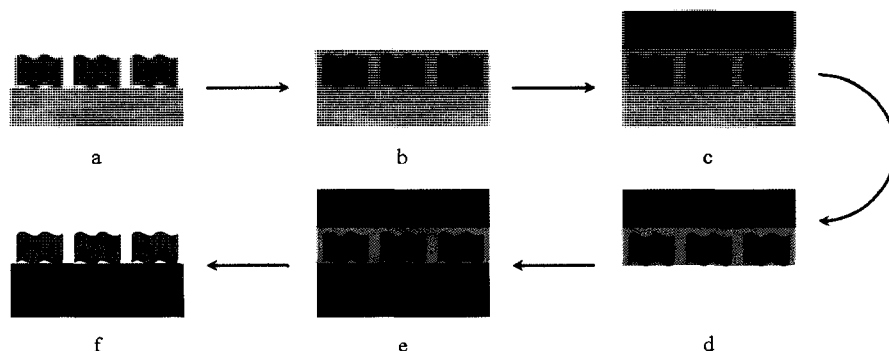


Figure 5.7: Schematic of transfer process using a supporting substrate (c) and a polymeric adhesive layer (e). The nanosheets are grown on a silicon wafer (a) and then cast with polystyrene (b). The support substrate is applied while the polystyrene film is drying (c) and afterwards the growth substrate is removed (d). The stiff substrate of interest is cast with a polymeric adhesive layer and then placed in contact with the exposed basal layers of the nanosheet film (e). The support substrate is removed, aided by heating, and the polystyrene washed away leaving a nanosheet film on a zero thermal-budget substrate (f).

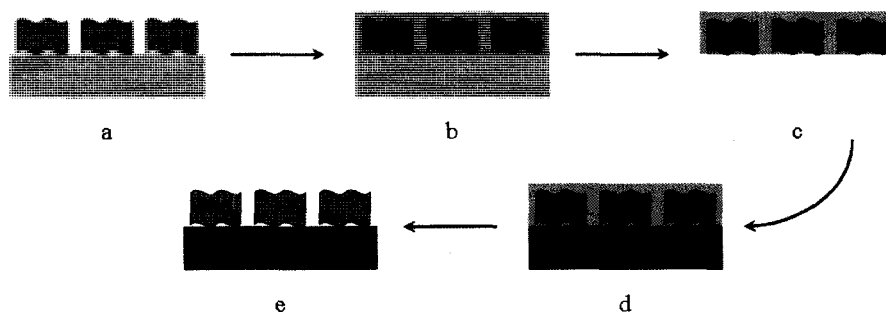


Figure 5.8: Schematic representation of the transfer of nanosheet films without the aid of supporting substrates to a flexible polymeric substrate. The nanosheets are grown of a silicon substrate (a) and then spin cast with polystyrene (b). The polystyrene/nanosheet film is then removed (c) and a silicone substrate is put in place (d). The polystyrene is then washed away (e) without damaging the silicone substrate.

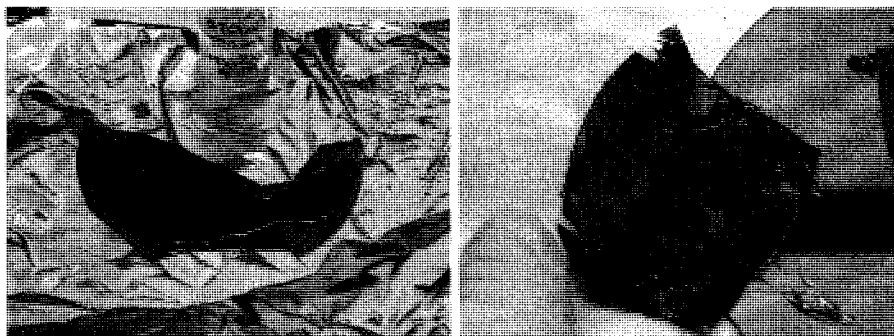


Figure 5.9: Photographs of the creation of silicone substrates. The flexible, solvent resistance substrates were manufactured without the aid of supporting substrates by applying the silicone solution (left) or by doctor blading the silicone (right) directly to the exposed basal layers of the nanosheet film.

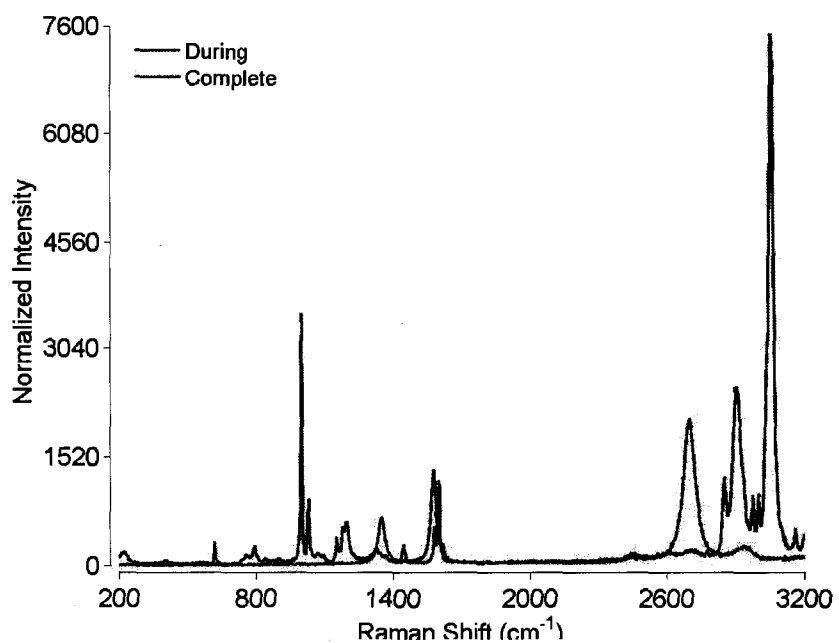


Figure 5.10: Raman of post-transfer carbon nanosheets. As is illustrated via the D and G peaks, the graphitic nature of the nanosheet structure is maintained. Also shown is that Raman can be used to determine how clean the sample is. The blue line represents a transferred nanosheet sample inspected with only a slight rinsing and the red line represents a sample after immersion and rinsing, showing the clean, transferred nanosheet film.

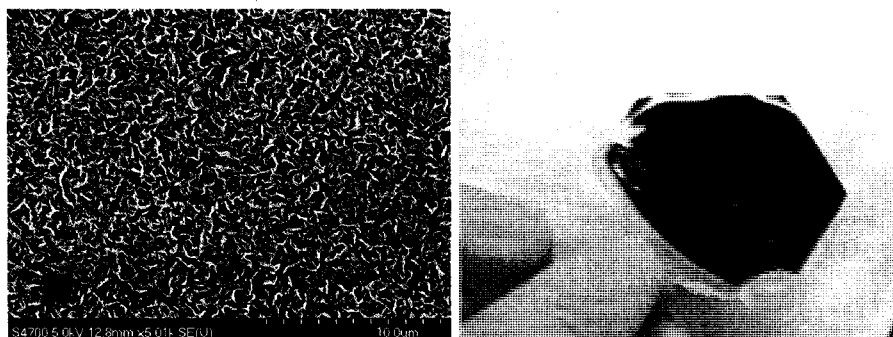


Figure 5.11: SEM images of transferred nanosheets. As can be seen, the vertical morphology of the nanosheets is retained throughout the process. The lack of charging suggests that the nanosheets have retained their electronic properties as well. The image on the right reveals that the transfer of large areas is possible.

Table 5.1: As-deposited sheets and transferred sheets have a resistivity close to that of graphite. Values reported are best values based on experiments with varying force of probes. Average is based on varying the outer probe current from 0.1mA to 1.5mA.

Sample	Sheet Resistance (Ω / \square)	Resistivity ($10^{-5} \Omega \text{ cm}$)
Graphite	41.7	5 [20]
As-deposited nanosheets	67.53	81.0
Transferred nanosheets	108.77 - 272.5	130 - 327

5.5 Photoluminescence measurements as a proof of concept for carbon nanosheet as high surface area electrodes

For organic photovoltaics (OPVs), conjugate polymers are used in the active layer. During the absorption of a photon, an electron is excited from a lower energy level to a higher energy level, creating an electron-hole pair, termed an exciton. This exciton typically has a lifetime of hundreds of picoseconds before the electron and hole radiatively recombine releasing another photon. This process is called photoluminescence (depicted schematically in Fig. 5.12) and is quenched when the excitons are dissociated. Therefore the photoluminescence intensity of an organic photovoltaic device can be used to determine the effectiveness of charge separation in the device. This efficiency is representative of the quality of the donor-acceptor interface.

To show the feasibility of an organic photovoltaic (OPV) device using nanosheets as an ultra-high surface area electrode, nanosheets were incorporated into poly[2-methoxy-5-(2'-ethyl-hexyloxy)-1,4-phenylene vinylene] (MEH-PPV) films (Fig. 5.13). MEH-PPV is a common polymer used in OPV bulk heterojunction devices. The unique structure of the nanosheets offers the possibility of their use as a nanostructured electrode in a bulk-heterojunction device setup (demonstrated schematically in Fig. 5.14). The full incorporation of their dense canopy into a photoactive polymer would allow for increased charge collection and the conductive properties of both the vertical sheets and horizontal basal planes suggest more efficient charge transport to the electrodes. The use of nanosheets in an OPV device could offer several advantages, such as ease of processing, multi-layer device fabrication and photon trapping. Previous work has shown the interface between other carbon nanostructures, such as fullerenes [81,82] or carbon nanotubes [83], and the polymer to be an effective dissociation interface for the photoexcited excitons (Fig. 5.14), with transfer of electrons from the π -conjugated polymer to the carbon structures. Carbon nanosheets are composed

of a sp^2 -conjugated carbon lattice like fullerenes that would allow the nanosheets to act as electron acceptors. Also, since nanosheets are composed of graphene layers and graphene is a zero bandgap semiconductor [18], they may be more efficient. Finally, nanosheets have been shown to possess a work function ≈ 4.8 eV therefore enabling the maintenance of the built-in electric field between the electron and hole-collecting electrodes.

Photoluminescence measurements were performed on a Perkin Elmer LS-55 Luminescence spectrometer equipped with a solid sample holder and the results are shown below in Figure 5.15. As illustrated, the photoluminescence of the MEH-PPV system is quenched by three orders of magnitude, suggesting that nanosheets can be effectively used for exciton separation.

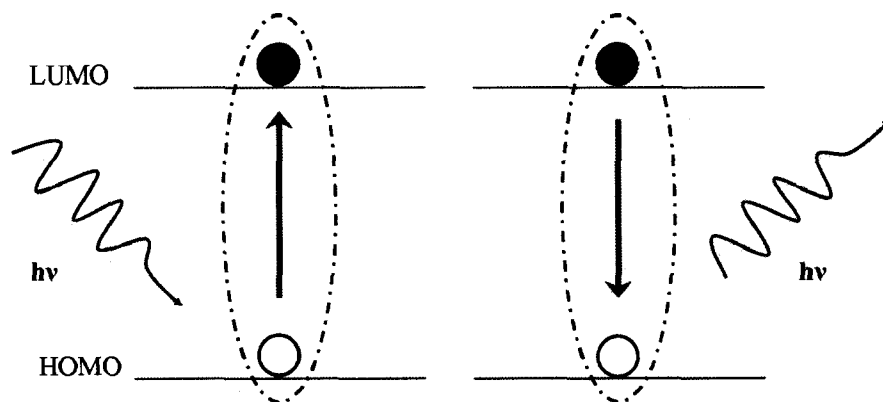


Figure 5.12: representation of the photoluminescence process for illustration.

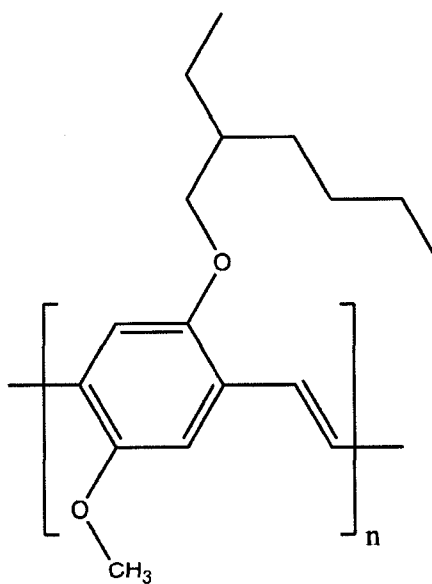


Figure 5.13: The structure of MEH-PPV, a common conjugated polymer used in organic photovoltaics, showing one repeat unit ($n = 1$) of the polymer.

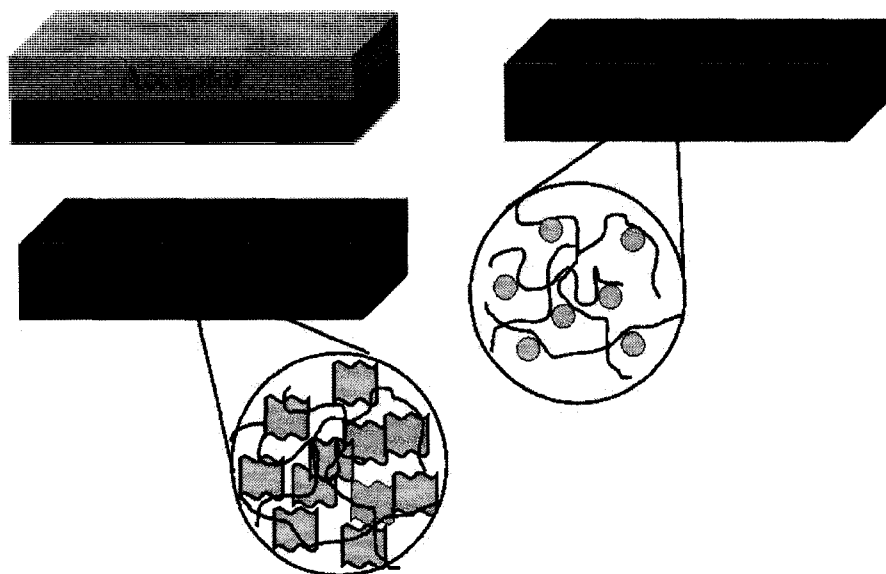


Figure 5.14: Typical photovoltaic device setup with the electron donor represented in light blue and the acceptor represented in red. The device depicted in the upper left is a planar heterojunction where the interface of the materials represents the junction. The upper right is bulk heterojunction, with the acceptor material (e.g., fullerenes) blended into the donor (polymer) material. The bottom device represents the nanosheet device, illustrating the decreased distance excitons would need to travel before encountering an interface for separation.

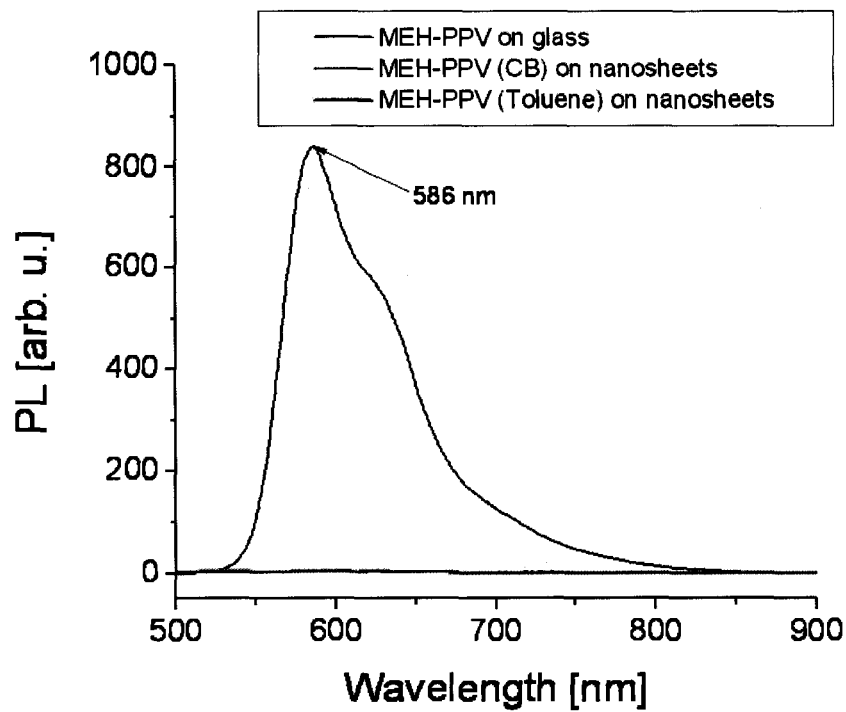


Figure 5.15: Photoluminescence results of nanosheets incorporated into MEH-PPV, a common polymer used in organic photovoltaic devices. The spectrum for the polymer alone is represented by the black line while the nanosheet composites are in blue and green with the only difference being the solvent.

5.6 Summary

We have shown the ability to conformally coat individual carbon nanosheets with a variety of polymers and then incorporate the sheets into films, creating unique composites. As a specific example we demonstrated the proof-of-concept for nanosheets as a high surface area electrode for OPV applications through the quenching of photoluminescence of MEH-PPV in a polymer/nanosheet composite thin film. We have also shown the ability to retain the original morphological and electrical properties of the nanosheets during a transfer from growth substrates to polymer substrates which have seen no thermal budget. These achievements demonstrate the versatility of carbon nanosheets as an ultra-high surface area electrode material.

Chapter 6

Summary and future work

6.1 Summary

The work described in this dissertation focused on the development of carbon nanosheets as high surface area electrodes via three main approaches—the chemical modification of the carbon nanosheet material, the complete incorporation of the nanosheets into a polymeric film and a proof-of-concept measurement. The chemical modification of the nanosheets represents a large portion of this work and can be divided into four main areas, i.e., the functionalization treatment (section 2.3), inspection via x-ray absorption near-edge spectroscopy (XANES) (section 3.2), investigation of the defects with thermal desorption spectroscopy (TDS) (section 3.3) and finally the examination of the functional groups through high resolution x-ray photoelectron spectroscopy (XPS) (section 3.4). The wetting and conformal coating of nanosheets with different polymers and finally building to composite films is discussed in section 5.4. It was also shown that the nanosheets can be transferred to a non-growth substrate with zero thermal budget. Finally, as proof-of-concept, nanosheets were used as nanostructured templates (section 4.4) for the growth of TiO_2 thin films and as a means of exciton separation (section 5.5) for organic photovoltaics.

The functionalization of the nanosheets via acid-treatment (section 2.3) was the first step in developing carbon nanosheets as a viable option for advanced graphene electronics. Because graphene is effectively chemically inert, the edge states offer the

most serviceable areas and produce interesting electronic properties. By introducing defects into the graphene lattice of the carbon nanosheets we were able to effectively introduce other avenues of interest. However, in order to pursue these interests, more information pertaining to the chemical nature of the defects was needed, which brings us to the characterization of the defects, the largest contributor to this research.

Through XANES (section 3.2) we were able to identify the defects as oxygen decorated defect sites that created available unoccupied states just above the Fermi-level in the nanosheet system. These defects observed in the spectra were assigned to C=O π^* (B1 peak) and C-O σ^* (B2 peak) transitions. These features were observed in the acid-treated as well as the water-treated samples though with varying intensities. This suggests that the acid treatment creates a different type of defect, or a higher density of one of two defects, than does the water treatment. Density functional theory was able to reproduce in simplified form the spectral features observed in the XANES experiments, lending credence to our primary assumptions. This work also suggested that the conductivity of the nanosheets—and also graphene—could be increased by the controlled introduction of defects into the lattice. We were able to confirm this via a measurement made for the first time by a modified AFM tip in a focused ion beam - scanning electron microscope setup (section 3.2.1). Also during the XANES study, we were able to identify that the defects—or functional groups present as a result of the treatments—could be removed via thermal annealing. These observations lend us to state that we have developed a novel way to controllably introduce defects and functionality into the nanosheet system.

TDS (section 3.3) was employed for the determination of the chemical nature of the functional groups that were introduced into the nanosheet lattice via the acid treatment. Through TDS it was determined that the functional groups created are carboxylic acid and hydroxyl groups. It was also shown that we were able to introduce functionality through the water-treatment of the nanosheet material. Both of these

treatments resulted in the decrease of hydrophobic behavior of the carbon nanosheet material. During the course of the TDS experiments, we were able to identify the presence of surface reactions taking place when the nanosheets are heated. These reactions themselves are a step towards the further functionalization of the carbon nanosheet material because they produce other functionalities, i.e., carboxylic anhydrides and lactones, in the nanosheet lattice. Deconvolution of the TDS spectra utilizing the Polanyi-Wigner equation produced interesting results. The 1st order equations that were expected to depict the thermal decomposition of anhydride structures did not produce a satisfactory fit. However, use of 2nd order equations did produce a quality fit and resulted in the calculation of values for the number of molecules desorbing from the surface and for energy values of the desorption process. This study was complicated due to 1st and 2nd order processes being represented in the same spectra and by the contribution of the substrate which was not expected has produced an avenue of research of its own. This process has outlined a procedure that could be used for the qualitative and quantitative calculation of the functional groups.

In support of the identification of carboxylic acid and hydroxyl functional groups high resolution x-ray photoelectron spectroscopy was utilized. Survey scans of the as-deposited, acid-treated and water-treated samples demonstrated the presence of carbon and oxygen only. The sub-peak identification of the C(1s) and O(1s) spectra however proved to be difficult. Calibration of the XPS system for only the nanosheet system would need to be undertaken for a more accurate assignment. However, with calibration, it would be possible to correlate the atomic percentages of oxygen and carbon sub-peaks and their relative changes with heating to the molecules seen desorbing from the samples during the TDS experiments. Despite the lack of stand-alone assignment via XPS, the trends observed in the data support the assignments made through the XANES and TDS work.

In Chapter 4, the functionality of the treated nanosheets was demonstrated by

depositing TiO_2 onto as-deposited and functionalized nanosheets via atomic layer deposition (ALD). This process not only illustrated the ability of carbon nanosheets to be used as nanostructured templates, but also effects of the acid treatment. It was shown that the as-deposited sheets were successful in supporting the creation of nanostructured TiO_2 films, though pinholes and defects were observed in the film. However, the acid-treated nanosheets, when used as a substrate, produced an amorphous layer of TiO_2 about 5nm in width before giving way to crystalline growth. This resulted in a continuous nanostructure TiO_2 film. TiO_2 films are of interest in applications ranging from gas sensors to photovoltaics and the ability to grow nanostructured films greatly increases the chance of success of this material.

Finally, Chapter 5 illustrated the complete incorporation of the nanosheets into polymeric material to form polymer/nanosheet composite films. This was accomplished via the conformal coating of the nanosheets with varying polymeric materials, e.g., silicone and poly[2-methoxy-5-(2'-ethyl-hexyloxy)-1,4-phenylene vinylene] (MEH-PPV). By controlling the spin-casting process and the viscosity of the casting material, wetting of the nanosheets was obtained and utilized. The success of this process also resulted in the transfer—for the first time—of carbon nanosheets films to a non-growth substrate, including a polymeric substrate. As a proof-of-concept, the MEH-PPV/nanosheet films were inspected via photoluminescence (PL) measurements and the nanosheet composites showed a PL quenching of three orders of magnitude greater than the MEH-PPV films alone. These results suggest that carbon nanosheets can be used as an effective interface for the separation of electron-hole pairs in organic photovoltaic devices.

Overall, this work has produced several advances in the understanding of carbon nanosheets science and their implementation as high surface area electrodes. The introduction of carboxylic acid and hydroxyl groups into the graphene lattice of the carbon nanosheets was shown. The ability of these groups to increase the conductiv-

ity of the nanosheets was also demonstrated. A process for the calculation of defect type and quantity was outlined and the presence of complicated surface reactions was identified using TDS and high resolution XPS. We have shown the ability to successfully transfer the nanosheet film to a non-growth, zero thermal-budget substrate in addition to conformally coating the nanosheets with polymeric material. Finally, we were able to establish nanosheets as a nanostructured template for the growth of TiO_2 films and as an interface for the separation of excitons in organic photovoltaics. This work is not only applicable for carbon nanosheets, but should also advance the knowledge of other fullerene type structures such as graphene and graphene oxide.

6.2 Avenues for future work

As a result of this work, there are several areas of follow on research that are suggested. In this section, five directions will be identified and discussed. The first has already been identified in previous sections and is the quantification of defect density and quality through TDS, MATLABTM and high resolution XPS. The second is the further functionalization of carbon nanosheets. Third, continued development of carbon nanosheets as high surface area electrodes in organic photovoltaics. The fourth area is the epitaxial growth of graphene via RF PECVD and finally, the fifth is the development of carbon nanosheets as chemical sensors.

6.3 Defect concentration and quality in carbon nanosheets

As mentioned in section 3.3.2, 3.4.2 and 3.5, we were able to successfully outline a procedure for defect control and quantization. The first step for this procedure is eliminating the substrate's contribution to the spectra. Using a substrate with no

native oxide would be ideal. This would also involve extensive characterization to ensure that the acid treatment does not damage or react with the substrate as well. Gold may be one substrate of interest as it has no native oxide and should not react with just HCl acid (though HCl is one of the components in aqua regia, one of the few reagents that can dissolve gold).

The next step involves deconvoluting the TDS spectra. By utilizing a straight line fitted to a $\ln(r/\theta^n)$ vs. $1/T$ plot, we would be able to determine if the process is 1st or 2nd order per desorption energy. This identification would then allow us to accurately apply the Polanyi-Wigner equation via our MATLABTM routine.

Finally, by using a calibrated and dedicated instrument, the sub-peak analysis of the high resolution XPS C(1s) and O(1s) peaks could in fact result in exact functional group identification as illustrated in the work of Zhang *et al.* [84]. In reference [84], they outline a mechanism for the oxidative process that occurs when using a sulfuric/nitric acid combination with sonication and are they are able to identify transition states that evolve over time. With peak fitting, there is a trade off of a better fit through more peaks and computational time consumed. However, it is possible that we simplified our analysis too much with too few sub-peaks. An inspection of fit parameters including number of sub-peaks would have to be involved in this work.

This analysis should also include water-treated samples. Yang *et al.* report [56] the functionalization of multi-walled carbon nanotubes through sonication in deionized water. This treatment does not result in the cleavage of a sp^2 -hybridized C-C bond, but the oxidation of sp^3 -hybridized CH₂ and CH₃ groups already present. As reported by Zhao *et al.* [37, 38] these groups are also present in carbon nanosheets and offer sites for functionalization. During our treatment of nanosheets (section 2.3.1), the nanosheets do not undergo extreme heating and the functionalization via the water-treatment was unexpected. However, it may be possible that the inherent

defects present in the carbon nanosheets experience localized heating and therefore offer more reactive sites for functionalization. It is more likely however, that the functionalization of water-treated carbon nanosheets occurs due to the heating of the samples during analysis. This is supported by the work reported in [84]. The outlined procedure above would allow for defect control and quantization as well as lay the ground work for the true mechanism of nanosheet functionalization.

6.4 Further functionalization of carbon nanosheets

The functionalization of carbon nanosheets was an important step in the development of nanosheet technology. As is illustrated by the reviews of references [51] and [52], a vast array of possible functionalization experiments of single-walled nanotubes exist. These chemical modifications offer a controllable pathway for the tailoring of the desirable properties of nanotubes. Through these experiments, scientists are capable of making nanotubes components in applications ranging from molecular sensing to catalyst supports. Until now, the same could not be said for carbon nanosheets.

The identification of the functional groups introduced during our acid-treatment will allow organic chemists to tailor properties of the nanosheets for their desired application. We have already shown that the carboxylic acid and hydroxyl groups introduced during our acid and water treatments have the ability to decrease the hydrophobic behavior of the nanosheets. We have also shown that the defects introduced during the acid treatment are capable of improving the conductivity of the nanosheets. These are just two properties that already show significant potential for aiding the advancement of nanosheet technology.

6.5 Carbon nanosheets as high surface area electrodes

As was illustrated in section 5.5, carbon nanosheets offer the ability to successfully separate electron-hole pairs for use in photovoltaic devices. However, much is left to be explored. One advantage of using organics in photovoltaics is the ability to tailor the bandgaps of the material for the desired match. We were able to demonstrate that the introduction of defects can change these properties of the nanosheets [14], offering yet another tool for tuning the adsorption capabilities of the material.

Delivery of a working device remains extremely difficult however. Complications include drying of the polymeric material without delamination occurring, contacting the external circuit without creating shorts via pinholes in the polymeric material and encapsulation of the material for device characterization. These concerns are mostly engineering concerns, but must be addressed for the advancement of nanosheet technology. There are other polymeric materials that need to be investigated and the effects of functionalized nanosheets needs to be systematically studied in combination with extended functionalization of the carbon nanosheets (section 6.4).

Carbon nanosheets also hold the potential to be used in dye-sensitized solar cells as well. Wang *et al.* [85] successfully demonstrated the use of graphene films as transparent electrodes in these devices. Combining these observations with the results that we have presented in Chapter 4 suggest that nanosheets could be used as well.

Photovoltaics are not the only opportunity for the use of carbon nanosheets as an electrode material. As demonstrated in references [86–88] and as was illustrated in Figure 2.4, carbon nanostructures can be grown on carbon paper for use in fuel cell applications. However, due to the extreme hydrophobic behavior of the nanosheets, the Pt catalysts that were dispersed in a water solution were not deposited on the nanosheet surface (Figure 2.4 (right)).

Post-treatment nanosheets do not display the same hydrophobic behavior however.

Therefore, the chemically active sites that have been introduced into the graphene lattice of the sheets not only offer reduced hydrophobic behavior for the casting of the Pt catalyst, they also offer potential high energy binding sites for the catalyst as well. Though the amount of Pt loading should depend on the length of the functionalization treatment and the stability of these structures would then need to be investigated via a systematic approach, the need for alternative fuel sources at this time and the potential for carbon nanosheets to be high surface area catalyst support warrant investigation.

6.6 Epitaxial growth of graphene

As mentioned in the introduction (section 1.1), the isolation of single-layer graphene was not seen experimentally until quite recently when Novoselov *et al.* were able to do it [10, 18] by mechanical exfoliation. However, this process is tedious and the production and manipulation of large area films is difficult [89]. Since that time, others have also been able to fabricate graphene via the sublimation of silicon from single crystal silicon carbide [9, 90–92] though the size domains and uniformity of these films remain an issue, not to mention the cost and the temperatures required (1100°C). Because of these limitations it would be unlikely for these processes to be scaled up for industrial use. Another approach is the use of chemically modified graphene material, such as graphene oxide (GO) to produce large area films [85, 93–97]. However, in order to produce these films, the films must undergo long chemical reductions via exposure to hydrazine hydrate vapor to recover C-C and C=C bonds, after which the conductance is still not that of graphene [94].

Initial results of the transfer process described in section 5.4 suggest that large graphene grains are present in the basal layers of the carbon nanosheets. By undertaking a systematic study that includes matching the lattice parameter of graphene

(0.246nm) to various substrates—such as SiO₂ (0.49nm) and MnS (0.5011nm)—and growth parameters, such as temperature and time, it is possible that a cheap, large-area process for the synthesis of graphene could be developed. This process would greatly increase the opportunity for the industrial scale up of graphene production for advanced electronic applications.

6.7 Carbon nanosheets as chemical sensors

Single-walled carbon nanotubes (SWNTs) are cylinders of carbon, \approx 1nm in diameter, microns long and with a wall thickness of one atom. These structures have shown remarkable electrical and mechanical properties as well as the ability to detect trace levels of molecules through both conductance [24,25] and capacitance [26] based methods when a molecule interacts with the tube sidewalls. Continued inspection of chemical sensing utilizing SWNTs revealed that random networks of nanotubes are capable of sensitivity for a wide range of analyte materials at extremely low detection limits [26]. It has also been shown that molecular interactions with defect sites dominate the SWNTs' sensitivity in both detection schemes, that the interaction varies based on the site and that by controlling the defect density, the sensor sensitivity and selectivity can be modified [98]. However, with SWNTs, as the sensitivity is increased with defect density, the cost is the loss of conductance.

Chemically modified graphene (CMG)—a sp^2 -bonded graphene sheet with attached functional groups—allows for another approach to the problem. Two dimensional graphene can be chemically modified with any number of molecules ranging from atomic hydrogen, to carboxylic acids, to DNA. In particular, graphene oxide (GO)—a CMG with many epoxides, alcohols and carboxylic acids groups [28]—is attractive since these functional groups are particularly favorable as chemically active defect sites. However, even though the ability to produce continuous thin films has

been shown [85, 93–97], GO offers its own disadvantages. Even after chemically reducing the films to recover the C-C and C=C bonds for increased conductivity, the conductance is still not as high as graphene [94] and the total area available for molecular interactions is limited to a single flat surface.

Carbon nanosheets present another promising opportunity for graphene-based chemical sensing. Nanosheets are composed of *vertical* free-standing graphene layers and horizontal basal layers with an extremely high surface area [22] that can be patterned using standard photolithographic techniques [69, 70]. Our recent work, as discussed earlier, has demonstrated that chemically active defect sites useful for molecular detection can be controllably introduced into the graphene lattice of the nanosheets [14] and enhance the conductivity of the nanosheets. The characterization work of XANES, TDS and XPS discussed previously in this dissertation has identified these defects as carboxylic acid and hydroxyl type functional groups.

The use of nanosheets for sensing applications offers advantages over both SWNTs and GO in conductance based systems. The morphology of the nanosheets allows for the creation of a multitude of chemically active sites like the SWNT networks, but without the degradation in conductance. Nanosheets are a pure carbon sp^2 -system with defects being added, unlike the GO systems that require long reductions to recover a mixture of C-C single and double bonds. It may be possible to take advantage of these defects and the inherent nanosheet properties in the creation of novel, nanosheet-based chemical sensors.

Graphene planes, in graphene [99, 100] and SWNTs [24, 26], have shown significant responses to molecular adsorbates and though there is no prior sensing technology available for nanosheets, their field emission properties have shown dependence on adsorbates as well [37, 38]. These observations support the use of nanosheets as chemical sensors since molecular adsorbates will affect their conductance, as well as their capacitance to produce a sensitive detection scheme.

Despite the availability of literature on SWNT sensing technology, questions and difficulties remain, such as the ability to tailor chemical specificity and reducing $1/f$ noise. Because all the atoms in a SWNT are surface atoms their sensitivity to molecular adsorbates is exceptional, but it is also a source of large $1/f$ noise [101]. Graphene oxide is still yet unproven in the chemical sensing realm and offers its own concerns about being able to reproduce reliable devices. Because nanosheets are a graphene-based carbon nanostructure, capabilities similar to SWNTs and GO should be expected. However, nanotube networks involve inter-nanotube contacts that produce excess low-frequency noise, known as $1/f$ noise, and reduce signal strength by introducing series resistance [101]. On the other hand, the nanosheet systems are a continuous network and it is expected that $1/f$ noise will be significantly reduced over SWNT devices. Secondly, improved sensitivity is expected for functionalized nanosheets as their defect density is readily controlled, which provides an advantage of GO-based systems. Nanosheets also offer a higher surface area for detection than do GO-based systems. The further functionalization of nanosheets (section 6.4) makes the molecular sensitivity of the nanosheet system an asset as well. Finally, because nanosheets can be transferred to polymeric substrates, they offer unique opportunities for large scale device production.

Afterword

Much of the material presented in this dissertation has been, or is currently in the process of being, submitted for peer review. Part of the contents of Chapter 3 have been published in the Journal of Physics D: Applied Physics. The remaining data is currently being prepared for publication. The results of Chapter 4 have been submitted to Advanced Materials. The study presented in Chapter 4 was supported by the Swedish Research Council (VR), in part by the U.S. Department of Energy (Grant#: DE-FG02-07ER84806) and the U.S. AFOSR (Grant#: FA9550-06-C-0010). Chapter 5 is currently being prepared for publication. The research presented in this thesis was supported by the U.S. AFOSR under contract FA9550-07-C-0050. Any opinions, findings, and conclusions or recommendations expressed in this material are those of the authors and do not necessarily reflect the views of the United States Air Force.

Bibliography

- [1] H. W. Kroto, J. R. Heath, S. C. O'Brien, R. F. Curl, and R. E. Smalley, *Nature* **318**, 162 (1985).
- [2] M. Reibold *et al.*, *Nature* **444**, 286 (2006).
- [3] S. Iijima, *Nature* **354**, 56 (1991).
- [4] M. Dresselhaus, G. Dresselhaus, and P. Avouris, *Carbon Nanotubes: Synthesis, Structure, Properties, and Applications*, Topics in Applied Physics Vol. 80, 1st ed. (Springer, New York, 2001).
- [5] Y. Ando, X. Zhao, and M. Ohkohchi, *Carbon* **35**, 153 (1997).
- [6] J. Wang *et al.*, *Carbon* **42**, 2867 (2004).
- [7] J. J. Wang *et al.*, *Applied Physics Letters* **85**, 1265 (2004).
- [8] W. A. de Heer *et al.*, *Solid State Communications* **143**, 92 (2007).
- [9] J. Hass *et al.*, *Applied Physics Letters* **89**, 143106 (2006).
- [10] K. S. Novoselov *et al.*, *Proceedings of the National Academy of Sciences* **102**, 10451 (2005).
- [11] Y. Wu, P. Qiao, T. Chong, and Z. Shen, *Advanced Materials* **14**, 64 (2002).
- [12] A. T. H. Chuang, B. O. Boskovic, and J. Robertson, *Diamond and Related Materials* **15**, 1103 (2006).
- [13] N. G. Shang *et al.*, *Chemical Physics Letters* **358**, 187 (2002).
- [14] V. A. Coleman *et al.*, *Journal of Physics D: Applied Physics* , 062001 (2008).
- [15] T. W. Ebbesen and P. M. Ajayan, *Nature* **358**, 220 (1992).
- [16] S. Iijima, T. Wakabayashi, and Y. Achiba, *J. Phys. Chem.* **100**, 5839 (1996).
- [17] Y. Wu and B. Yang, *Nano Lett.* **2**, 355 (2002).
- [18] K. S. Novoselov *et al.*, *Science* **306**, 666 (2004).

- [19] J. Wang *et al.*, Journal of Vacuum Science & Technology B: Microelectronics and Nanometer Structures **22**, 1269 (2004).
- [20] M. Zhu, *Carbon nanosheets and carbon nanotubes by RF PECVD*, Ph.d., The College of William and Mary, 2006.
- [21] M. Zhu *et al.*, Diamond and Related Materials **16**, 196 (2007).
- [22] M. Zhu *et al.*, Carbon **45**, 2229 (2007).
- [23] S. Gunes, H. Neugebauer, and N. S. Sariciftci, Chem. Rev. **107**, 1324 (2007).
- [24] J. Kong *et al.*, Science **287**, 622 (2000).
- [25] P. G. Collins, K. Bradley, M. Ishigami, and A. Zettl, Science **287**, 1801 (2000).
- [26] E. S. Snow, F. K. Perkins, E. J. Houser, S. C. Badescu, and T. L. Reinecke, Science **307**, 1942 (2005).
- [27] K. Besteman, O. L. Jeong, F. G. M. Wiertz, H. A. Heering, and C. Dekker, Nano Letters **3**, 727 (2003).
- [28] A. Lerf, H. He, M. Forster, and J. Klinowski, J. Phys. Chem. B **102**, 4477 (1998).
- [29] J. Goldstein *et al.*, *Scanning Electron Microscopy and X-Ray Microanalysis*, Third ed. (Lluwer Academic/Plenum, New York, 2003).
- [30] W. Weber and R. Merlin, *Raman Scattering in Materials Science*, Materials Science Vol. 42 (Spring-Verlag, New York, 2000).
- [31] F. Tuinstra and J. L. Koenig, The Journal of Chemical Physics **53**, 1126 (1970).
- [32] J. R. Ferraro, K. Nakamoto, and C. W. Brown, *Introductory Raman Spectroscopy*, Second ed. (Academic Press, San Diego, 2003).
- [33] A. C. Ferrari and J. Robertson, Physical Review B **61**, 14095 (2000).
- [34] D. A. Skoog, F. J. Holler, and T. A. Neiman, *Principles of Instrumental Analysis*, Fifth edition ed. (Saunders College Publishing, 1998).
- [35] D. Koningsberger and R. Prins, *X-ray Absorption: Principles, Applications, techniques of EXAFS, SEXAFS and XANES*, Chemical Analysis Vol. 92, 1st ed. (John Wiley & Sons, Eindhoven, 1988).
- [36] R. Nyholm, S. Svensson, J. Nordgren, and A. Flodström, Nuclear Instruments and Methods in Physics Research Section A: Accelerators, Spectrometers, Detectors and Associated Equipment **246**, 267 (1986).
- [37] X. Zhao *et al.*, Journal of Chemical Physics **124**, 194704 (2006).

- [38] X. Zhao, DAI **68**, 214 (2006).
- [39] Y. Ferro, F. Marinelli, and A. Allouche, Chemical Physics Letters **368**, 609 (2003).
- [40] A. M. de Jong and J. W. Niemantsverdriet, Surface Science **233**, 355 (1990).
- [41] H. Bubert and H. Jenett, *Surface and Thin Film Analysis* (Wiley-VCH Verlag GmbH, 2002).
- [42] W. A. D. M. P. Seah, Surface and Interface Analysis **1**, 2 (1979).
- [43] C. R. Cole, *Electron stimulated desorption of hydronium ions from chromium oxide surfaces*, PhD thesis, The College of William and Mary, 2005.
- [44] W. Xia, Y. Wang, R. Bergsträßer, S. Kundu, and M. Muhler, Applied Surface Science **254**, 247 (2007).
- [45] E. Cappelli *et al.*, Diamond and Related Materials **14**, 959 (2005).
- [46] E. Cappelli *et al.*, Thin Solid Films **482**, 305 (2005).
- [47] M. Imamura *et al.*, Physica B: Condensed Matter **208-209**, 541 (1995).
- [48] S. Banerjee *et al.*, Chemical Communications , 772 (2004).
- [49] A. Kuznetsova *et al.*, J. Am. Chem. Soc. **123**, 10699 (2001).
- [50] J. Li, K. Chajara, J. Lindgren, and H. Grennberg, Journal of Nanoscience and Nanotechnology **7**, 1525 (2007).
- [51] S. Banerjee, T. Hemraj-Benny, and S. S. Wong, Advanced Materials **17**, 17 (2005).
- [52] S. Niyogi *et al.*, Acc. Chem. Res. **35**, 1105 (2002).
- [53] J.-H. Zhou *et al.*, Carbon **45**, 785 (2007).
- [54] A. Kuznetsova *et al.*, Chemical Physics Letters **321**, 292 (2000).
- [55] H. P. Boehm, Carbon **40**, 145 (2002).
- [56] D. Q. Yang, J. F. Rochette, and E. Sacher, J. Phys. Chem. B **109**, 7788 (2005).
- [57] S. M. George, A. W. Ott, and J. W. Klaus, J. Phys. Chem. **100**, 13121 (1996).
- [58] U. Diebold, Surface Science Reports **48**, 53 (2003).
- [59] B. O'Regan and M. Gratzel, Nature **353**, 737 (1991).
- [60] H. Tang, K. Prasad, R. Sanjinés, and F. Lévy, Sensors and Actuators B: Chemical **26**, 71 (1995).

- [61] K. N. L. N. M. Knez, *Advanced Materials* **19**, 3425 (2007).
- [62] G. Zhang, H. Huang, Y. Zhang, H. L. W. Chan, and L. Zhou, *Electrochemistry Communications* **9**, 2854 (2007).
- [63] A. T. A. R. A. H. J. Sundqvist, *Chemical Vapor Deposition* **9**, 21 (2003).
- [64] J. Aarik *et al.*, *Applied Surface Science* **193**, 277 (2002).
- [65] D. B. Farmer and R. G. Gordon, *Electrochemical and Solid-State Letters* **8**, G89 (2005).
- [66] M. Schuisky *et al.*, *Journal of The Electrochemical Society* **147**, 3319 (2000).
- [67] H. Najafov, S. Tokita, S. Ohshio, A. Kato, and H. Saithoh, *Japanese Journal of Applied Physics* **44**, 245 (2005).
- [68] S. Wang *et al.*, *Applied Physics Letters* **89**, 183103 (2006).
- [69] T. Tyler *et al.*, *Journal of Vacuum Science & Technology B (Microelectronics and Nanometer Structures)* **24**, 2295 (2006).
- [70] T. Tyler *et al.*, High current field emission from graphitic carbon nanosheets, *Technical Digest of the 18th International Vacuum Nanoelectronics Conference (IEEE Cat. No. 05TH8837)*, pp. 320–1, Oxford, UK, 2005, IEEE.
- [71] Y.-R. Cho *et al.*, *Materials Science and Engineering B* **79**, 128 (2001).
- [72] D. Whang, S. Jin, Y. Wu, and C. M. Lieber, *Nano Lett.* **3**, 1255 (2003).
- [73] Y. Huang, X. Duan, Q. Wei, and C. M. Lieber, *Science* **291**, 630 (2001).
- [74] J. Zhu, M. Yudasaka, M. Zhang, D. Kasuya, and S. Iijima, *Nano Lett.* **3**, 1239 (2003).
- [75] A. C. Allen, E. Sunden, A. Cannon, S. Graham, and W. King, *Applied Physics Letters* **88**, 083112 (2006).
- [76] E. Sunden, J. K. Moon, C. P. Wong, W. P. King, and S. Graham, *Journal of Vacuum Science & Technology B: Microelectronics and Nanometer Structures* **24**, 1947 (2006).
- [77] C. K. M. Fung, C. K. M. Fung, V. T. S. Wong, R. H. M. Chan, and W. J. A. L. W. J. Li, *Nanotechnology, IEEE Transactions on* **3**, 395 (2004).
- [78] Y. J. Jung *et al.*, *Nano Lett.* **6**, 413 (2006).
- [79] N. R. Raravikar *et al.*, *Chem. Mater.* **17**, 974 (2005).
- [80] S. Huang, L. Dai, and A. W. H. Mau, *J. Phys. Chem. B* **103**, 4223 (1999).

- [81] N. S. Sariciftci, L. Smilowitz, A. J. Heeger, and F. Wudl, *Science* **258**, 1474 (1992).
- [82] C. J. Brabec *et al.*, *Chemical Physics Letters* **340**, 232 (2001).
- [83] E. Kymakis, I. Alexandrou, and G. A. J. Amaratunga, *Journal of Applied Physics* **93**, 1764 (2003).
- [84] G. Zhang, S. Sun, D. Yang, J.-P. Dodelet, and E. Sacher, *Carbon* **46**, 196 (2008).
- [85] X. Wang, L. Zhi, and K. Mullen, *Nano Lett.* **8**, 323 (2008).
- [86] C. Wang *et al.*, *Nano Lett.* **4**, 345 (2004).
- [87] X. Sun, R. Li, D. Villers, J. P. Dodelet, and S. Désilets, *Chemical Physics Letters* **379**, 99 (2003).
- [88] S.-S. Tzeng, K.-H. Hung, and T.-H. Ko, *Carbon* **44**, 859 (2006).
- [89] A. K. Geim and K. S. Novoselov, *Nature Materials* **6**, 183 (2007).
- [90] C. Berger *et al.*, *J. Phys. Chem. B* **108**, 19912 (2004).
- [91] C. Berger *et al.*, *Science* **312**, 1191 (2006).
- [92] T. Ohta, A. Bostwick, T. Seyller, K. Horn, and E. Rotenberg, *Science* **313**, 951 (2006).
- [93] H. Becerril *et al.*, *ACS Nano* **2**, 463 (2008).
- [94] S. Gilje, S. Han, M. Wang, K. L. Wang, and R. B. Kaner, *Nano Lett.* **7**, 3394 (2007).
- [95] S. Stankovich *et al.*, *Nature* **442**, 282 (2006).
- [96] S. Stankovich *et al.*, *Carbon* **45**, 1558 (2007).
- [97] H. Schniepp *et al.*, *Journal of Physical Chemistry B* **110**, 8535 (2006).
- [98] J. A. Robinson, E. S. Snow, S. C. Badescu, T. L. Reinecke, and F. K. Perkins, *Nano Lett.* **6**, 1747 (2006).
- [99] T. O. Wehling *et al.*, *Nano Lett.* **8**, 173 (2008).
- [100] F. Schedin *et al.*, *Nat Mater* **6**, 652 (2007).
- [101] E. S. Snow, J. P. Novak, M. D. Lay, and F. K. Perkins, *Applied Physics Letters* **85**, 4172 (2004).

Vita

Ronald A. Quinlan was born in Louisville, Kentucky on July 31, 1980 and grew up in Figsboro, VA. In June of 1998, he graduated from Fieldale-Collinsville High School as valedictorian. In August of 1998, Ron joined the United States Marine Corps, where he served 8 years in the reserves before being honorably discharged in 2006. In August of 1999, he began his tenure at the College of William and Mary and graduated with a Bachelor of Science degree in Chemistry in May of 2003. After a year of graduate study and teaching in the University of Tennessee's Chemistry Department, Ron returned to William and Mary as a graduate student for Dr. Brian Holloway to pursue a more applied field of study. In 2006 he received his Master of Science in Applied Science from the College of William and Mary.